THE UNIVERSITY OF QUEENSLAND

AUSTRALIA

Bioelectronic Materials and Devices:

An All-solid-state Eumelanin Based Organic Electrochemical Transistor

Margaryta Sheliakina

Bachelor of Biotechnology

Master of High Technologies

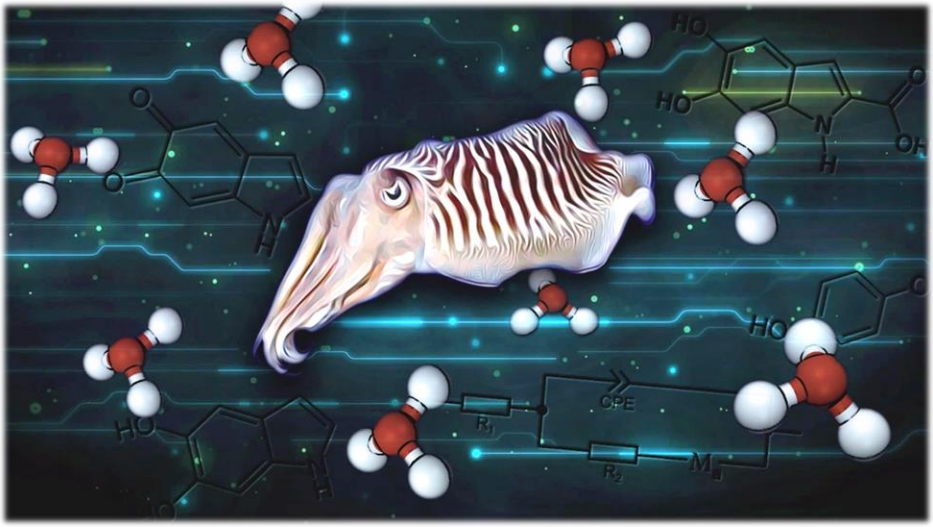

A thesis submitted for the degree of Doctor of Philosophy at

The University of Queensland in 2018

School of Mathematics and Physics

Abstract

Bioelectronics is an emerging field at the intersection of biology and electronics, which aims to create new ways to interface traditional semiconductor control circuitry with biological entities. Thus, a key goal in the field is to achieve ionic-to-electronic transduction, i.e. to create devices that translate biological signals (often ionic in nature) to high fidelity electronic signals (carried by electrons and holes) and *vice versa*. The motivation for the work presented in this thesis is the creation of biocompatible, all-solid-state transducing elements which could form the basis of so-called bioelectronic logic. To this end, the functional biomaterial eumelanin was investigated as the primary transducing element in an Organic Electrochemical Transistor (OECT) architecture.

Eumelanin is the human skin pigment and possesses a diverse collection of physico-chemical properties including electrical and photoconductivity, featureless broadband optical absorption, persistent free radical behaviour, and almost unity non-radiative conversion of absorbed photon energy. In addition it can be cast into device quality thin films. As a biomaterial eumelanin is inherently biocompatible, which is a key property for any viable bioelectronic material. However, it is eumelanin's hydration dependent conductivity that is important for creating functional OECT devices, since with changing its water content ionic (proton) concentrations can be varied to control and optimise transistor performance.

In the work presented in this thesis, the first all-solid-state biocompatible OECT bioelectronic transducer is demonstrated. The underlying operational mechanism is conclusively elucidated and found to be volumetric gating *via* the injection of protons from the eumelanin gate into the semiconductor transistor channel. Furthermore, device performance is correlated with eumelanin charge transport behaviour utilising impedance spectroscopy where it is shown that the hydration dependent charge transport is dominated by proton currents. Moreover, it is shown that the solid state OECT performance can be enhanced by chemically engineering the eumelanin thin films *via* copper ion chelation in a mechanism akin to traditional “doping”. The work contained within this thesis establishes structure-property relationships and basic operational principles for transducing elements, and is a step towards bioelectronic logic.

Declaration by author

This thesis is composed of my original work, and contains no material previously published or written by another person except where due reference has been made in the text. I have clearly stated the contribution by others to jointly-authored works that I have included in my thesis.

I have clearly stated the contribution of others to my thesis as a whole, including statistical assistance, survey design, data analysis, significant technical procedures, professional editorial advice, financial support and any other original research work used or reported in my thesis. The content of my thesis is the result of work I have carried out since the commencement of my higher degree by research candidature and does not include a substantial part of work that has been submitted to qualify for the award of any other degree or diploma in any university or other tertiary institution. I have clearly stated which parts of my thesis, if any, have been submitted to qualify for another award.

I acknowledge that an electronic copy of my thesis must be lodged with the University Library and, subject to the policy and procedures of The University of Queensland, the thesis be made available for research and study in accordance with the Copyright Act 1968 unless a period of embargo has been approved by the Dean of the Graduate School.

I acknowledge that copyright of all material contained in my thesis resides with the copyright holder(s) of that material. Where appropriate I have obtained copyright permission from the copyright holder to reproduce material in this thesis and have sought permission from co-authors for any jointly authored works included in the thesis.

Publications during candidature

Peer-reviewed papers

1. M. Sheliakina, A.B. Mostert, and P. Meredith. An all-solid-state biocompatible ion-to-electron transducer for bioelectronics. *Materials Horizons*, 2018. 5(2): p. 256-263.

2. Andrew J. Clulow, A. Bernardus Mostert, Margarita Sheliakina, Andrew Nelson, Norman Booth, Paul L. Burn, Ian R. Gentle and Paul Meredith. The structural impact of water sorption on device-quality melanin thin films. *Soft Matter*, 2017. 13(21): p. 3954-3965.

Conference abstracts

1. Margaryta Sheliakina, Bernard Mostert, Paul Meredith. Skin pigment-based solid-state organic electrochemical transistor. // Asilomar Bioelectronics Symposium. – 2017.
2. Paul Meredith, Bernard Mostert, Margaryta Sheliakina, Damon J. Carrad, Adam P. Micolich. Towards bioelectronic logic // Proc. SPIE 9944, Organic Sensors and Bioelectronics IX. – 2016.
3. Paul Meredith, Margaryta Sheliakina, Bernard Mostert. Melanin –spin behaviour and implications for bioelectronic devices. // Organic Sensors and Bioelectronics VIII "SPIE". – 2015.

Publications included in this thesis

M. Sheliakina, A.B. Mostert, and P. Meredith. An all-solid-state biocompatible ion-to-electron transducer for bioelectronics. *Materials Horizons*, 2018. 5(2): p. 256-263 – incorporated as Chapter 4.

Contributor	Statement of contribution
Author MS (Candidate)	Designed experiments (40%) Collected Data (95%) Analysed Data (80%) Interpreted the Data (30%) Wrote and edited the paper (40%)
Author ABM	Designed experiments (30%) Collected Data (5%) Analysed Data (20%)

	Interpreted the Data (40%) Wrote and edited paper (40%)
Author PM	Designed experiments (30%) Interpreted the Data (30%) Wrote and edited paper (20%)

Andrew J. Clulow, A. Bernardus Mostert, Margarita Sheliakina, Andrew Nelson, Norman Booth, Paul L. Burn, Ian R. Gentle and Paul Meredith. The structural impact of water sorption on device-quality melanin thin films. *Soft Matter*, 2017. 13(21): p. 3954-3965 – incorporated in Chapter 2.

Contributor	Statement of contribution
Author AJC	Designed experiments (40 %) Collected Data (45 %) Analysed Data (85 %) Interpreted the Data (35 %) Wrote and edited the paper (25 %)
Author ABM	Designed experiments (30 %) Collected Data (45 %) Interpreted the Data (30 %) Wrote and edited paper (25 %)
Author MS (Candidate)	Designed experiments (10 %) Interpreted the Data (10 %) Wrote and edited paper (10 %)
Author AN	Designed experiments (15 %) Collected Data (10 %) Analysed Data (15 %) Interpreted the Data (20 %) Wrote and edited paper (15 %)
Author NB	Designed experiments (5 %) Wrote and edited paper (5 %)
Author PB	Wrote and edited paper (5 %)
Author IRG	Wrote and edited paper (5 %)
Author PM	Interpreted the Data (5 %) Wrote and edited paper (10 %)

Submitted manuscripts included in this thesis

No manuscripts submitted for publication.

Other publications during candidature

No other publications.

Contributions by others to the thesis

The work reported in this thesis was carried out under the supervision of Prof. Paul Meredith and Dr. Bernard Mostert. Prof. Paul Meredith had significant contributions to the conception and design of the thesis project and interpretation of the experiments. Dr. Bernard Mostert setup the hydration dependent conductivity experiments, and had significant contribution to the interpretation of the data. X-ray photoelectron spectroscopy (XPS) scans were collected, and analysed by Dr. Barry Wood. Neutron Reflectometry experiments were performed by Andrew Clulow, Bernard Mostert, Andrew Nelson and Norman Booth.

Statement of parts of the thesis submitted to qualify for the award of another degree

None

Research Involving Human or Animal Subjects

No animal or human subjects were involved in this research

Acknowledgements

The work presented here wouldn't have been possible without a lot of support and kindness from many people. I would like to take this opportunity to express my gratitude towards all the beautiful souls who shared this path with me. I deeply thank everyone who didn't stop believing in me throughout all these years of work.

Firstly, I would like to thank my supervisor Paul Meredith. For all your encouragement and advice, for the time spent at the meetings, for all the inspiration you gave me when I needed it the most, I am very grateful. Paul was brave enough to accept my application when I was running from another PhD I had started and he supported me when I was in turmoil about giving up on this one as well. Your positive attitude and priceless jokes lifted my spirit up every time I thought my results weren't good enough. I would also like to thank Paul for allowing me the opportunity to visit UNSW and the Asilomar conference. Both gave me a chance to learn and grow as a scientist, make professional connections and friends for life.

Next, I would like to thank my second supervisor Bernard Mostert for all the time he spent in the lab with me, sharing his experience and sometimes explaining the basics. Your patience and soft personality helped to extinguish my at times fiery character. I specifically would like to mention the Asilomar conference, when I only had a few hours to prepare a talk and you were there to cover my back and make sure I would do a decent job, even though we both had a lack of sleep. It meant a lot to me and I feel blessed to have you as my supervisor for all these years. I wish you all the very best in your academic career. You are one of the brightest people I know and I am sure it won't be too long before I see you somewhere on TV and will proudly tell my friends that I had the honour to know you.

I express my gratitude to all other friends in academia who were always available to give advice or explain something to me. To Ardalan, a brilliant mind and a kind soul, who took time to share his knowledge in impedance spectroscopy and Origin functions. I really appreciate all the comments and questions you asked, which helped me keep an open mind and never stop learning. To Adam Micolich who took me under his wing for two weeks in the UNSW. I appreciate the time you spent to share your endless knowledge in device Physics. To Aren, a fellow PhD student, a housemate and a friend. Your jokes and charisma were always there to cheer me up, even in the darkest times. Thank you for being who you are and I wish you a good luck in whatever path you choose to follow. I would also like to mention all COPE members whom I crossed paths with. I appreciate all the help you gave me in learning about different equipment during my first year.

This journey wouldn't be enjoyable without many friends whose presence and love brightened up many days of routine-full work. I would like to thank my office mates Anatolii, Andrew and Ale

for the chats, laughs and many chocolates shared together. Your support gave me strength to keep going when I was ready to give up. The passionate dedication you have for science has kept me inspired. Thank you Ale for the Spanish lessons, for taking care of Frisbee and for the light you carry inside you. Thank you Anatolii for understanding me at times when I felt like no one would, our conversations helped me to better understand myself and be a better person. Also, thank you for the tea. Thank you Andrew for your love, patience and many, many balloon animals. Your warmth and ability to forgive taught me some valuable lessons.

Thank you to my friends from Woodford, rock-climbing gyms and sharehouses. I learnt a great deal from all of you. Not just how to be a more loving and kind person, but also how to build with bamboo, practice yoga, and party in Australian style. Each of you is an interesting individual, passionate about something. I am grateful that you shared a bit of that passion with me and I will keep it in my heart. I would also like to thank my friends in Swansea for the fun camping and rock-climbing trips we have done together and for enormous amount of the board games you taught me. You made me feel at home and made my time in Swansea very pleasant.

I would also like to thank my special friend Torren. We had so many ups and downs, it's hard to count. Nevertheless, our connection means a lot to me and I will have a lot of happy memories of the time spent together. Thank you for being a respectful housemate, a great cook, an interesting travel companion, and a supportive friend. I am very grateful for the exercises and guitar lessons, frisbee games, help with expanding my vocabulary and taking care of me whenever you could. I appreciate deeply what you have done for me, especially in the first years of my PhD. I wish you to find yourself in this world and never stop being curious.

Last but not least, I would like to thank my family for all the effort they put into raising me. My mum and dad who never stopped believing in me and always encouraged me to pick the most ambitious goals in life. They never doubted me and told me that if I wanted to achieve something, I would. My sister Liza and brother Bogdan always challenged me with interesting questions, each in their own way. You all helped me to grow into an open minded, hard-working person. I love you all and I am very appreciative of everything you have done for me.

Finally, I am expressing my gratitude to the Universe. For sending into my life all the people and all the creatures, who have been present there for a long or a short amount time, and all those who couldn't be there but thought of me in a positive way. I believe there is a reason for everything and whilst this part of my journey is almost over, there are many more exciting things to come.

Financial support

This research was supported by an International Postgraduate Research Scholarship. Operational aspects of the project were supported by the Australian Research Council Discovery Project DP 140103653: Biocompatible Electro-Ionic Transduction.

Keywords

Eumelanin, OECT, charge transport, bioelectronics, solid-state, impedance spectroscopy, volumetric capacitance, biocompatible, semiconductor, transducer.

Australian and New Zealand Standard Research Classifications (ANZSRC)

ANZSRC code: 029901, Biological Physics, 10%

ANZSRC code: 020405, Soft Condensed Matter, 30%

ANZSRC code: 030607, Transport Properties and Non-equilibrium Processes, 50%

ANZSRC code: 030606, Structural Chemistry and Spectroscopy, 10%

Fields of Research (FoR) Classification

FoR code: 0299, Other Physical Sciences, 30%

FoR code: 1004 Medical Biotechnology, 20%

FoR code: 0204, Condensed Matter Physics, 40%

FoR code: 0306 Physical Chemistry (incl. Structural), 10%

Table of Contents

List of Figures & Tables

List of Abbreviations

OECT	Organic Electrochemical Transistor
MOSFET	Metal-Oxide-Semiconductor Field-Effect Transistor
PPy	Polypyrrole
PEDOT	Poly(3,4-ethylenedioxythiophene)
PSS	Polystyrene sulfonate
DNA	Deoxyribonucleic acid
DHI	5,6,-dihydroxyindole
DHICA	5,6-dihydroxyindole-2-carboxylic acid
HQ	Hydroquinone
SQ	Semiquinone
IQ	Indole quinone
QI	Quinone Imine
DOPA	3,4-dihydroxy-phenylalanin
HOMO	Highest Occupied Molecular Orbital
LUMO	Lowest Unoccupied Molecular Orbital
Cu^{2+}	Copper(II) cation
UV-O_3	UV-Ozone
UV-Vis	Ultra-Violet-Visible
OH	Hydroxyl group
COOH	Carboxyl group
H_2O	Water
D_2O	Deuterium oxide
AFM	Atomic Force Microscopy
DMSO	Dimethyl sulfoxide
XPS	X-ray photoelectron spectroscopy
NR	Neutron Reflectometry
SLD	Scattering length density
XRR	X-ray reflectometry
DC	Direct Current
AC	Alternating Current
EIS	Electrical Impedance Spectroscopy
IV	Current-Voltage
RC	Resistor-Capacitor
CELIV	Charge Carrier Extraction by Linearly Increasing Voltage
EGaIn	Eutectic Gallium-Indium
CPE	Constant Phase Element
R	Resistor
M_a	Modified Restricted Diffusion Element
Ag	Silver
M^+	Cation
HMDS	Hexamethyldisilozane
OFET	Organic Field Effect Transistor
ENODe	Electrochemical neuromorphic organic device
W	Width
L	Length
Cu-eumelanin	Copper-eumelanin
$CuCl_2$	Copper chloride
Cu(II)	Copper(II) cation
Ni^{2+}	Nickel(II) cation

Co^{2+}	Cobalt(II) cation
Mn^{2+}	Manganese(II) cation
Fe^{2+}	Iron(II) cation
Zi^{2+}	Zinc(II) cation
Cl	Chlorine
V_g	Gate voltage
V_d	Drain voltage
I_g	Gate current
TOS	Tosylate
p(g2T-TT)	Poly(2-(3,3´-bis(2-(2-(2-methoxyethoxy) ethoxy)ethoxy) [2,2´-bithiophen]-5-yl)thieno[3,2-b] thiophene)
p(gNDI-g2T)	Poly((ethoxy)ethyl 2-(2-(2-methoxyethoxy)ethoxy)acetate)-naphthalene-1,4,5,8 tetracarboxylicdiimide-co-3,3´-bis(2-(2-(2 methoxyethoxy)ethoxy) ethoxy)-(bithiophene))
PdH_x	Palladium hydride
Ag/AgCl	Silver-Silver chloride

1. Background

1.1. Introduction to Bioelectronics

In the last twenty years, the field of organic electronics has experienced tremendous growth, driven mainly by the development of organic light emitting diodes for display applications [1, 2]. This was followed by the development of organic thin film transistors for flexible circuitry and sensors, and of organic photovoltaics for solar energy harvesting [1, 2]. Investigation of organic electronic materials have led to new concepts, which delivered stand-alone sensing and control systems, targeting management of energy consumption, medical interventions, the environment and communications. These systems include components that require low power consumption and which can be integrated into a wide variety of materials (such as building fabrics, biological tissues or natural environments) [3].

A new emerging subfield within organic electronics is the field of bioelectronics. The main aim in this field is the focus on the development of *in situ* real-time health monitoring with integrated biosensors, tissue repair, drug delivery and cellular-level controls. The key requirements for this field impose even greater challenges on the materials, and which include bio-compatibility, mechanical flexibility, low power consumption and minimal environmental footprint to achieve a medical outcome [4, 5].

Bioelectronics is focused on creating new materials and devices which would function by directly reading or writing biological signals combined with conventional semiconductor-based electronics [3, 4, 6-9]. In biology, electrical currents are primarily driven by the flow of ions (the smallest of which is the proton), rather than electrons, which are the charge carriers in semiconductors and metals. The physics of both ion currents and electron currents are individually very well understood – albeit it from quite different perspectives and by different scientific communities (Table 1.1). Ions are large effective mass entities that are usually treated classically: for example utilizing the Stokes–Einstein Relation, classical thermodynamics, and the interplay of ion motion with large scale material structural perturbations [10, 11]. Electrons are quantum mechanical entities whose motions are strongly affected by local structure and disorder as famously articulated by Mott and Davis [12]. There are certain cross-over elements in their physics, for example considerable evidence is emerging that protons can “tunnel” [13], and electrons when strongly localized can “hop” almost classically site-to-site [14]. However, in the main, the two charge carriers remain separated in their physical behaviour and the study of their common behaviour and collective transport in the solid-state remains challenging [3].

Bioelectronics has to date largely focussed on conjugated polymers and small molecules, which exhibit semiconductivity due to their delocalized π-electrons (collectively organic semiconductors)

[3]. The semiconductivity arises from many partially filled states with energies near their Fermi level. Organic semiconductors can be doped *p*-type or (less frequently) *n*-type to reach high conductivity by adding a chemical that either oxidizes or reduces the π-conjugated structure. A change in the doping state (also called redox status) [3] can also be achieved when ions from an electrolyte (or other source) enter an organic semiconductor film, or vice versa. In this case the compensating electronic charge is supplied by a metal contact and the process is called "electrochemical doping". The physics of these systems is very rich and continues to attract a great deal of attention, particularly in the emergent area of bioelectronics [7].

Behaviour	**Ionic material**	**Electronic material**
Transport mechanism	Centre of mass diffusion ("Vehicle mechanism") Hopping ("Grotthus mechanism")	Tunnelling or hopping between localized states
Charge carrier mobility	10^{-5} – 10^{-2} cm^2/Vs	10 – 10^5 cm^2/Vs
Electrodes	Most electrodes are proton blocking	Most electrodes are electron transparent
Device switching rate	Milliseconds to seconds (Neuron switching is about 10^{-3} sec)	Down to nanoseconds
Trapping	Inter- or intramolecular (chemical)	Localised states within the gap
Examples	Acids, Bases, Salts, Ice, Nafion	Silicon, Fullerenes, PEDOT, Pentacene

Table 1.1. The physics of ionic and electronic materials – a brief summary relating to transport.

Since the signal carrying currents in biology (ions) and semiconductors (electronic) are different, the key challenge is therefore the development of biocompatible interfaces that can support and transduce both types of current, which are governed by their very different physics. Transduction can be achieved either using two separate media, one supporting ionic and the other electronic signals, connected via a suitable device architecture, or alternatively a single media supporting both types of current.

A number of transducing device architectures have been reported: 1) bipolar ion junction transistors, which are basically the ionic analogues to the semiconductor bipolar junction transistors. The operational mechanism of such devices involves the amplification of a cationic collector current by an anionic base current. Bipolar ion junction transistors have been used for delivery of neurotransmitters and showed efficacy in modulating neuronal cell signalling [15]. 2) Membrane

coated nanowires, which are silicone oxide nanowires modified with a polymer, providing a surface that can undergo protonation and deprotonation. The small size of these nanowires provides sensitive, label-free, real-time detection of a wide range of chemical and biological entities and could be exploited in array-based screening and *in vivo* diagnostics [16]. 3) Proton field effect transistors, which are a hybrid platform that uses nanowires coated with a continuous lipid bilayer. It has been shown that these transistors can achieve ionic to electronic signal transduction by using voltage-gated or chemically gated ion transport through the membrane pores [17]. 4) Finally, a recently developed technology, Organic Electrochemical Transistors, OECTs [9].

Organic semiconductors are viewed as promising for transduction purposes for several reasons: 1) they are low cost, can be made into flexible form factor devices [18], can sustain ionic and electronic currents [19] and can be biocompatible [20, 21]; 2) they offer facile chemical modification and make oxide-free interfaces with electrolytes [22, 23]; 3) being "soft" materials, they allow significant ionic motion at room temperature [24]; 4) in organics, excitation couples strongly to the structure of the molecule (doping/de-doping effects not only electrical, but also optical and mechanical properties of the film).

Organic conductors that can support ionic transport are another promising alternative strategy and examples include: PEDOT:PSS (poly(3,4-ethylenedioxythiophene) doped with poly(styrenesulfonate)), polyaniline, melanins, proteins and polysaccharides.

To date, the most widely used strategy to create transducing elements is to utilise a device platform known as the organic electrochemical transistor (OECT). OECTs appear to be the best candidates for medical applications.

The following sections introduce the background and a more detailed view of current understanding on Organic Electrochemical Transistors (Section 1.2). This is followed by a description of chemical, biological and physical properties (Section 1.3) of a particular material system, eumelanin, which was studied because of its potential to be a part of a model bioelectronic system. The aims and motivation are presented in section 1.4.

1.2. Organic Electrochemical Transistors (OECTs)

The Organic Electrochemical Transistor, or OECT, were first demonstrated by White et al. [5]. In their reported work, the conductivity of a film of the semiconducting polymer polypyrrole was modulated by ions via the application of a gate voltage through an electrolyte. The resulting behaviour demonstrated transistor-like behaviour. OECTs are similar in design to organic field effect transistors, however the switching is controlled by an electrochemical doping or de-doping mechanism changing the carrier density in the transistor channel. The key difference of the OECT architecture is that it gates via volumetric capacitance, meaning that the gating ions interact with electrons in the volume

of the channel. Because of this feature, applying low gate voltages can produce large modulations in the drain current, a key advantage vis-à-vis organic field effect transistors. This makes OECTs efficient switches and powerful amplifiers. Even though Si-based systems have such advantageous characteristics as thermal and mechanical stability, long lifetime and high charge carrier mobility (due to the crystalline structure of Si), organic semiconductors offer a range of useful characteristics, such as: facile chemical modification; possibility of low temperature processing; oxide-free interfaces with aqueous electrolytes; and support of efficient ion transport at room temperature. Furthermore, using electrolytes instead of metal-oxide-semiconductor capacitors makes it possible to create diverse device architectures and in combination with a variety of substrates, allows a wide range of fabrication techniques. Moreover, the tunability of organic molecules enables the optimization of ion and electron transport for biofunctionalization [25]. By virtue of these properties, OECTs are being exploited in a wide range of applications, such as neural interfaces [26, 27], chemical and biosensors [8, 28] and printed circuits [29, 30]. One disadvantage of the OECT architecture is the slow switching speed. However, most of described applications, including bioelectronics, don't require high speeds.

Similarly to MOSFETs and OFETs, OECTs show switching behaviour, where the gate voltage (input) controls the drain current (output). OECTs can also be considered as amplifiers, where the power of an input signal is amplified on the way to the output [26].

More detailed discussion on the mechanistic behaviour of the OECTs will be presented in Chapter 4.

1.2.1. Electrolyte-based OECTs

Figure 1 shows a schematic of a typical OECT. The basic elements of the transistor are: a *p*-type semiconducting channel in contact with a liquid electrolyte; an electrode (the gate), immersed in the electrolyte; and a metal source-drain contacts defining the channel.

The operation of a basic liquid-gated OECT is controlled by voltages applied to the gate and drain, which are referenced with respect to the source electrode. The gate voltage controls the injection of ions into the transistor channel and hence, the "doping" state of the organic thin film (and its conductivity). The drain voltage induces a source-drain current, which is proportional to the quantity of the mobile charge carriers in the channel [31].

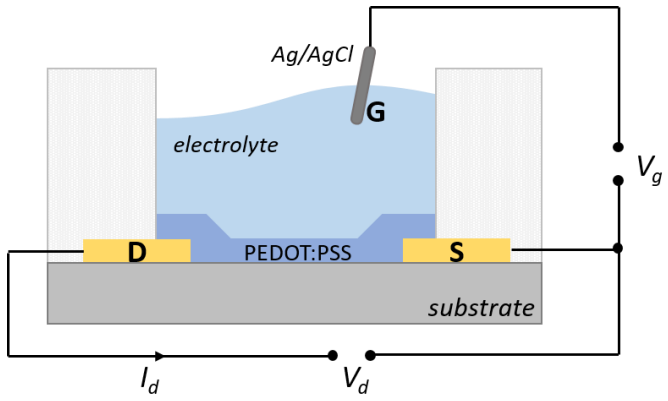

Figure 1.1. A schematic structure of an electrolyte-based OECT. The source (S), drain (D) and gate (G) contacts are labelled. Adapted from [26].

The major disadvantage of the state-of-the-art OECTs is the presence of the liquid electrolyte gate in their structure. Despite the fact that most biological systems function in a wet environment, an ideal OECT device should be solid-state, delivering stability, long term operation, and most importantly miniaturization and integration. The ultimate goal is to create bioelectronic interfaces which could not only perform read–write functions but also amplify, signal process or even compute [32]. This requires the combination and large scale integration of literally millions of individual components and the realization of low power consumption bioelectronic logic. The use of electrolytic or ionic gels or liquids as transducing gates is likely not compatible with such a vision, and hence the realization of scalable all-solid-state architectures is now a priority in bioelectronics. The work described in this thesis is motivated by this priority.

1.2.2. The model channel materials for OECTs

Transducing between electronic and ionic currents is a non-trivial task due to the different physics of the charge carriers as mentioned above. Furthermore, as described in section 1.1, the preferred materials should be organic in nature. With these conditions in mind, it should be noted that there is a lack of materials that can carry both electronic and ionic currents. Most of these materials are some form of inorganic hard material (for instance, oxides used in memristors [33]). Hence most strategies focus on creating devices that would host two materials (or media), each supporting the different charge carrier type [6-8].

At this point it should be noted that organic materials that are able to support high mobility ion currents in the solid state are also few in number. Some of the examples include Nafion and other polymer electrolytes [11, 34-37]. However, it is not clear whether these materials are biocompatible by nature.

Turning to the electronic media, the most common material used in the conductive channel for OECTs is usually based on PEDOT or polypyrrole (PPy), doped with p-type dopants such as small

anions or polyanions (Figure 1.2a,b). These materials are synthesized by solution, vapour-phase or electrochemical polymerization [25]. For example, when combined with the dopant PSS, PEDOT shows good redox stability and high electronic conductivity. Furthermore, and critically for OECT device operation, in the presence of foreign cations, the PEDOT:PSS conductivity is de-doped, which is the transduction mechanism (Figure 1.2).

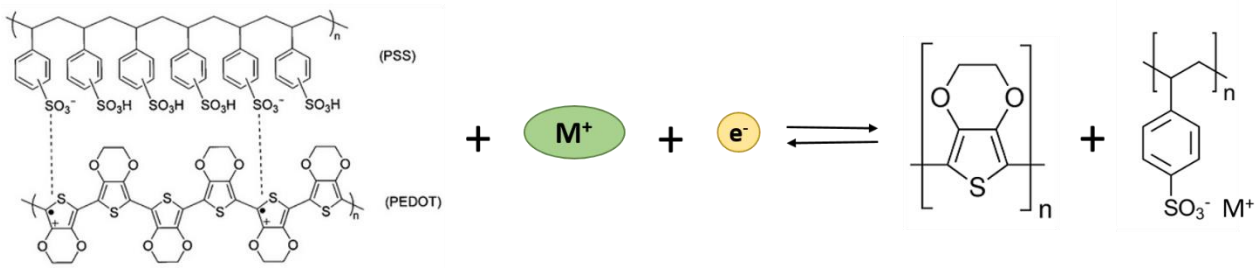

Figure 1.2. A schematic representation of the electrochemical reaction which leads to the de-doping of PEDOT:PSS.

PEDOT:PSS is so versatile that OECTs based upon it have been demonstrated in a wide variety of situations such as sensors, being successful in detecting such biological entities as enzymes [38], DNA [39] and antibodies [40]. Furthermore, PEDOT:PSS based OECTs have already been used in medical settings for prototype testing [41].

Apart from the aforementioned materials, a wide variety of electrolytes (both, gels [42] and solids[43]), and different gate electrodes, such as traditional polarizable electrodes and nonpolarizable electrodes [44] as well as non-traditional materials (such as PEDOT:PSS [43] and different forms of carbon [45]), have been used to fabricate OECTs. The choice of material is usually dictated by the application or limitations of the fabrication process.

To summarise, OECTs are devices that are similar to OFETs, however they have different mechanisms of operation. Their key advantages are high transconductance, stability in aqueous electrolytes, sensitivity and biofunctionalization. These qualities make OECTs ideal platforms for bioelectronic applications. All reported devices to date have a liquid electrolyte as a gate which makes the miniaturization of devices very challenging, hence the next step in advancing the technology is creating a solid-state OECT.

There is a variety of materials that can be used as a channel of OECTs. In the work described here PEDOT:PSS was utilised for this purpose, mainly due to its availability and well known properties. Eumelanin was used as a gate material due to its biocompatibility and various phisico-chemical properties, which will be described in the next sections.

1.3. Melanins

Melanins are a group of pigmentary macromolecules found throughout nature in a variety of organisms ranging from humans to bacteria. The word "melanin" came from a Greek word *μέλαζ*, which means "black, dark" and was first described by Aristotle [46]. There are four main pigments included in this group: 1) Eumelanin, the black-brown pigment made from two main chemical building blocks: 5,6-dihydroxyindole (DHI) and 5,6-dihydroxyindole-2-carboxylic acid (DHICA) and their various oxidative states (Figure 1.3).

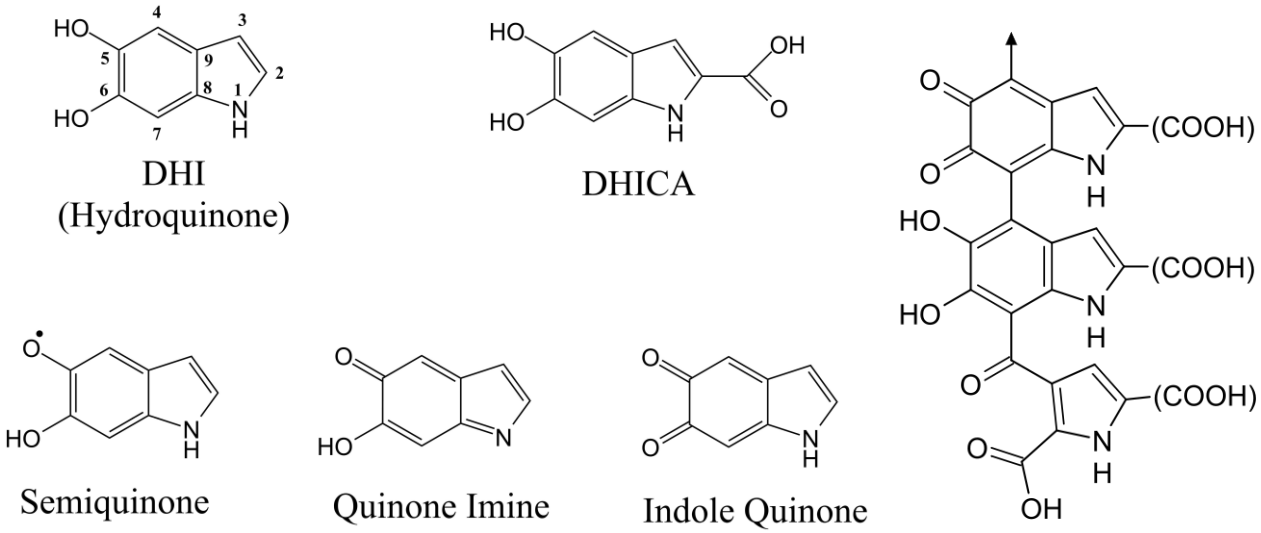

Figure 1.3. Monomeric components of eumelanin (on the left): 5,6-dihydroxyindole (DHI), 5,6-dihydroxyindole-2-carboxylic acid (DHICA) and the oxidative states of DHI (semiquinone radical (SQ), indole quinone (IQ) and quinone imine (QI)) [47]. The numbering indicates the reactive positions of the molecule. A part of the structural molecule of eumelanin is presented on the right. (COOH) can be COOH or H, or other substituents. The arrow shows where the other monomers attach.

It has been found in the skin, hair, irises of mammals [48] (Figure 1.5), the inner ear [49] and the brain stem (*Substantia nigra*) as part of neuromelanin [50]; 2) Pheomelanin (or phaeomelanin) has a pink to red hue, and is mainly found in red haired individuals' hair and skin [51]. In terms of the chemical structure, pheomelanins differ from eumelanins in the synthesis pathway (Figure 1.4).

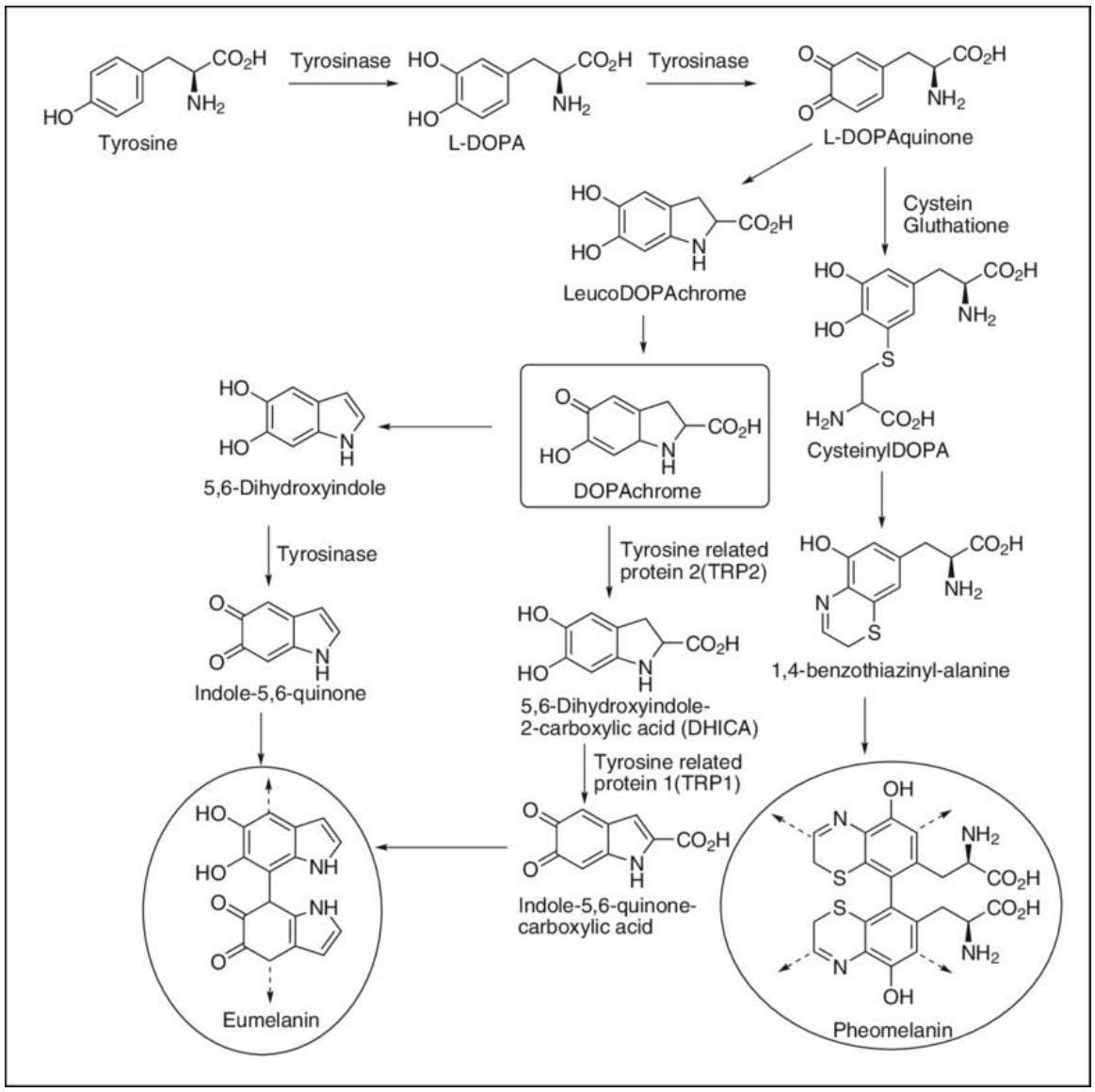

Figure 1.4. Biosynthetic pathways of eumelanin and pheomelanin. Figure adapted from [52].

In the body L-Dopa reacts the same as per eumelanin formation, however, after dopaquinone formation the amino acid L-cysteine is incorporated into the synthesis. As a result, the synthesis proceeds to form an oligomer structure, similar to eumelanin, but with benzothiazine and benzothiazole units forming the mass of the material instead of DHI and DHICA [53]; 3) allomelanin (which means "other" melanin) has been found in plants and fungi [54] and can be seen as the enzymatic browning of fruits. Biosynthesis of allomelanin includes the oxidation of indole-5,6-quinone by the enzyme polyphenol oxidase from tyrosine and catecholamines [55]. 4) Neuromelanin is a dark insoluble polymer found in the brain stem (in specific populations of catecholaminergic neurons) [50]. Neuromelanin appears in particles, which have a pheomelanin core and eumelanin outer shell. It appears that *in vivo* as pheomelanin is formed, the cysteine becomes depleted and the pathway switches over to eumelanin [56]. Interestingly, humans have the largest amount of neuromelanin of all primates, and it is totally absent in many other species [57]. Even though the

biological function of neuromelanin is not fully understood, it has been shown that it effectively binds transition metals such as iron, and other potentially toxic molecules. Hence, it may play a role in apoptosis and Parkinson's disease [58].

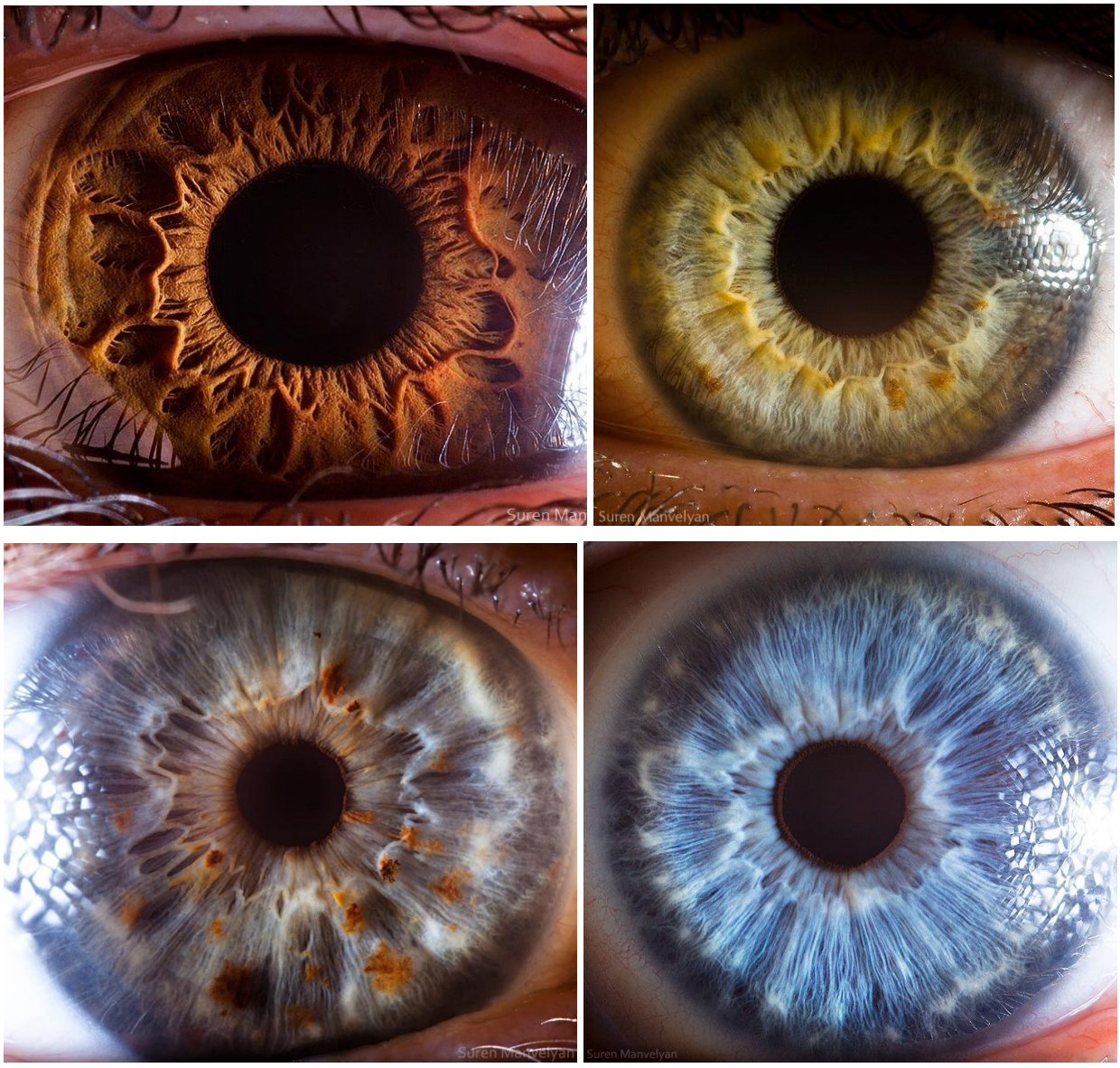

Figure 1.5. Close-up photographs of a human eye. Iris, containing different concentrations of eumelanin can be seen. Photo credit: Suren Manvelyan via http://www.surenmanvelyan.com.

As previously mentioned, melanins are found in a diverse range of animal species. For example, melanin synthesis in microorganisms is often associated with numerous survival mechanisms, it can serve as an energy transducer and effect cellular integrity. Some animals use melanins for sexual display and mimicry (camouflage) [59]. Melanin also plays an important role in the innate immune system of insects [60]. Bacterial melanin was shown to speed up motor recovery after damage in the central nervous system of humans [61, 62]. One of the main roles of the melanin in mammals is believed to be its resistance to UV radiation. In this regard it has been commercially used in photoprotective creams and sunglasses [63, 64].

Eumelanin is considered the archetype of the melanins, and the names “melanin” and “eumelanin” are used interchangeably in the literature [65, 66]. The work presented in this thesis is focused on eumelanin and to avoid any confusion, the properties of only this type of the melanin will be described hereafter.

1.3.1. Eumelanin structure and biological properties

Eumelanin is the most studied melanin due to its natural abundance [67], implication in melanoma skin cancer [68] and a diverse and unique collection of physiochemical properties [47]. In terms of biological role eumelanin provides photo-protection, antioxidant action, metal chelation, and free radical scavenging [47, 69]. The protective property of eumelanin is due to its ability to absorb and scatter the high energy photons from the UV and blue part of the solar spectrum [47]. As a biomaterial, eumelanin is inherently biocompatible, which is a very important property of any viable organic bioelectronic material [70].

As was mentioned above, eumelanin is a heterogeneous macromolecule arising in part from the polymerization of L-dopa via 5,6-dihydroxyindole (DHI) and 5,6-dihydroxyindole-2-carboxylic acid (DHICA) and their various redox forms. The final polymer is essentially a heterogeneous polymer of these monomers that bind via the 3, 4 and 7 positions and simpler entities to form small oligomeric sheets [71]. In turn, these stack to form colloidal particles. One of the major challenges in studying eumelanin is the lack of adequate methods for the isolation of the pure pigment. Remarkably little is known about the structure of eumelanin despite its abundance in the global biomass [48, 68]. This is due to the inability of current biochemical and biophysical techniques to provide a definitive chemical structure, because this complex polymer is amorphous, insoluble, and not amenable to either solution or crystallographic structural studies [52].

Eumelanin can be obtained by chemical [72] and microbiological synthesis [73] or by extraction from animal tissues [48]. In mammals, pigment synthesis, storage, and transport occur in lysosome-related organelles – melanosomes. Interestingly, although the biochemical synthesis of eumelanin is common to all pigmented tissues, melanogenesis is regulated differently among the different tissues. For example, in hair, melanogenesis occurs only during the active phase of the hair growth cycle in melanocytes located exclusively in the hair bulb, while in skin, for instance, eumelanin is continuously produced [74]. The eumelanin-forming enzyme tyrosinase is the major catalyst responsible for melanogenesis. The very first step of eumelanin synthesis begins with conversion of phenylalanine to tyrosine with the help of the enzyme phenylalanine hydroxylase. This process takes place in the liver. The rest of the synthesis occurs within the melanocyte’s melanosome, where L-tyrosine firstly oxidises to 3,4-dihydroxy-L-phenylalanine (L-DOPA) by tyrosinase and then L-DOPA oxidises to dopaquinone, catalysed by the same enzyme. From dopaquinone, the eumelanin

synthesis pathway diverges from the synthesis of pheomelanin. Dopaquinone is converted to dopachrome through auto-oxidation of leucodopachrome. Eventually dopachrome is converted to 5,6-dihydroxyindole in the presence of dopachrome tautomerase and dihydroxyindole-2-carboxylic acid oxidase (DHICA). In the last step 5,6-dihydroxyindole oxidises to indole-5,6-quinone by tyrosinase and forms eumelanin [52].

The synthesis described above is for *in vivo* situations and it is quite complex. It leads to the incorporation of various materials such as proteins, peptides, salts etc. However, a "clean" analogue of eumelanin can be synthesised much more easily in the laboratory, as schematically presented in Figure 1.6. This will further be described in Chapter 2.

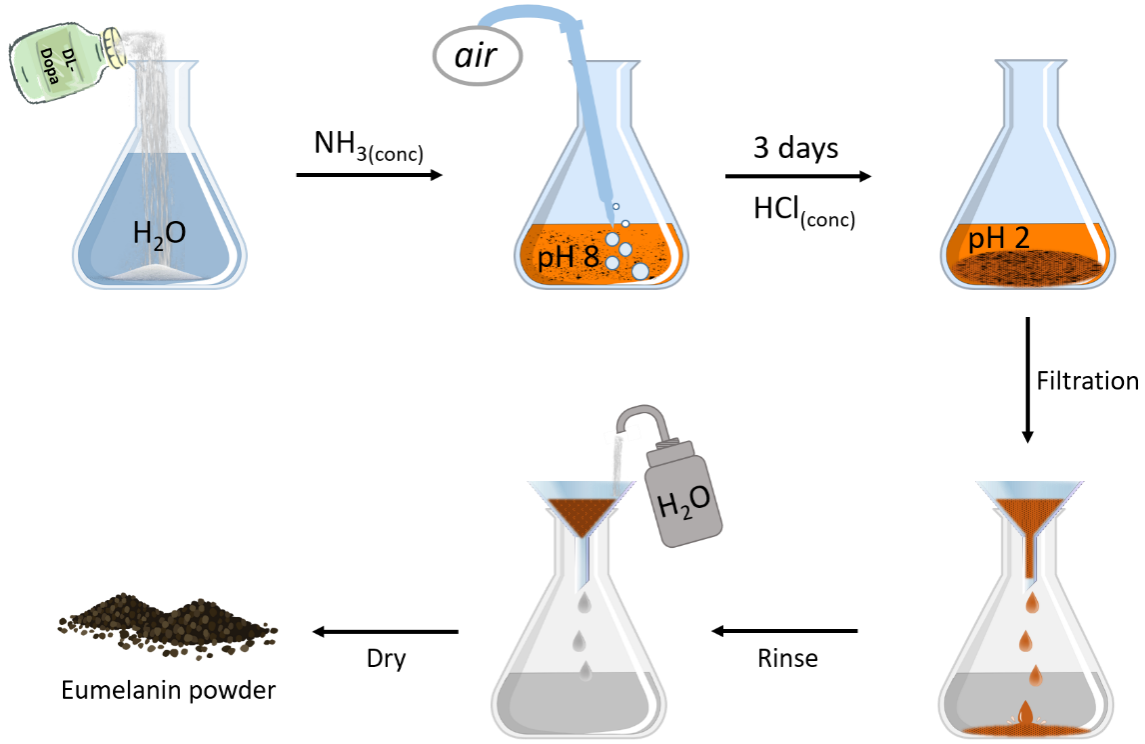

Figure 1.6. Schematic representation of the eumelanin synthesis in the laboratory.

1.3.2. Optical properties

Eumelanin has an interesting and rather unique collection of physico-chemical properties, one of which is a featureless broadband optical absorption, and almost unity non-radiative conversion of absorbed photon energy [3].

It is unusual for an organic material to have a featureless broad absorption spectrum (See Figure 1.7) [75] and many attempts have been made to explain this phenomena in eumelanin. It was believed by many authors that scattering may play a significant role [75], since eumelanin is known to be a fine colloidal suspension in solution. However, recently it has been shown that scattering contributes less than 6% to the total absorbance across all wavelengths in the UV and visible spectrum [76]. As such, most of the absorbance is electronic in nature.

Given the electronic nature of the absorbance, the optical properties have been explained using a chemical disorder model that was proposed by Tran *et al.* [77]. This disorder model suggests that the absorption spectrum is essentially a superposition of many individual absorbances (which can be modelled using Gaussians for example [47]), each corresponding to a different chemical species in eumelanin. Each of those species absorbs light at a different energy (wavelength) and has a various HOMO/LUMO (highest occupied molecular orbital and lowest unoccupied molecular orbital respectively) gaps. Since eumelanin is a highly disordered system, it contains a large number of possible species (chromophores). When all these absorbances are summed together (see Figure 1.7), the broad-band absorption spectrum emerges.

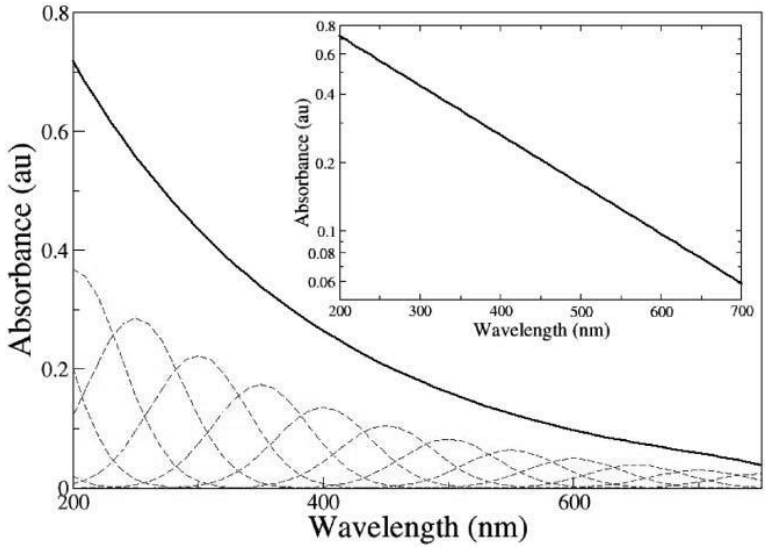

Figure 1.7. Simulated broadband UV-visible absorbance spectrum of synthetic eumelanin (solid black line). The dashed lines are the simulated absorbance of different chromophores. The inset shows a log-linear plot of the simulated broadband absorbance. Figure reproduced from Meredith *et al.* [78].

Considering the above, it is clear that eumelanin should not be thought of as a standard conductive organic electronic material. In the next section it will be shown that its electrical properties are reflective of its optical properties.

1.3.3. Electrical properties

Since McGinness *et al.* [79] discovered apparent resistive switching behaviour in eumelanin, it was considered as an amorphous semiconductor. A peculiar feature of eumelanin conductivity is its dependence upon the state of hydration (higher water contents delivering higher electrical conductivities). This was first explained in the 1970s using Rosenberg's theory based upon the idea that water is capable of modifying the local dielectric constant of semiconducting organic systems. In a traditional semiconductor, carriers can be thermally activated from the valence band to the

conduction band, and the temperature dependent electrical conductivity [σ (T)] is given by the Arrhenius equation:

$$\sigma(T) = \sigma_0 exp\left(-\frac{E}{2kT}\right), \qquad \text{Eq. 1.1.}$$

where, σ_0 is the so-called pre-exponent, E is the energy gap (activation energy) between the conduction and valence band, k is Boltzmann's constant and T is the temperature [80]. In the presence of water Rosenberg's modification appears:

$$\sigma\ (T) = \sigma_0 exp\left[\frac{-E_D}{2kT}\right] exp\left[\frac{e^2}{2kTr}\left(\frac{1}{\kappa} - \frac{1}{\kappa'}\right)\right], \qquad \text{Eq. 1.2.}$$

where, σ_0 is the dry conductivity in the infinite temperature limit, E_D is the energy gap of dry eumelanin, r is the screening length, κ is the dielectric constant of dry eumelanin, and κ' is the effective dielectric constant of eumelanin due to the presence of water.

Essentially, as water is added, the average dielectric constant increases leading to a reduction in the effective energy gap. This also allows for the resistive switching behaviour to emerge at voltages lower than breakdown, which is an archetypal signature of amorphous semiconductivity [47].

To account for the hydration dependent behaviour of eumelanin, Mostert *et al.* [81] proposed a series of experiments, which demonstrated that the origin of eumelanin conductivity is a redox chemical equilibrium, most likely dominated by protons. In the mechanism of Mostert *et al.* [81], upon absorption of water, free carriers are produced locally from a comproportionation reaction (Scheme 1.1), which drives the production of extrinsic free radicals (electrons) and hydronium ions (protons).

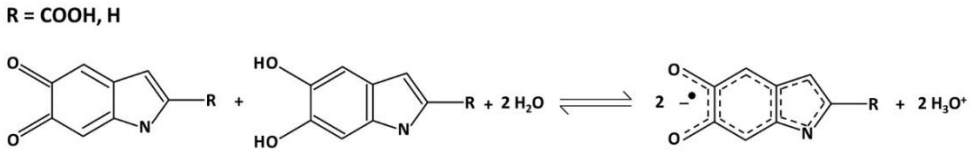

Scheme 1.1. The comproportionation equilibrium which dominates eumelanin electrochemistry. Quinone and Hydroquinone moieties react with water to form Semiquinones and hydronium [66].

The "chemical self-doping" presented in Scheme 1.1 leads to hybrid ionic-electronic behaviour and explains the exotic electrical properties of eumelanin. Given that eumelanin is a naturally occurring biomaterial, this opens up exciting possibilities to create bioelectronic interfaces and devices. The mechanism proposed by Mostert *et al.* [81] is in principle generic to other conducting materials with ionisable groups, and this has recently been confirmed by Zhong *et al.* [82] and Ordinario *et al.* [83] who have demonstrated fully ionic transistors based upon chitosan and synthetic proteins respectively. These are very exciting times for the development of bioelectronic interfaces and the field is undergoing explosive growth. Key to its continued success though is the acquisition

of accurate and predictive structure-property relationships and a firm foundation in the pertinent basic physics.

To summarise the above, eumelanin's electrical behaviour suggests that its dominant charge carrier is protonic by nature [66, 84]. Furthermore, eumelanin is a biocompatible material that allows one to produce high quality thin films. These properties make eumelanin a possible model candidate for acting as a solid state proton electrolyte for OECT purposes.

1.3.4. Eumelanin doping

As discussed previously, eumelanin shows potential as a solid-state protonic conductor for OECTs. An additional feature that enhances this potential is its ability to bind to different drugs and metal ions, which may act as dopants [85]. It has been shown that both natural and synthetic eumelanin bind the same metal ions with an affinity that depends on the valency of the metal. Eumelanin shows high affinity to numerous metal ions and there are several examples in the literature which prove that. For example, an accumulation of iron was observed in melanocytes of the eye iris [86], copper was found in neurons which contained neuromelanin [87], and calcium was found in the inner ear melanosomes [49]. The role of eumelanin in binding metal-ions seems important, as it makes molecular complexes with potentially poisonous substances and releases them later on in small, non-toxic concentrations [88]. However, another side to the role of eumelanin-metal binding process is the accumulation of toxic substances in the pigmented tissues, which leads to damage and loss of their normal function. For example, the accumulation of toxic metal-ions in an eye can cause cataract formations [88]. As eumelanin supposedly plays a dual role in both protection and harming the human cells, significant research has been put into investigation of these phenomena. It has also been demonstrated that eumelanin could potentially be used in drug delivery systems [89] and diagnostic imaging [90].

Although much research has been done in the binding properties of eumelanin, only a few studies investigated how the metal-ion complexes affect the chemical structure and physicochemical properties of eumelanin [47]. One of the most studied complexes is Cu-eumelanin. There are multiple reasons for this state of affairs. One is that natural eumelanin binds to copper (II) alongside other metal-ions, providing chemical protection to cells [87]. It has also been shown that Cu(II) is one of the most common metal-ions found in the brain, where it was bound to neuromelanin [87]. It is probable that such complexes play a major role in the development of Parksinson's and Alzheimer's diseases, when the neuromelanin become saturated with these metal ions. It was demonstrated that some of the features of these diseases include depleted eumelanin concentration and a high concentration of Cu(II) [91, 92]. Another reason Cu-eumelanin complexes are interesting is that Cu(II) is involved in the synthesis of natural eumelanin *in vivo*. As was mentioned earlier, to start the

process of biosynthesis, tyrosine has to be oxidised to dopaquinone (the precursor of eumelanin). For that to happen, the enzyme tyrosinase, which catalyses this process, has to be activated by Cu(II). However, copper has to be converted first from its inactive form (which is a Cu^{2+}-Cu^{2+} complex) into a Cu^{+}-Cu^{+} pair [93]. Furthermore, copper can also be a catalyst for converting dopachrome into DHICA, which is a key regulatory step in the biosynthetic pathway of eumelanin [94].

Cu(II) itself can be incorporated into the eumelanin structure in two ways, during biosynthesis and after eumelanin formation [88]. The chemical structure of the final copper-eumelanin complex depends on when the copper was bound to eumelanin [95]. Both, synthetic and natural eumelanin have a strong affinity for Cu(II), independent of its biosynthetic pathway via the copper containing enzyme.

In the eumelanin polymer, Cu(II) binds to semiquinone and deprotonated hydroxy groups on the hydroquinone. Considering this, the comproportionation reaction mentioned above can be modulated by something other than water, opening up possibilities for modifying eumelanin as a solid state proton conductor for OECT purposes. This matter will be further discussed in Chapter 5.

The conductivity of synthetic eumelanin is strongly dependent on its hydration state, increasing exponentially upon the addition of water by orders of magnitude [81]. Having the ability to modify the comproportionation reaction with copper ions would make the hydration dependent conductivity of eumelanin even more sensitive. The majority of eumelanin conductivity studies on natural or synthetic samples have been carried out without "doping" it with metal ions [71, 81, 96]. However, one study showed the conductivity response of eumelanin with added Cu(II) ions [97]. It is worth noting that the copper ions were added to eumelanin during its synthesis instead of post synthesis. The measurements were performed under vacuum conditions at room temperature (which means that eumelanin remained dry during the experiment) and no significant changes in eumelanin conductivity were found upon the addition of copper ions. Considering that the conductivity of neat eumelanin (without the addition of metal-ions) increases up to 1.5 orders of magnitude when increasing the water content from dry (vacuum) to wet (fully saturated) [81], the study mentioned above doesn't shed any light on the electrical properties of the eumelanin-metal complexes and more investigation of this phenomenon is necessary, including the effect of hydration.

1.3.5. Challenges in creating solid state OECTs

To re-iterate, ions are the predominant signal carrying entities in biology, whereas our everyday electronics are based upon electron/holes as the main charge carrier transported through semiconductors and metals. Thus, one of the key challenges explored within bioelectronics is the task of realising efficient communication and signal processing between ionic and electronic currents [9, 78].

It appears that the two media approach is most likely to succeed and an OECT architecture could deliver the best device geometry for such purposes. However, the key flaw in current OECT systems is that the majority of them are liquid based. For the reasons mentioned in Section 1.2 (providing stability, long term operation and miniaturization), an ideal OECT platform should be solid-state. The channel material of choice for use in such devices is PEDOT:PSS, since it is a well understood standard material for OECTs. To solve the issue with a liquid electrolyte, eumelanin is an excellent candidate to be used as a viable solid state equivalent. However, there are numerous challenges to anticipate in creating solid state OECTs, which are:

- The complexity and experimental difficulty in the investigation and understanding of the charge transport mechanisms in disordered organic conductors (natural and synthetic, ionic and semiconducting) [98, 99];
- The fabrication difficulties associated with the creation of a solid-state OECT based on an ionic conducting biomaterial such as eumelanin (solvent compatibility, definition of device architecture, interlayer stability, etc.) in combination with an organic semiconductor [100];
- The transient behaviour of potentially unstable OECTs which have hydration dependent behaviour;
- The challenge to improve device performance and reduce leakage currents;
- Integration of a biological component into a solid-state device [101, 102];
- It has been shown that doping eumelanin with metal-ions could change its electrical properties [103]. However, the change in the conductivity due to the metal-ion influence has not been fully investigated.

1.4. Aims and motivation

Bioelectronics is an emerging field at the intersection of biology and semiconductor electronics. A key scientific problem in this field is the efficient transduction between ionic and electronic signals. The work described in this thesis was motivated by this challenge. For this study a particular model system, eumelanin, was chosen due to its biocompatibility and capability of acting as part of a transducing element.

In this thesis will be presented an investigation and discussion on the basic properties of eumelanin thin films to provide understanding of its physics and chemistry. Then there will be a more applied focus on how this material can be incorporate into a solid-state system based upon an electrochemical transistor, which seems to be a suitable bioelectronics platform. The study described here is hoped to be a precursor to the development of bioelectronic logic, which should be the next natural step on the evolution of the field of bioelectronics.

2. Characterising Eumelanin Thin Films

2.1. Eumelanin Synthesis and Thin Film Fabrication

Auto-oxidized eumelanin was synthesized according to a standard literature procedure [104]. 3,4-Dihydroxy-DL-phenylalanine (D,L-dopa, Sigma-Aldrich, 5 g) was dissolved in 2 L of deionized water, subsequently adjusted to pH 8 using NH_3 (AnalaR, 25% NH_3 Merck). Air was then bubbled through the solution while stirring for 3 days. A drop of ammonia was added each day to maintain the solution at pH 8, which was measured using litmus paper. After 3 days, the solution was then adjusted to pH 2 using concentrated hydrochloric acid (Univar Analytical reagent HCl 32%), to precipitate the formed eumelanin. The aggregated solution was then filtered and washed multiple times with deionized water. The obtained black powder was dried overnight under ambient conditions.

To create a solution for thin film casting, eumelanin powder was re-dissolved in water and ammonia [70]. The composition of the new solution was ~0.7g eumelanin in 5 ml H_2O and 10 ml NH_3 (AnalaR, 25% NH_3 Merck). The solution was stirred for 1 hour at room temperature and ultrasonicated for 1 hour. The eumelanin solution was then spin-coated onto pre-treated glass substrates (see below).

Glass slides were purchased in 4 inch-wafers (Australian National Fabrication Facility) and diced into 14.9 mm x 14.9 mm substrates. The size was thoughtfully chosen to fit the slides into the evaporation holder plate for future experiments (the schematic of the plate is shown in the Appendix, Figure S2.1). The substrates were cleaned with Alcanox, rinsed in deionized water and ultra-sonicated in acetone (5 min). Afterwards they were rinsed with deionized water, ultra-sonicated in 2-propanol (5 min) and dried under a flow of nitrogen. The substrates were finally treated with UV-Ozone (MB UV-O_3, MBraun): 5 min of oxygen purging, followed by 20 min of UV exposure and 5 min of nitrogen treatment, and were ready for spin-coating. The eumelanin solution was filtered through a 0.45 µm PVDF/L filter (Simplepure) to eliminate larger particles and insure the homogeneity of the film. Then it was spin-coated (G3P Spincoater, Specialty Coating Systems) onto the substrates for 5 s at 500 rpm followed by 60 s at 1500 rpm. To obtain films of different thickness, the same solution was used, however, the spin-coating procedure was modified. Faster spin speeds (up to 2500 rpm) were used to create thinner films, while slower spin speeds (down to 1000 rpm) and shorter spin times were used to obtain thicker films.

Thicknesses of any formed films were measured using a Dektak XT (Bruker). Using a sharp needle, three scratches were made on each sample to check the film homogeneity. Vision 64 software was used to control the machine stylus and collect the data. The length of each run was 400 µm, the duration of each run 8 sec and the stylus force 3 mg.

2.2. UV-Visible Absorption (UV-Vis)

One of the key features of the eumelanins are their optical properties. It is unusual for organic material to have a featureless broad absorption spectrum [75] and many attempts have been made to explain this phenomena in eumelanins. It was believed by many authors that scattering may play a significant role [75] but later on it has been shown that it is not the case as scattering contributes less than 6% to the total loss across all wavelengths in the UV and visible spectrum [76]. Therefore, even though scattering effects are connected to the photoprotective function in eumelanin, the observed broad absorption must be due to basic electronic effects. To investigate the absorbance of eumelanin thin films a UV-Vis measurement was performed. For that purpose a UV-Vis-NIR Spectrophotometer 5000 (Varian) was utilised and Cary WinUV (Agilent Technologies) software was used to record the data. The absorbance of a eumelanin thin film spin coated onto a glass substrate was measured against a clear glass slide (which served to obtain a baseline). Figure 2.1(a) shows typical eumelanin thin film spectra. As can be seen, the spectra are essentially featureless and exhibit a decaying exponential behaviour as a function of increasing wavelength. This exponential behaviour is clearly illustrated in the inset where the data is plotted on a log-linear scale. Furthermore, it can be observed that the absorbance increases with increasing thickness with no essential change in the qualitative behaviour of the absorbance (Figure 2.1(b)). All of which indicates that the change in the absorbance is due to an increasing absorption length. The thickness of the films were determined after the UV-Vis measurements were completed.

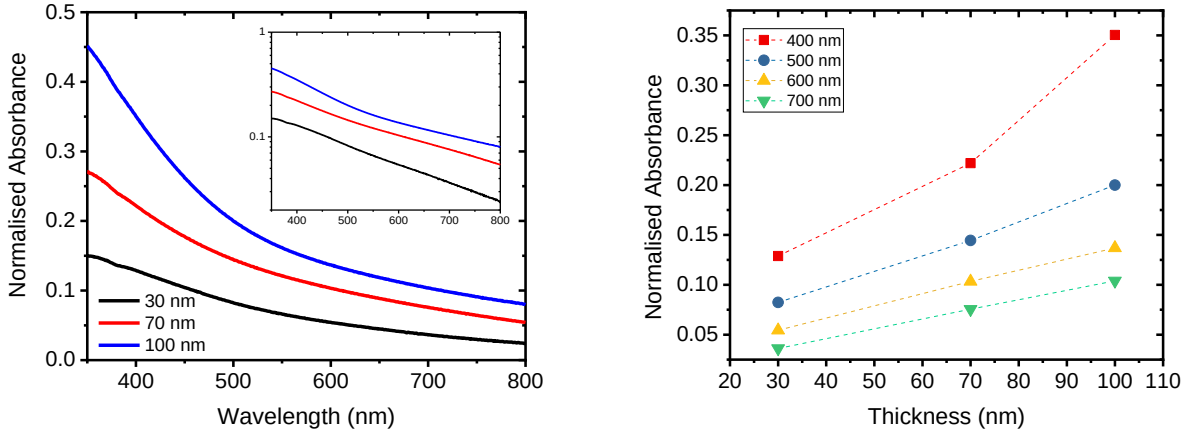

Figure 2.1. (a) The UV-visible absorption spectra of synthetic eumelanin thin films, as a function of thickness. The spectra follow decaying exponential behaviour as indicated by the inset, which is the data replotted on a log-linear scale. The data indicates that the eumelanin thin films show the same optical behaviour as eumelanin solutions. (b) The normalised absorption as a function of film thickness for different wavelengths. The full data set is presented in the Appendix (Figure S2.2).

As was highlighted in Chapter 1, the broad-band, featureless absorption spectra of eumelanin solutions is unusual for organic materials. For eumelanin, this profile is due to the overlapping

absorbances of different chromophores within the material (where distinct chromophores create specific spectral features), which when superimposed form the exponential curve. As can be seen from Figure 2.1, this same optical behaviour is preserved in the solid state morphology of thin films. Since melanins in general are defined more by their chemical origin and observed behaviour than their chemical structure [47], this would suggest that the thin films fabricated above can be considered a true eumelanin compound.

2.3. Atomic Force Microscopy (AFM)

To further characterise the eumelanin thin film properties in anticipation of device fabrication, the surface morphology was investigated using tapping-mode Atomic Force Microscopy (AFM). Eumelanin solutions were prepared, as described in section 2.1, and spun cast onto a range of different substrates including: mica, grade V-1 (ProSciTech); silicon wafers, (111)-orientation p-type with native oxide formed on the surface and surface resistance of 1-30 Ohm (ProSciTech); glass slides (ProSciTech) and silicon wafers with Si_3N_4 top layer (MMRC). Both types of silicon substrates and glass slides were pre-cleaned as described in section 2.1. to increase the hydrophilicity of the surface and improve the quality of the films. The top layer of the mica substrates was peeled off, and eumelanin solution was spin coated immediately without any further treatment of the surface. Different substrates were selected to see whether the eumelanin thin film morphology and roughness was substrate dependent. The thicknesses of the films were measured as described previously (section 2.1) and, across all samples came to 50 nm on average, which indicated that the fabrication process was consistent. The AFM utilised was an Asylum Cypher High Resolution. The cantilevers (Budget Sensors) used for imaging had a resonant frequency of 75 kHz and a force constant of 3 N/m. All experiments were carried out under ambient conditions. Asylum Research software was used to collect and analyse the data. Data was obtained as a function of scan window size, i.e. image dimension, for each kind of film. This was especially important to determine the surface roughness of the films, since roughness can depend on image size and may not be representative of the entire film.

Figure 2.2 ((a) to (f)) shows AFM images obtained for eumelanin thin films cast on glass slides. The corresponding figures for other substrates can be found in the Appendix (Figure S2.3, Figure S2.4 and Figure 2.5). It is worthy of note that only a minimal difference was detected between the surface roughness of the films on different substrates. Furthermore, glass slides proved to be the best substrate to fabricate devices on (see later, Chapter 4), hence the focus here on this particular substrate.

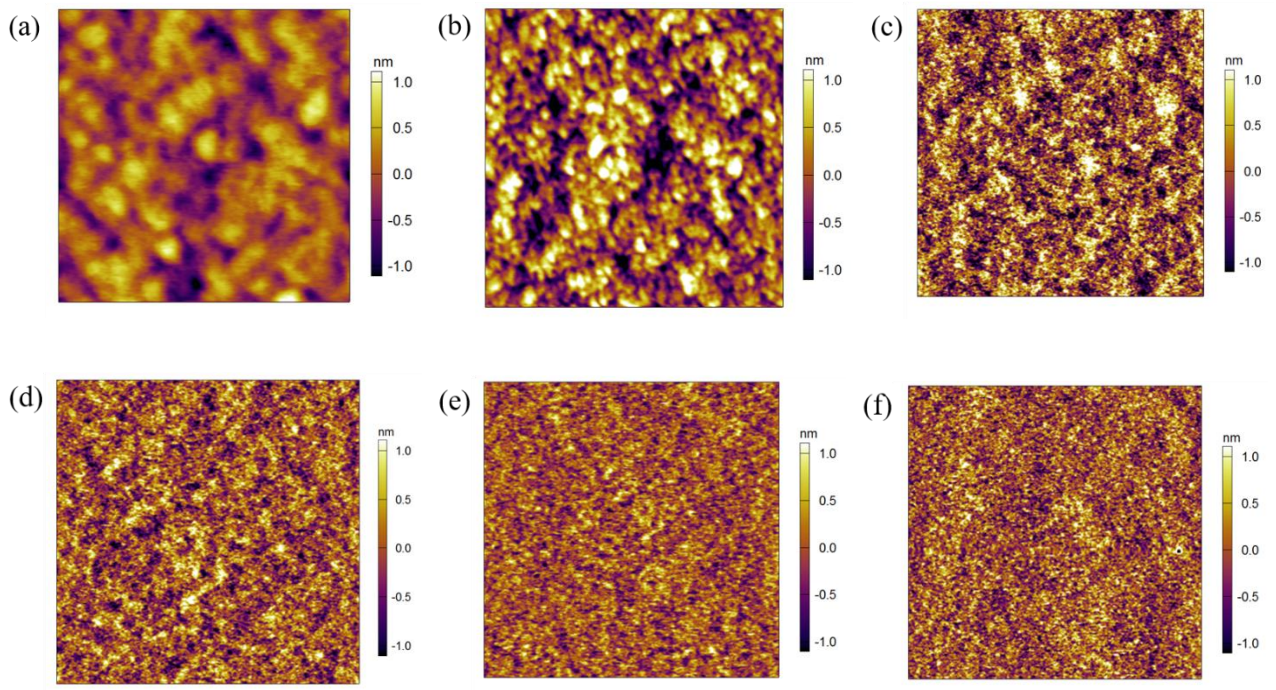

Figure 2.2. Topographic AFM images of a eumelanin thin film on a glass substrate taken at different image dimensions/magnifications: (a) 500x500 nm^2, (b) 1x1 μm^2, (c) 5x5 μm^2, (d) 10x10 μm^2, (e) 20x20 μm^2, (f) 30x30 μm^2.

As can be seen in Figure 2.2, as the image dimension increases, the film morphology does not appear to change. This indicates that the eumelanin film remains homogeneous across a sample. The films presented here did not show any significant features, such as cavities or peaks. However, some large round formations can be seen (e.g. Figure 2.2(b) and Appendix), which could indicate that eumelanin absorbed atmospheric water vapour [105], since eumelanin is hygroscopic and the measurements were done under ambient laboratory conditions.

At the highest magnification (Figure 2.2 (a)-(c)) the images indicate that the eumelanin film consists of densely packed granules 40-50 nm in diameter. The size of these granules is consistent with previously published literature on thin films cast from solution as well as scanning tunnelling microscopy [71] and would indicate that eumelanin "solutions" at high pH are not technically solutions but colloidal suspension of eumelanin particles as has also been inferred from optical spectroscopy [76].

The surface roughness profiles for films on all substrates were obtained at each magnification, from which, the root-mean-square roughness of the films were determined by averaging over three images of the same sample. The resultant data is depicted in Figure 2.3.

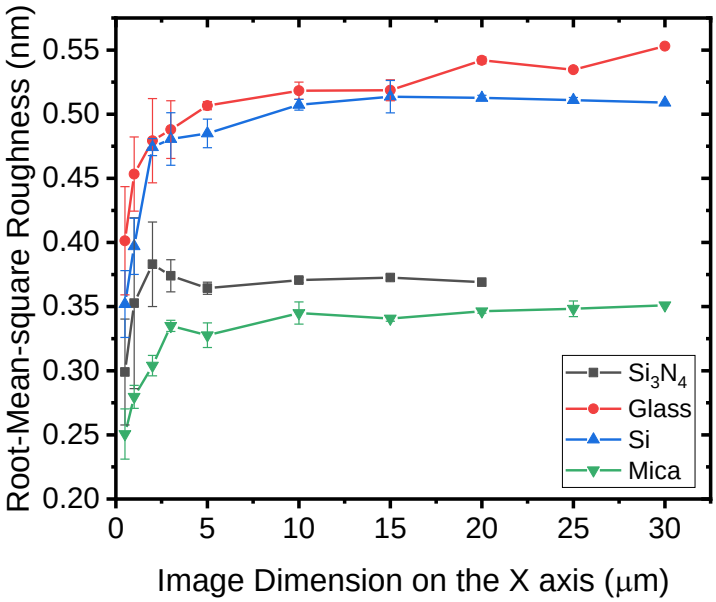

Figure 2.3. Root-mean-square roughness as a function of image size for 50 nm eumelanin thin films spin-coated on different substrates. As can be seen, the data indicates that the films do not exceed a roughness of greater than 1 nm, which make these eumelanin thin films excellent candidates for device applications. The error bars presented on the graph were calculated (2SE) across three different samples.

Figure 2.3 shows that regardless of the substrate, the eumelanin casting process forms smooth films. The roughness of the film cast on Mica and Si_3N_4 substrates remains between 0.25 and 0.35 nm throughout the whole spectra of image dimensions. It then increases slightly for the films cast on Si wafers and glass (up to 0.55 nm). This increase is insignificant and hence, any of the probed substrates could be used for the film casting. The smoothness of the film is relatively insensitive to image dimension. Over the entire image dimension spectrum, the roughness observed between all the substrates remained within a tight band between 0.22 – 0.6 nm, all below 1 nm. Usually it is a challenge to create homogeneous films of eumelanin due to its insolubility in standard solvents. Multiple examples of literature in the past few years report similar synthetic models of eumelanin which have been created in thin film form using variety of starting materials and processing techniques. Notable examples of these include: 1) Wünche *et al.* [106], showing eumelanin thin films fabricated using a spin coating method. Two batches of eumelanin, dissolved in different solvents (DMSO and ammonia) were spun cast from solution. The results show that the films spun cast from DMSO solution were reasonably smooth and homogeneous, whilst the films processed from ammonia solution, still contained aggregates. In this work film roughness of 1.6 nm was reported [106]; 2) Abbas *et al.*, used a spray deposition method and reported the film roughness of 0.4 nm, however the films presented in this work lacked the uniformity on a large scale [107]; 3) da Silva *et al.*, compared the morphology and properties of three ammonia solutions, which contained different

concentrations of eumelanin. While the surface roughness was approximately 0.5 nm for all three types of films, there were still peaks observed on the AFM profile [108].

For organic materials spun cast from a solution, the roughness is a crucial parameter when making devices, the smoother the film the more acceptable it is for making device quality films [70]. Hence, the procedure for the thin film fabrication described here is suitable for preparing device quality thin films. Furthermore, such smoothness is a critical requirement for other characterisation techniques such as Neutron Reflectometry.

In conclusion, the eumelanin thin films fabricated above are homogenous and smooth and good candidates for devices and for further characterisation.

2.4. X-ray Photoelectron Spectroscopy

Eumelanin is a chemically heterogeneous polymer that is polymerised based upon DHI and DHICA monomers and their various redox states (Chapter 1, section 1.3). Since the final polymer is not easily subject to standard chemical analysis [47] due to its insolubility and intrinsic heterogeneity, X-ray photoelectron spectroscopy (XPS) is used as an elemental analysis tool to determine the atomic ratios of the underlying constituents, Carbon (C), Nitrogen (N) and Oxygen (O) (see examples [109, 110]). The ratios obtained via XPS can then be used to determine whether the final polymer has ratios commensurate with the initial starting monomers of DHI and DHICA. As such, thin films of eumelanin were investigated using XPS. This was done for both the Neutron Reflectometry experiments (see below) and characterisation of films in general.

XPS measurements were performed using a Kratos Axis Ultra XPS Surface Analysis System with a monochromatic Al Ka X-ray source. Survey and high resolution scans (for the Neutron Reflectometry measurements specifically) were taken at 120 and 20 eV pass energies, respectively.

For the neutron reflectometry measurements, the spectra were referenced to a binding energy of the N 1s peak of poly(9-vinylcarbazole) at 400.22 eV [111]. The XPS spectra were analysed using CASA XPS software. Atomic ratios for C, N and O were determined from integrating areas under the C 1s, N 1s and O 1s peaks using Shirley backgrounds for the peak modelling. Example data set can be seen in Figure 2.4.

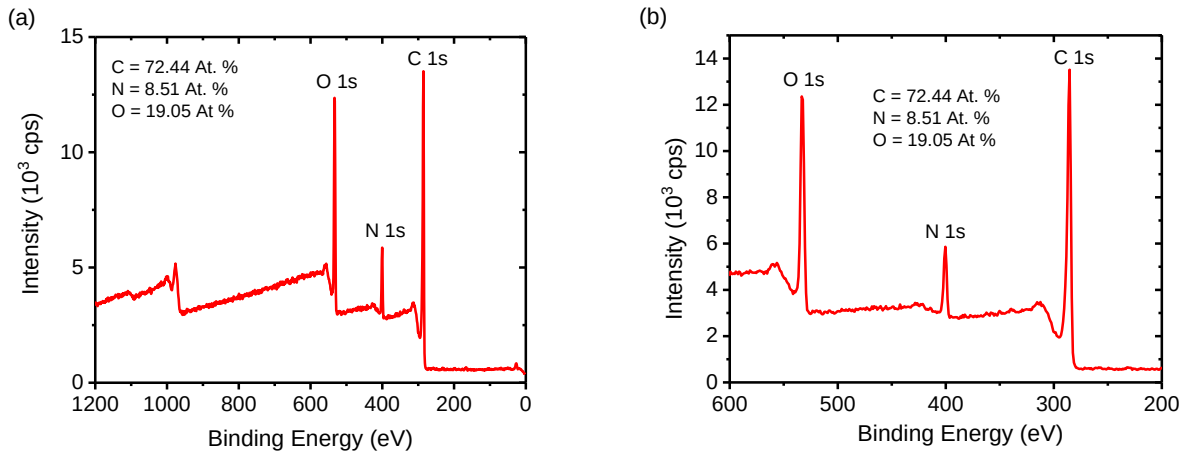

Figure 2.4. XPS scans obtained on eumelanin thin film on silicon substrates for comparison with Neutron Reflectometry experiments: (a) Scan from 1200 to 0 eV, (b) O, N, C region of the spectrum shown in (a). Atomic ratios indicated. XPS scans obtained on eumelanin films deposited on glass slides can be found in the Appendix, Figure S2.6.

To test whether the films fabricated were heterogeneous polymers based on DHI and DHICA, it is useful to determine the expected atomic ratios for the individual monomers and then compare the result to Figure 2.4. For DHI, the numbers of atomic constituents are 8 C, 2 O and 1 N. This yields an expected percentage break down of approximately 72% C, 18% O and 9% N with the remainder due to rounding errors. Hydrogen is omitted in these calculations since XPS is unable to observe signal related to H. For DHICA, the atomic constituents are 9 C, 4 O and 1 N yielding a percentage breakdown of approx. 64% C, 29% O and 7% N.

Comparing the XPS results (e.g. Figure 2.4) to those expected for the monomers, it can be clearly seen that the atomic percentages are very similar to that expected for DHI, with the exception of a slightly higher oxygen amount and lower nitrogen amount. This suggests that the eumelanin thin film is a polymer primarily composed of DHI, with only a small amount of DHICA, or more specific COOH, being present.

In conclusion, XPS was used to characterise the eumelanin thin films elementally. It was found that the ratios of C, N and O were commensurate with that of a heterogeneous polyindole quinone polymer such as eumelanin. However, the ratio values indicated that the thin films were primarily DHI, and that there was only a small amount of COOH present. Hence, alongside the UV-Vis spectra and knowing the origins of the synthesis, it can be confidently asserted that the eumelanin thin films fabrication method yielded a model eumelanin material. This is consistent with a large body of published literature.

2.5. Neutron Reflectometry

As was described in Chapter 1, eumelanin possesses a unique set of physico-chemical properties. The property of most interest to device design and fabrication is its hydration dependent hybrid protonic-electronic electrical conductivity. Given that hydration is the key variable to eumelanin's conductivity, it is incongruent that to date there has been no systematic morphological studies of eumelanin thin films and their interaction with water. This key question, the effect of water interaction on morphology, should be investigated to further understanding of conductive eumelanin thin films' potential device applications and to help with future interpretation of eumelanin based device performance. Gravimetric adsorption isotherms for eumelanin exposed to H_2O and D_2O vapour have been reported for pressed powder pellets of eumelanin [112, 113], but there are no such reports for eumelanin thin films. Furthermore, it would be useful to gain information on how the water is distributed throughout a film since this impacts performance parameters such as responsivity, speed, stability, and reproducibility.

One technique that can probe the effect of morphology of thin films as a function of solvent penetration (e.g. water) is Neutron Reflectometry (NR) [114-116]. It allows direct and non-invasive investigation of thin film structure and how it evolves as a function of water content. The NR method involves utilising a neutron source to direct a beam of neutrons onto a thin film target. Taking advantage of the wave nature of matter, the neutron matter waves interfere with the thin film under investigation depending on the atomic constituents of the films and their position in the film. After the interference event, the neutrons are detected as particles and an interference spectrum is constructed in which fringes can be observed. The technique is analogous to optical surface interference experiments in which the refractive index of different layers within a film determine the fringes. In the case of NR, instead of the refractive index, the scattering of the neutron off the atomic nuclei determine the interference structure.

As mentioned above, in an NR experiment, neutrons are directed onto a thin film sample and where each stratum reflects the waves to some degree leading to interference between the reflected matter waves. The quantification of the interference fringes is performed as a function of momentum transfer, $Q = \frac{4\pi \sin\theta}{\lambda}$, θ is the angle of incidence and λ is the neutron wavelength. The spacing between the fringes is directly related to the thickness of the layers within the thin film and the scattering length density governs the amplitude of the fringes.

The scattering length density, or SLD (ρ_i), is given by the following equation:

$$\rho_i = \frac{\rho_{M,i} N_{\mathrm{Av}}}{M_i} \sum_j n_j b_j \equiv \frac{1}{V_i} \sum_j n_j b_j \qquad \text{(Eq. 2.1)}$$

where $\rho_{M,i}$ is the mass density of the species i, N_{Av} is Avogadro's number, M_i is the atomic molar mass of the species i, V_i is the molecular volume of the species i, n_j is the number of atoms j in the molecular formula of species i, and b_j are the corresponding bound coherent neutron scattering lengths. Essentially the SLD is the product of the number density of molecules in a thin film and the bound coherent neutron scattering lengths of the constituent atoms in a molecule. Hence, as an example, when films are exposed to H_2O and D_2O vapour, difference or contrast in the neutron scattering lengths of hydrogen (b_H = - 3.74 fm) and deuterium (b_D = 6.67 fm) [117] nuclei result in the hydrated films scattering the neutron waves quite differently because the overall SLD of the film changes markedly. The sorption of water into eumelanin thin films and the corresponding structural changes can then be modelled as changes in film SLD as a function of distance from the substrate by a least squares analysis of the observed reflectivity profiles [118].

To perform NR experiments effectively, one needs smooth, thin films. The neutron matter waves are sensitive to roughness, since roughness leads to incoherent scattering and thus attenuates the fringes. As demonstrated above, eumelanin thin films can be fabricated with roughness of <1 nm, making them ideal for NR experiments. Eumelanin thin films were prepared as described above. The one key difference was in selection of substrate. Eumelanin thin films were deposited on 50 mm diameter silicon wafers with native oxide. These substrates were initially cleaned with Piranha solution [a mixture of sulphuric acid (98%, 245 ml) and hydrogen peroxide (30%, 105 ml)], followed by a UV-ozone (20min) treatment. Alongside NR experiments, an X-ray Reflectometry (XRR) experiment was performed, which determined the mass density and average empirical formula for a dry thin film [119]. For the XRR experiment, eumelanin films and substrates preparation was the same as for NR.

The NR measurements were performed using the PLATYPUS time-of-flight neutron reflectometer operating in medium resolution mode, ($\Delta Q/Q$ = 4.5%) at the OPAL 20 MW research reactor (Australian Nuclear Science and Technology Organisation (ANSTO), Sydney, Australia) [120]. The samples were placed on top of a boron carbide block in a sealed custom built chamber. The chamber was connected to a computer controlled ANSTO "static" vapour pressure system (Hiden Isochema, based on an original design of their XCS sample control system). The vapour pressure was controlled by two needle valves. One of the valves was connected to a turbo pump and the other to a heated liquid reservoir that contained either H_2O or D_2O. H_2O and D_2O were degassed before the experiment with four freeze–pump–thaw cycles to purge the liquids of any trapped gasses. The eumelanin films were initially placed under vacuum and their reflectivity profiles were recorded (Figure 2.5). Samples were then exposed to the desired pressure of H_2O or D_2O vapour and their reflectivity profiles were obtained. The chamber was then evacuated to purge the atmosphere to insure the reversibility of the sorption process before the next cycle. The pressure in the sample chamber

was observed to vary by around ±0.3 mbar during the ~ 4–6 h exposures to H_2O and D_2O and this error range was ascribed to all exposure pressures. Three measurements were taken at the same value of Q to ensure an equilibrium state. Then, the reflectivity profile was recorded across the entire Q-range [0.008, 0.235]/Å^{-1} (θ = 0.65° and 3.00°). Films were exposed to 0%, 7.5%, 20%, 50% and 80% of the saturation pressures of H_2O and D_2O, which were taken to be 31.0 mbar and 27.0 mbar, respectively [121]. The films were able to reach the equilibrium in 20–50 minutes after exposure or evacuation.

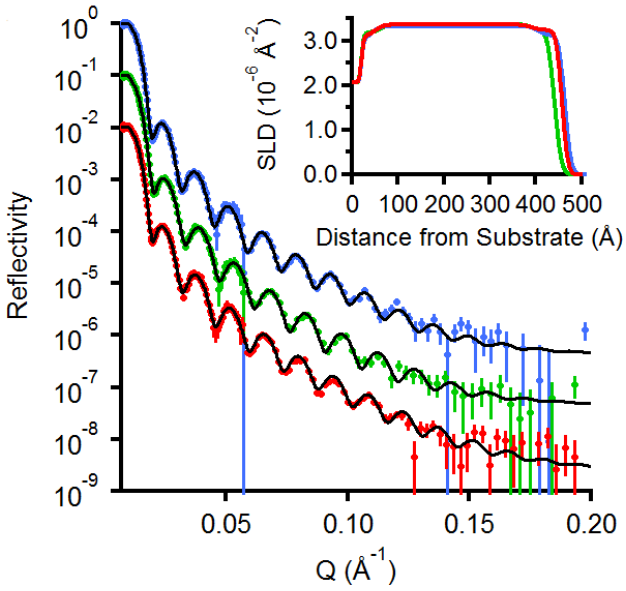

Figure 2.5. NR profiles of 3 different eumelanin thin films dried under vacuum. Each data set was recorded on a separate film produced in the same batch (different colours indicate different samples). Individual points indicate recorded data and the solid black lines represent the spectrum predicted by the fitting model (see text for details) and traces are offset for clarity. The inset show the corresponding 1D variation in the SLD with increasing distance of the films from the silicon substrates.

X-ray reflectometry (XRR) measurements were performed as a function of incident angle (θ) on a Panalytical XPert Pro reflectometer operating with Cu Kα (1.54 Å) radiation. X-rays from a (45 kV) tube source were focused with a Göbel mirror, collimated with a 1/32° pre-sample slit and detected with a Xe scintillator detector. A sample was placed inside a custom-built sample chamber under a vacuum (16 mbar) for the measurement. Data recorded can be seen in Figure 2.6.

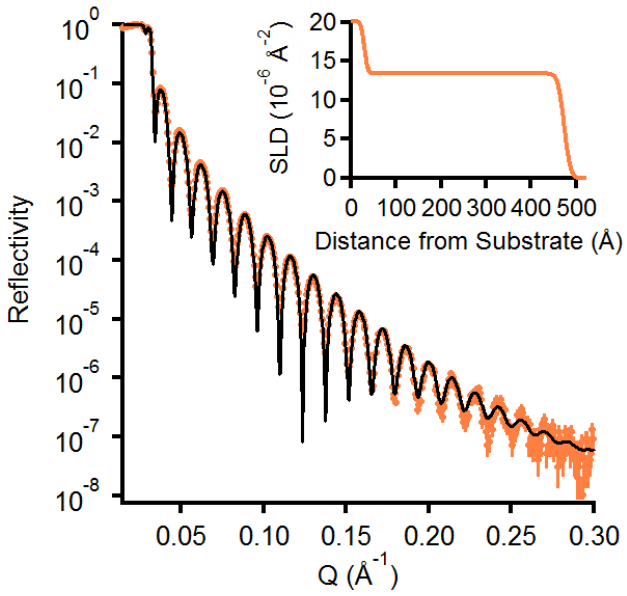

Figure 2.6. XRR profile of a eumelanin thin film dried under vacuum. Data was obtain from the same batch of synthesized eumelanin as in Figure 2.6. Individual points indicate recorded data and the solid black line represents the spectrum predicted by the fitting model (see text for details). The inset shows the corresponding 1D variation in the SLD with increasing distance of the film from the silicon substrate.

XPS measurements were performed as described in Section 2.4. The modelling of the NR reflectivity profiles and the XRR profiles was performed using the Motofit reflectometry analysis program [118, 122] and can be found in the Appendix (Table S2.1 and Table S2.2).

To establish the effect of water exposure on the eumelanin films, it was necessary to determine the mass density and average empirical formula of a dry eumelanin film under vacuum. This was achieved using a combination of three methods: NR, XRR and XPS, following procedures described previously (Figure 2.5 and 2.6). Three independent NR measurements on evacuated eumelanin films prepared under the same conditions revealed film thicknesses of 420–443 Å. This is in line with the measurements obtained for DEKTAK mentioned above. It demonstrates the consistency of the fabrication method.

The effect of increasing vapour pressures of H_2O or D_2O vapour are shown in the corresponding NR profiles given in Figure 2.7 A and C respectively. After each exposure to water vapour the sample chamber was evacuated and the reflectivity profiles of the films were re-measured. The corresponding NR profiles of the evacuated films after each exposure are shown in Figure 2.7 B and D for H_2O and D_2O, respectively. The reflectometry profiles obtained were modelled as three-layer films as described in the Appendix. The changes in the reflectivity profiles due to sorption and desorption of water were modelled with only four free structural parameters: the bulk layer thickness and the SLDs of the three layers in the model. A complete list of the fitting parameters used is given in Tables S2.1 and S2.2 in the Appendix.

Upon exposure to increasing vapour pressures of H_2O the eumelanin films were observed to swell (inset Fig. 2.7(A)) whilst the SLD of the film decreased, as was expected from the uptake of H_2O. For vapour pressures up to 6.2 mbar (20% relative humidity) of H_2O, the film was observed to contract close to its original thickness and SLD upon evacuation. The eumelanin film exposed to increasing vapour pressure of D_2O was observed to swell and contract in a similar manner to the film exposed to H_2O, with incomplete contraction observed after exposure to D_2O pressures of 13.6 mbar (50% relative humidity) and above. The SLD of the exposed film also increased significantly (Fig. 2.7(C)), as was expected from the uptake of D_2O into the film. The SLD of the evacuated film also rose after each successive exposure to D_2O (Fig. 2.7(D) inset), indicating that H/D-exchange was occurring with the eumelanin macromolecules in the film. It was assumed that any additional volume of the films after swelling and evacuation (determined from the film thickness) was occupied by traces of H_2O or D_2O trapped during contraction of the films with their usual neutron SLDs.

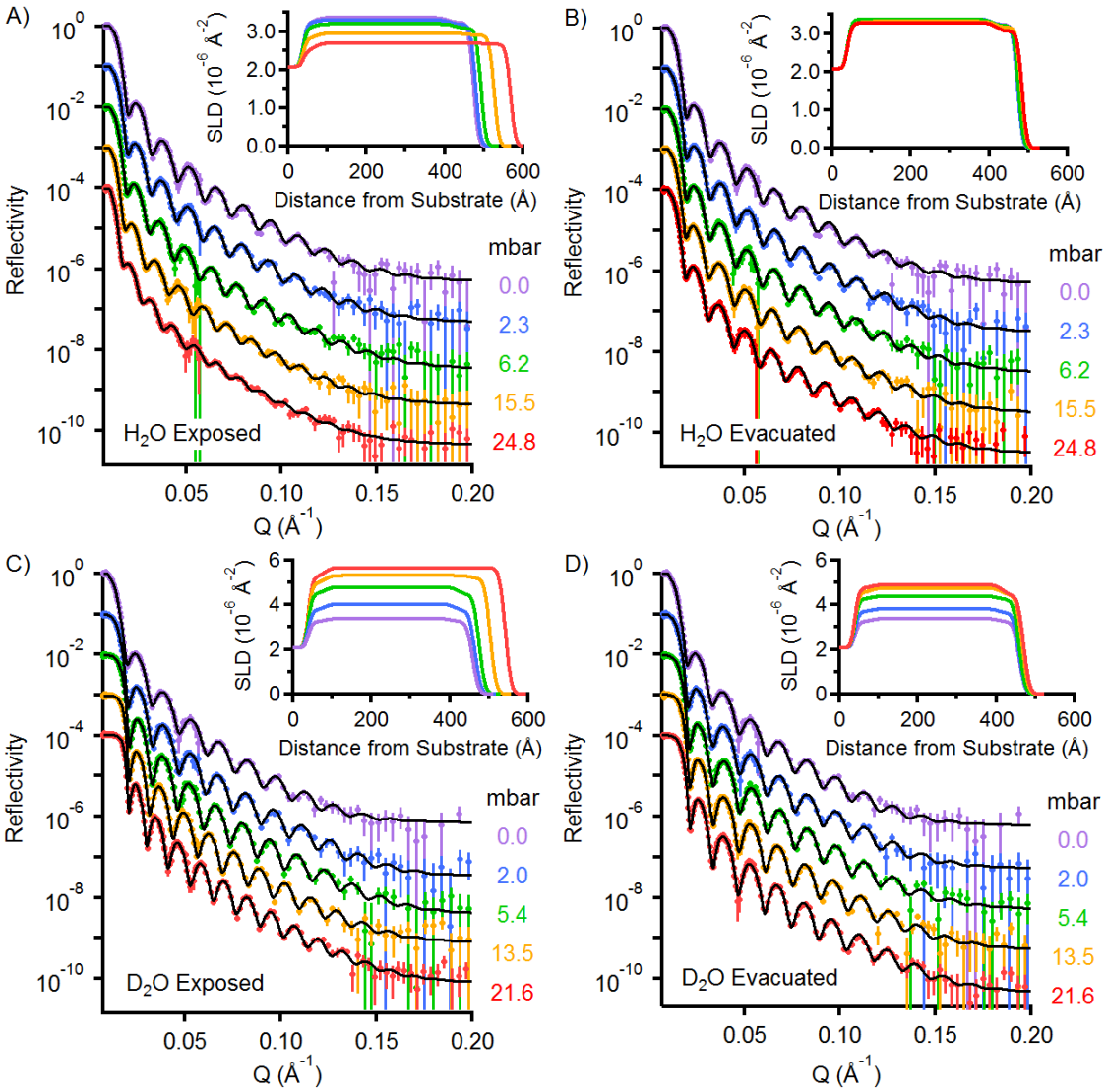

Figure 2.7. The NR reflectivity profiles for eumelanin films exposed to H_2O vapour (A & B) and D_2O vapour (C & D) with the data at each pressure (indicated) being offset for clarity. Fits for each profile are also present with the insets showing the modelled SLD profiles vs thickness of the eumelanin film. All of the data in (A) and (B) are from

measurements on the same film and all of the data in (C and D) were recorded on a separate film. In each panel the 0.0 mbar spectrum corresponds to the initial measurement of the eumelanin film under vacuum. A and C show the data for films exposed to H_2O and D_2O, respectively. B and D show the data for films after the chamber was evacuated following each successive exposure to remove the respective vapours.

The formation of a water layer on top of the films can be excluded for the following two reasons. Firstly, if the water film was uniform, then an additional feature would have been observed in the melanin SLD curves (Figure 2.7) at the edge of the sample. Essentially, an additional layer would have been seen which would have had a lower SLD (high SLD in case of D2O) than the corresponding hydrated eumelanin film SLD. Secondly, if the water was forming droplets on the surface, the neutron scattering of them would have smeared out any signal coming from eumelanin and the interference pattern would have disappeared. However, this did not happen (Figure 2.7). Therefore, it is clear that no water was formed on top of the film.

When comparing the influence of D_2O vapour vs H_2O vapour on eumelanin thin films (Figure 2.7) the same conclusions can be drawn about the film behaviour with one major exception, that the SLDs after exposure to D_2O increases. The reason for this increase is that the SLD for deuterium, D, is positive. This fact clearly demonstrates that the eumelanin film is absorbing the water vapour. However, it can be also seen in Figure 2.7 D that after every evacuation the SLD systematically increases. Correspondingly, the SLD in the subsequent exposed films in Figure 2.7 B also increases. This observation demonstrates that H/D exchange is occurring. Essentially, due to the mass difference of the H and D atoms, the D's are replacing the H's in the polymer. Susceptible sites within the eumelanin film for exchange are presumably the COOH, OH and NH groups, since these sites have appropriate pK_A's.

The main conclusions that can be drawn from the described experiments are:

a) Decrease in SLD means that water has been absorbed into the film. The reason for that is that additional H from the H_2O molecules contributes a negative scattering length density, which decreases the SLD.
b) As eumelanin absorbs water from the environment, it swells, indicating that water is disrupting the eumelanin polymer morphology, and that water is not entering only voids in the polymer film.
c) The water is absorbed throughout the film evenly, since the SLD profile changes uniformly.
d) The surface roughness of the film, as indicated by the slope at the film edge of the film, stays consistent with addition of water. Hence the film, even though it absorbs water, is structurally robust.

These important observations form the basis for understanding the structural impact of water on eumelanin thin films.

2.6. Hydration Dependent Conductivity

The application of the concepts of solid state physics to biological molecules started in 1941 with a work of Szent-Györgyi [123], who proposed the existence of conduction bands in proteins. Since then much work has been done on the conductive properties of organic materials, eumelanin being one of them. For example, after investigating hydration dependent conductivity of various biomolecules, Rosenberg *et al.* [80, 124] developed a model utilising semiconductor models to explain observations (Chapter 1). The conductivity of an intrinsic semiconductor is due to the promotion of an electron from the valence band to the conduction band. In this case the density of charge carriers (and so as the conductivity) is temperature dependent. Essentially, water is a dielectric constant modifier, which when present, lowers the effective energy gap. This in turn promotes more charge carriers to the conduction band. This is the first model that takes into account hydration dependent conductivity of eumelanin [80].

Later McGinness *et al.* [79] used the model developed by Rosenberg to explain threshold switching behaviour discovered in eumelanin pellets. In this work a reversible threshold switch observed in the pressed powder eumelanin pellets is reported. Upon application of a potential a switch between a high and a low resistive states of eumelanin was shown. However, it is worthy of note that the dry samples of eumelanin pellets did not show any switching until they were hydrated. To explain this behaviour, McGinness *et al.* utilised Rosenberg's model, where a local modification of the dielectric constant of the material leads to lowering of the activation energy for conduction. It was concluded that the reversible switching observed in the pellets was an electronic effect related to amorphous semiconductor switching.

However, the above models have been questioned. The work of Mostert et al. [66] indicated that eumelanin, instead of being an amorphous semiconductor, is likely to be an electronic-ionic hybrid conductor. Electrical conductivity, muon spin relaxation, and electron paramagnetic resonance measurements were undertaken as a function of water content. It was shown that upon the absorption of water, extrinsic free radicals (electrons) and hydronium ions (protons) are produced, as given by the comproportionation reaction:

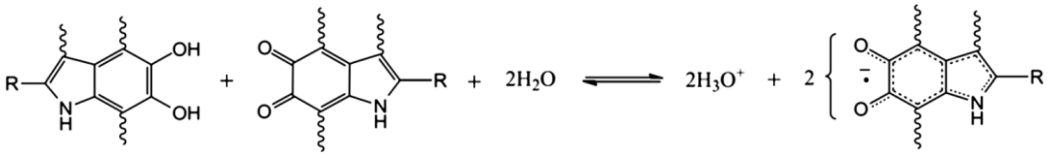

Mostert *et al.* propose that this chemical self-doping leads to hybrid ionic-electronic behaviour and explains the exotic electrical properties of eumelanin. Basically, the conductivity of eumelanin is regulated by the charge density of protons (hydronium) and semiquinone free radicals via the surrounding water content.

There are two basic mechanisms that play a role in bulk movement of an ionic charge carrier in a biomolecular conducting. The first is a centre of mass diffusion, or "vehicle mechanism" [125] and the second one is proton tunnelling or hopping [125] also known as the Grötthuss Mechanism. In the Grötthuss mechanism the orientation and polarization of the water molecules is a key to a faster transport than a centre of mass diffusion (Figure 2.8).

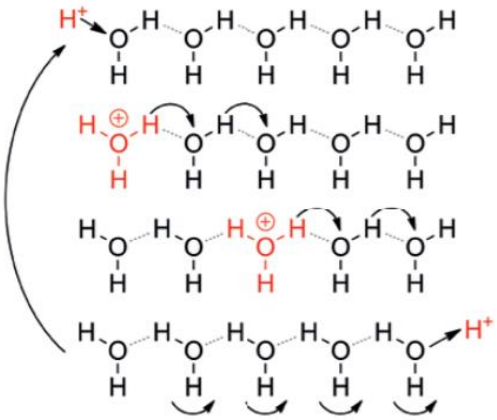

Figure 2.8. The Grötthuss mechanism shows how an ionic charge hops through a hydrogen-bonded network [13].

The Gröthuss mechanism is incoherent hopping. Since it involves a positive charge in coherent hopping of a massive particle, it can sometimes be difficult to distinguish it from *p*-type small polaron behaviour. This may be one of the reasons eumelanin was considered a semiconductor. It needs to be noted that solid-state current-voltage measurements of ion transporting materials, particularly utilising DC, are more difficult than for the electronic counterparts. The main reason for the difficulty is that most electrodes are found to be blocking with respect to protons or ions. The term "blocking" electrode can be explained in relation to the ohmic or Schottky concept in electronics. At small-to-moderate fields, injection and extraction can keep pace and the system can appear to be "ohmic" (linear current-voltage behaviour). However, at high fields blocking contacts lead to build up of space charge and strong capacitive effects. One of the ways to avoid blocking contacts is using palladium instead of gold. It was shown by Morgan *at al.* [126] that palladium forms proton conducting PdH_x upon exposure to hydrogen. PdH_x and Pd electrodes act as efficient source and sink for protons, making the conductivity measurements more precise.

Due to the difficulties associated with DC measurements, AC impedance methods are commonly used to extract charge transport behaviour information (also known as electrochemical impedance measurements, which will be discussed in detail in Chapter 3).

Nevertheless, performing DC measurements on a conducting material is an important characterisation step. DC measurements capture all movable charges in a material and give important insights into how AC measurements should be interpreted, since AC measurements tend to be model dependent. In this section DC conductivity experiments are reported on thin films that were fabricated

on glass as described earlier. However, in order to make electrical contact with the films, the glass slides were first subject to metal evaporation [100]. A glass sample was pre-cleaned as described above. Then 3 nm (as measured via an internal Quartz Crystal Microbalance in the evaporator) of chromium was evaporated thermally unto the glass, through a mask, to "wet" the glass and ensure that the actual contacting metal did not peel off the glass. The actual contact metal, gold, was then evaporated on top to a thickness of 50 nm. The electrical contact geometry was a 2 point, interdigitated set of source-drain electrodes. The interdigitated pattern was used to increase the active contact area of the electrodes to the film to reduce resistances measured and thus improve the electrical signal to noise ratio. The length and width of the channel were 100 μm and 11.2 mm respectively. The schematic for the electrodes can be seen in the Appendix, Figure S2.1. The eumelanin thin film was then spin-coated on top as described above and, hence the source-drain electrodes were in a bottom contact geometry.

With samples fabricated, the samples were then placed within a vacuum-capable chamber [81] (Appendix, Figure S2.7), specifically capable of maintaining a water vapour atmosphere. The chamber, made out of aluminium and acting as a Faraday cage, had a back plate lid with a vacuum capable high impedance electrical plug, which connected to an external electrical box. To this electrical box, numerous coaxial sockets were attached that ensured a shielded cabling connection. Inside the chamber there was an internal Teflon coated wiring to connect to samples. The connections to the samples were completed by creating copper wires for the thin film devices and connecting them to the devices via a one-pot conductive silver epoxy paint (RS components).

The vacuum system, as mentioned previously, was capable of hydration control. The chamber itself was connected to a rotary vacuum pump to enable vacuum pumping. However, the pump could be isolated to ensure a static vacuum system, a requirement for enabling a water vapour atmosphere. In addition to the pump system, a vial of deionized water was attached, which acted as the source of water vapour. The pressure of the water vapour was measured using a BOC-Edwards GK series gauge, 0-50mbar. Reading off the pressure gauge, and manually controlling the water vial valve, it was possible to select any desired pressure up to the saturation pressure of the water. The water was freeze-thaw-pumped 3 times to purge it of any trapped gasses and ensure no systematic error was introduced into the pressure readings. This was confirmed by measuring the saturation pressure of the water, which came to 24 mbar and was commensurate with the set temperature for the laboratory, which was 20°C.

The current-voltage (IV) data required for determining the conductivity was obtained by using an Agilent Semiconductor Device Analyzer B1500A. The voltage was swept forwards and backwards from -1 to 1 V, with a hold time of 60 s and a scan rate of 1 point per second. The voltage range was selected to prevent the electrochemical splitting of water into hydrogen and oxygen, which occurs at

a potential difference of 1.2 V [127, 128]. This reduced an additional systematic uncertainty in current measured.

The experimental procedure started with an initial pumping down of the chamber to vacuum for 2 hours. Pressures obtained were ~10^{-2} Torr (as measured by an additional Pirani Gauge, Gran-Philips). After isolating the pump from the vacuum chamber, water vapour was let in to reach the desired vapour pressure. Each pressure was held for an hour to insure equilibrium was reached. As mentioned in Section 2.4 regarding the Neutron Reflectometry experiment, one hour was a sufficient period of time to reach equilibrium. All pressure data was then normalised to a relative pressure value, using a saturation pressure of water 24 mbar, since experiments were carried out in ambient conditions (20° C). Once the IV data was obtained at a given pressure, additional water vapour was added to the chamber and the IV experiment was completed. Pressures selected for the experiment were 0 mbar, 5 mbar, 10 mbar, 15 mbar and 20 mbar. This ensured that there were enough data points to clearly observe a hydration dependent trend.

Presented in Figure 2.9 is an example set of IV data for a thin eumelanin film as a function of water vapour pressure. Multiple sets of data were obtained on different samples to check for consistent behaviour and can be found in Figure S2.8, in the Appendix. It is clear from Figure 2.9 that the current increases as a function of hydration. This is presumably due the increase of charge carriers, protonic and electronic, due to the shifting of the comproportionation reaction in eumelanin [66, 113]. The current increase is about three orders of magnitude, again commensurate with a shifting of the comproportionation reaction and observed elsewhere [66, 81, 84, 106, 107, 113] for eumelanin powders and thin films.

Interestingly, as can be seen, the IV curves do not go through the origin, as would be expected for a standard resistor type element obeying Ohm's law. Furthermore, there is hysteresis between the forward and backward sweeps. These observations are a clear indication of capacitive effects. This is not surprising given that eumelanin conducts protons, species that tend to exhibit capacitive behaviour due to their slow motion and inability to be extracted at electrical electrodes such as gold, i.e. blocking electrodes.

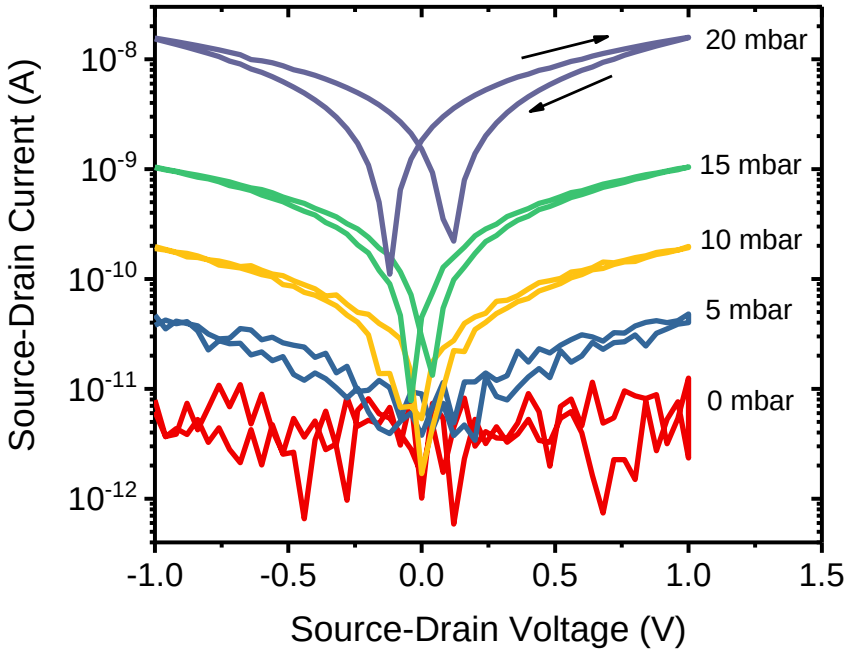

Figure 2.9. Source-drain current as a function of voltage for an example eumelanin thin film. Each IV measurement was taken at different water vapour pressures, which are indicated. Each curve is an average of three measured substrates (see Appendix, Figure S2.8 for the full data set).

The IV data obtained can be normalised to a conductivity plot, as a function of hydration and can be seen in Figure 2.10. It should be noted that the thickness used was 70 nm, which was measured by a Dektak XT (see above). This conductivity isotherm plot is the first conductivity isotherm for a eumelanin thin film that spans the entire relative pressure range for water. Other data sets described in literature only start at about 50% relative humidity [84, 107], and hence the data presented here gives a more complete overview of the electrical behaviour of eumelanin thin films. For the given range of 50% to 90% relative humidity the conductivity behaviour presented in the literature and investigated here is very similar. The conductivity of the semi-dry eumelanin films (at about 50% relative humidity) is ~10^{-7} S/cm and grows exponentially with the increase of hydration.

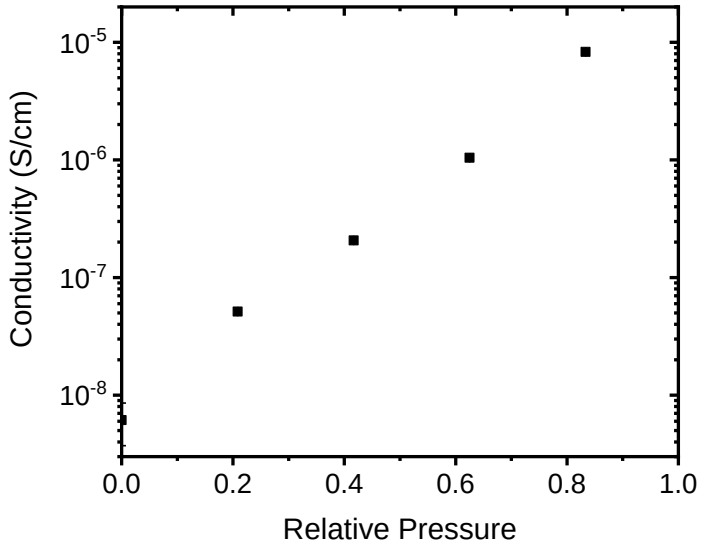

Figure 2.10. Eumelanin conductivity as a function of hydration. The uncertainty has been calculated (to 2 times the standard error) and is present on the graph, however the bars are smaller than the actual data point resolution.

In Figure 2.10 the data has been properly normalised using recently published findings on Neutron Reflectometry of hydrated eumelanin thin films [129], described in Section 2.5. To do so, the thickness of the samples had to be known and the change with hydration had to be anticipated. As such the thickness was measured at ambient using a Dektak XT profilometer, with films thicknesses of ~70 nm. The thickness changes determined by Neutron Reflectometry were then taken into account when calculating the conductivity for each level of hydration.

In comparison to the literature, the conductivity increases exponentially with increase of the water content. It is more or less similar to eumelanin thin films prepared in DMSO described in the literature [8]. For example, at given relative humidity of 80% the eumelanin conductivity in both cases is close to 10^{-5} S/cm. The dramatic increase in conductivity shows that the ionic component of eumelanin plays a significant role in charge transport. It is worthy of note that the DC measures the overall charge, however it is unable to distinguish between electronic and ionic contributions. Therefore, the DC measurements have limitations which cannot provide a complete insight to the charge transport in eumelanin. For this purpose AC measurements need to be implemented, which should be able to decouple ionic and electronic signals.

2.7. Conclusions

Eumelanin thin films were fabricated and characterised using a newly developed procedure. AFM and XPS studies were undertaken to ensure that the synthesised material was in fact eumelanin. Moreover, smooth and homogeneous films were obtained. The ratio of atoms measured by XPS showed that the synthesised eumelanin mostly contained DHI compounds. UV-Vis absorption

measurements showed that eumelanin possesses the same optical properties as standard eumelanin: broad-band monotonic featureless absorption. Because eumelanin's conductivity is dependent on its hydration state, it is important to understand its relationship with water at the surface level as well as in the bulk of the material. NR measurements showed that eumelanin swells upon water absorption and that water is evenly distributed through the film. Further conductivity measurements on eumelanin thin films proved that indeed its electrical conductivity is hydration dependent and increases exponentially as a function of hydration. It should also be noted that DC IV measures capacitive displacement current and extraction current of small population of electrons. The above findings are an important experimental step and the results form a foundation for design and realisation of eumelanin-based bioelectronic devices.

3. AC and Dielectric Properties

3.1. Introduction

The question of whether eumelanin's charge transport is dominated by ionic or electronic carriers, has been an ongoing question for a number of decades. This last property has been attributed recently, as indicated in Chapter 1, to a redox reaction, the comproportionation equilibrium (Figure 3.1) in which the long-range conductivity is presumably due to protons (associated with hydronium – H_3O^+) and negatively charged semiquinone (SQ) free radicals [66, 113].

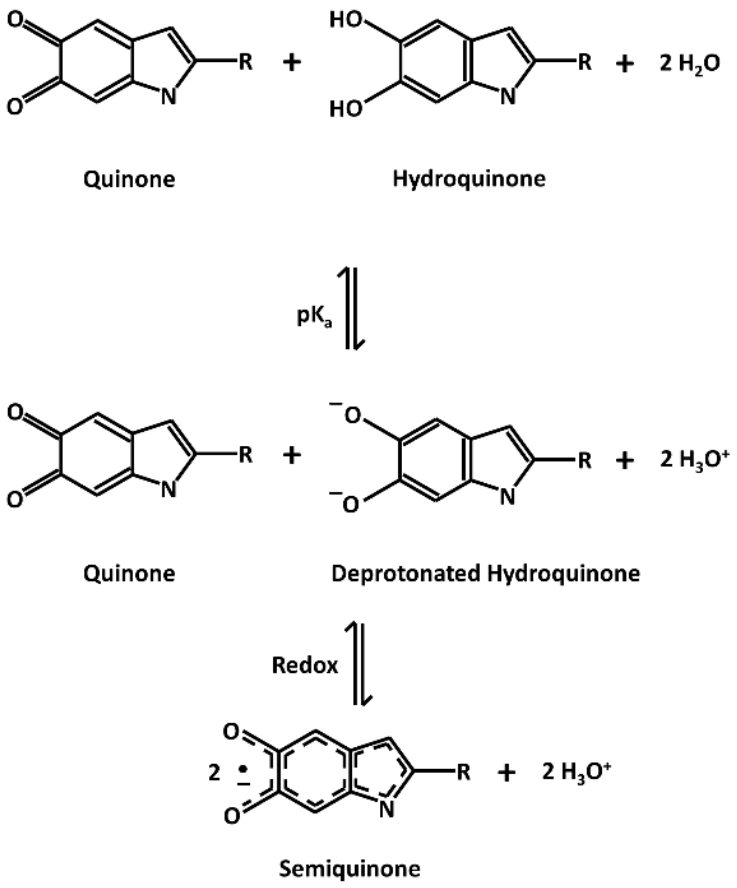

Figure 3.1. The comproportionation reaction, split into two sequential steps. In the first step, the Hydroquinone becomes deprotonated, driven by the local environment and the pK_a of the moiety. Once deprotonated, a 1 electron redox reaction occurs between the two different oxidative states of the moieties to form the intermediate, negatively charged semiquinone.

As indicated in Chapter 2, the proton concentration and SQ charge density can be modulated by changing the state of hydration, with the water environment also acting as the proton transporting medium via the Grötthus Mechanism [66, 81, 84, 106, 113, 130]. The reaction in Figure 3.1 is a

simple manifestation of Le Chatelier's principle in which the addition of water forces the formation of hydronium and SQ. This process leads to orders of magnitude change in the conductivity of eumelanin as a function of water content [66, 81, 113, 131] (Chapter 2).

A natural question to ask is which of the two potential charge carriers (proton or free radical), dominates the current, or are they both significant contributors? Recent work appears to indicate that the protonic current is the dominant component [84], but there are also multiple reports invoking a substantial electronic effect [132-134]. These questions are important in determining what sort of material and device applications eumelanin can be applied to. This is especially pertinent to the question of whether eumelanin thin films can be employed as a proton top gate in an OECT, and whether one should account for potential electronic injection from eumelanin into a conductive channel.

Currently, there is only one study from the 1970's that attempted to quantify the relative contributions of protonic and electronic current using a coulombmetric approach [130]. This study indicated a relative contribution of 65% protonic current and 35% electronic current – however, the coulombmetric method only captures electrode-sample-surface electrochemical effects and would thus naturally report both current types. With the recent advances in eumelanin thin film fabrication (Chapter 2) and general experimental techniques with hydration dependent control, one can now potentially probe bulk effects of eumelanin in the solid-state and thus address the question of the relative charge carrier density in a more reliable and systematic manner. To this end, described in this chapter is an alternating current (AC)/impedance experiment on the thin films fabricated according to the techniques described in Chapter 2. Given that the relative transport physics of the two charge carriers is dominated by the large mass discrepancy between the proton and electron, this could potentially deliver radically different frequency dependent signatures which could be isolated. Furthermore, in the experiment described below, D_2O vapour was also used alongside H_2O to probe the kinetic isotope effect, as was recently reported on cephalopod proteins [83]. The kinetic isotope effect, specifically, the replacement of H with D, may change the mobility of the mobile protonic charge carrier, since D is twice as heavy as H. Such a change may manifest itself in a change of frequency dependent behaviour and help distiguish between electronic and protonic charge carriers.

3.2. Experimental methodology

3.2.1. Impedance spectroscopy background

Electrical Impedance Spectroscopy (EIS) is a powerful technique for characterising electrical properties of materials. This method has been widely used in electrochemistry [135, 136], biomedical applications [137, 138], material science [139], and other applications. The advantage of this

technique is its versatility. EIS can be used to investigate the dynamic properties of bound or mobile charge carriers of materials (in their bulk or interfaces with other systems), e.g. solid-liquid interfaces. The general approach to EIS is to apply an oscillating electrical stimulus (voltage or current) to the electrodes and observe the response (resulting current or voltage). It is assumed that the properties of the electrode-material system are time-invariant and it is one of the basic purposes of EIS to determine these properties and their dependence on temperature, pressure, humidity, and applied bias [140].

Impedance itself consists of a measurement of the AC electrical current, $I_t(\omega)$, at a certain angular frequency, ω, when an AC voltage, $V_t(\omega)$, is applied to the system – or vice versa, a measurement of $V_t(\omega)$ at an applied $I_t(\omega)$. The definition of impedance, analogous to the DC resistance equation, is then given by:

$$Z(\omega) = \frac{V_t(\omega)}{I_t(\omega)} \quad \text{(Eq. 3.1)}$$

Usually impedance is measured by maintaining a constant current or voltage amplitude and scanning the frequency at a range of values $f = \omega/2\pi$ from Hz (or mHz) to 10MHz. It is very important to determine the EIS parameters (such as resistances, capacitances, etc.) under different conditions at steady state to be able to relate the obtained data to a particular physical model [141].

Impedance (Z) is defined in a similar manner as Ohm's law is for DC currents. The impedance can be rewritten mathematically in Cartesian form, using complex notation:

$$Z = R + jX \quad \text{(Eq. 3.2)}$$

where R is the real part which represents the resistive component, and X is the imaginary part which represents the reactance. Using polar form gives an opportunity to express magnitude (the ratio of the voltage amplitude to the current amplitude) and phase (the phase shift by which the current lags the voltage) characteristics of impedance:

$$Z = |Z|e^{jarg(Z)} \quad \text{(Eq. 3.3)}$$

where |Z| is the magnitude, which represents the ratio of the voltage amplitude to the current amplitude, *arg*(Z) (or θ) represents the phase difference between voltage and current. The polar form of impedance is used for simplicity in calculations.

For all systems of physical interest there are two basic circuit elements which always appear. These are the high frequency limiting geometric capacitance, C, and the high frequency limiting resistance of the system, R, the bulk or solution resistance. They are important quantities and are part of the bulk response of the system as opposed to its interfacial properties [142].

The impedance of an ideal resistor is purely real, because the voltage and current waveforms are proportional and in phase:

$$Z_R = R \quad \text{(Eq. 3.4)}$$

The impedance of ideal inductors and capacitors have a purely imaginary form. For example, for a capacitor:

$$Z_C = \frac{1}{j\omega C} \quad \text{(Eq. 3.5)}$$

where C is capacitance. In this case the resulting current is also sinusoidal, but it is 90 degrees out of phase with the voltage.

The simplest electric circuit comprises a resistor and a capacitor in series (an RC, or resistor-capacitor circuit). The total impedance of such circuit can be expressed as:

$$Z = R + \frac{1}{j\omega C} \quad \text{(Eq. 3.6)}$$

where $\omega = 2\pi f$. From here:

$$Z = \sqrt{R^2 + \left(\frac{1}{j\omega C}\right)^2} \quad \text{(Eq. 3.7)}$$

Moving now to a realistic electrochemical system, for example, a liquid, containing ions/electrolytes, the rate of an electrochemical reaction is often influenced by diffusion of molecules towards, or away from the electrode-electrolyte interface. In this case a Warburg element is introduced. Mathematically the Warburg impedance is expressed by:

$$Z_W = \frac{\sigma_w}{\sqrt{j\omega}} \quad \text{(Eq. 3.8)}$$

where σ_ω is the Warburg diffusion coefficient. The Warburg element is represented in a Nyquist plot by a straight line with a slope of 45° at lower frequencies, since the diffusion of molecules is a slow process.

In traditional electrochemical literature two situations are defined: 1) a supported system, which has a supporting, or indifferent, electrolyte that decouples the charged ionic species of interest from the rest of the charges in the system, which makes its electrical effects easier to calculate in an approximate but adequately accurate way; 2) an unsupported situations, in which there is no additional amplification of the signal in question. In unsupported systems it is generally much more difficult to solve electrical response problems, particularly under large signal (non-linear) conditions [142]. Solid electrolytes and polymers belong to unsupported systems, even if sometimes they can possess some electrical characteristics usually associated with supported systems. It is crucial to distinguish between supported and unsupported systems for interpretation of IS results. It should be emphasised that developed system described in this thesis is unsupported, which makes the definition of an equivalent circuit more challenging.

In general for the electrochemical analysis of the AC data the Nyquist and Bode plots are useful for representation of the AC parameters. These plots are used to evaluate the key parameters of the system, such as resistances, impedances and frequency dependent responses and obtaining the best fitting parameters for equivalent circuit modelling. These constructs will be used in this Chapter.

Nyquist plot represents $Z'(\omega)$ and $Z''(\omega)$ in a complex plane. The advantage of a Nyquist plot is the possibility to reveal such electrochemical parameters as solution resistance (R_s), electrode polarization resistance (R_p) or contact resistance (R_c), double layer capacitance (C_{dl}), etc. and enable the clear demonstration of a low frequency diffusion tail as proof of ionic conduction. However, one disadvantage of Nyquist plot is that it does not present any information on a frequency axis. Hence, to fully understand the data, Nyquist plots were interpreted alongside the dielectric spectra.

An example of a simple Nyquist plot is shown on Figure 3.2. The equivalent circuit for such a system would contain a minimum of four parameters: a resistor, connected in parallel with a capacitor and another resistor in series with a Warburg element. The semicircle on the Nyquist plot is a feature that appears due to the resistor and a capacitor in the equivalent circuit. The solution resistance can be calculated by the high-frequency intercept on the real axis. The diameter of the semicircle is equal to the polarization resistance. The tail represents diffusion and is related to the Warburg element [143].

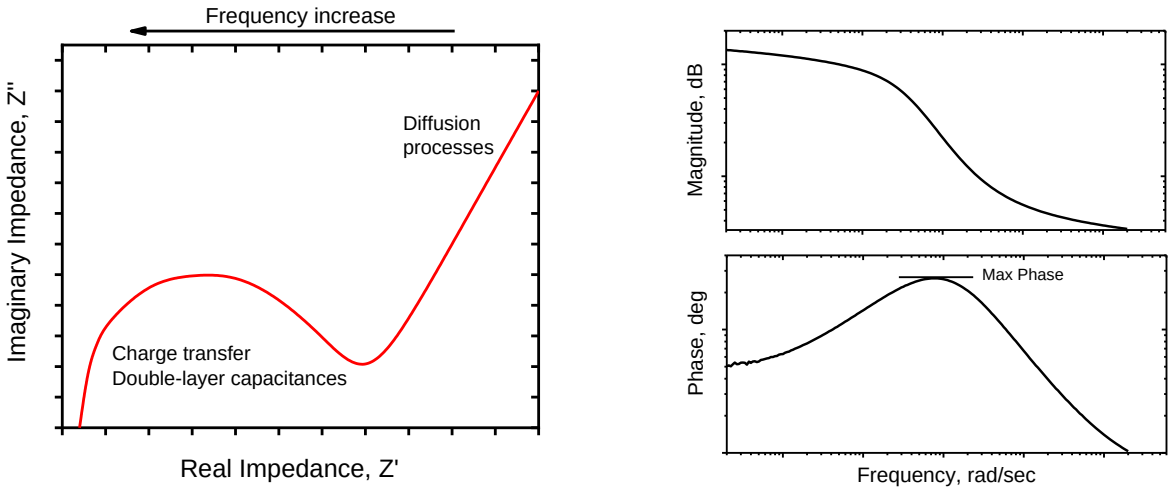

Figure 3.2. An example of a typical Nyquist plot (a) that consists of a semicircle representing a charge transfer and a linear tail representing a diffusion process and an example of a typical Bode plot (b).

Bode plots show impedance $Z(\omega)$ and phase angle $\theta(\omega)$ as a function of frequency (Figure 3.2 (b)). Both Bode and Nyquist plots are utilised to derive system-specific parameters.

There are many parallels between wet and all-solid electrochemical systems. However, one important distinction is that while liquid electrolytes have negligible electronic conductivity, most of solid electrolytes can exhibit substantial electronic conductivity. In solid systems mobile ions are

considered to be able to move as close to an electrode as permitted by the ion's size. However, in liquid electrolytes there is an inner layer composed of solvent molecules usually present adjacent to the electrode. This layer may often be completely devoid of ions. Therefore, capacitive effects at the electrode interface regions can be considerably different between liquid and solid electrolyte systems [144].

3.2.2. Device fabrication

Eumelanin used in this experiment was synthesized as described in section 2.1.

Glass slides (15 mm x 15 mm) with 80 nm thick patterned ITO (Xin Yan Technology) were cleaned with Alcanox, rinsed in water and ultra-sonicated in acetone (5 min). Afterwards they were rinsed with deionized water, ultra-sonicated in 2-propanol (5 min) and dried under a flow of nitrogen. The substrates were finally treated with UV-Ozone (20 min). A thin film of eumelanin was spun cast at 500 rpm for 5 sec followed by 1500 rpm for 60 s. The obtained thickness of 70 nm was measured using a Dektak XT. Finally, 30 nm Ag top electrodes were thermally evaporated on top. A schematic picture of a sample presented in the Appendix, Figure S2.1.

3.2.3. Electrical measurements

Humidity dependent measurements were carried out using a vacuum capable chamber and an Agilent E4980A LCR meter. The chamber was initially designed for the Charge Carrier Extraction by Linearly Increasing Voltage (CELIV) measurements and consisted of two steel plates connected together by screws with a glass window in the middle. The sample holder had four gold spring pins as contacts, wired through to the coaxial outputs. The measurements were taken sweeping through a frequency range from 20Hz to 1MHz. For the hydration procedure, the chamber was initially pumped down to vacuum for 2 hours using a rotary pump. The desired water pressure was then achieved, using the same methods as described in Chapter 2, Section 2.6. The same procedure was used for D_2O vapour. Each vapour pressure was held for an hour to insure equilibrium was reached as indicated by the neutron work in Chapter 2, Section 2.5 (see also [129]). All pressure data were then normalised to a relative pressure value, using a saturation pressure of 24 mbar for H_2O and 20 mbar for D_2O.

To have confidence in the measurements, two potential systematic errors had to be accounted for: a) that the eumelanin thin films be at equilibrium with the hydrating environment; 2) that the measurements were not dominated by capacitances from the electrical measurement circuit. The latter issue occurs when a planar geometry is utilised in AC measurements (as used elsewhere [84]) on thin films. Essentially, the electrode surface area is minimal and thus the capacitance of the sample is less than that of the electrical wiring. To overcome these potential errors, and to cross check the data

obtained in the experiment described above, a parallel, liquid contact setup was designed and used. In this experiment, the same kind of sample as used above was fabricated, with the exception that the Ag top contact was omitted. Instead, the sample was placed on a custom made stepper motor, within the previously described hydration chamber in Section 2.6, which was capable of bringing the sample into contact with a temporary metal liquid contact. The liquid metal used, (EGaIn, (Sigma-Aldrich)), is able to be de-contacted mechanically when the sample is lifted up, which then allows the film to be exposed to the hydrating atmosphere. For a schematic of the system use, see the Appendix, Figure S2.9. The electrical measurement procedure and hydration procedure was the same as described above.

3.2.4. Modelling of the AC data

Modelling was achieved utilising the EC-lab demo software. A common issue with fitting AC equivalent circuits is the possible number of variables. The more free parameters are included the better a fit one can obtain, though the confidence in the meaning of those parameters decreases. This has been demonstrated, quite amusingly, by a paper [145] that attempted to prove an old story about John von Neumann, who claimed that he could fit an elephant with just 3 parameters, and make its tail wag using 4. The paper goes on to demonstrate that this is indeed possible. The point though is quite clear, that curve fitting is a weak method and should be done with the minimum number of free parameters. As such in the modelling below, great care was taken to use the minimum number of free parameters that were justifiable from the literature and fitting procedure.

The basic circuit that was found that fitted well and had the fewest possible number of free parameters can be seen in Figure 3.3. The elements are briefly described below, but the reason and interpretation is left for the results section.

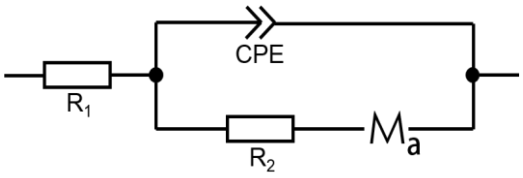

Figure 3.3. The equivalent circuit used to model the impedance data. It includes a contact resistance (R_1), a constant phase element (CPE), an ionic displacement resistance (R_2) and a modified restricted diffusion element (M_a).

The modelling parameters used, begin with the standard resistor element, of which there are 2 in the circuit, labelled R_1 and R_2. The impedance is described as

$$Z_R = R \qquad \text{(Eq. 3.9)}$$

where R is resistance. The constant phase element or CPE is an element that is essentially a capacitor with a slight modification to its phase and is given by

$$Z_{CPE} = \frac{1}{[Q \cdot (j \cdot \omega)^n]} \quad \text{(Eq. 3.10)}$$

where ω is the AC frequency, 0 < n < 1, and Q is the admittance of an ideal capacitance. It is important to note that when n = 1, the CPE behaves as a pure capacitor, while when n = 0, the CPE behaves as a pure resistor. Hence n changes the phase in a consistent way. Finally, there is the modified restricted diffusion element (M_a) which is based upon the Warburg element. It captures mass diffusion for charged particles such as ions:

$$Z_W = R_1 \frac{\coth(\tau_1 j 2\pi f)^{\alpha_1/2}}{(\tau_1 j 2\pi f)^{\alpha_1/2}} \quad \text{(Eq. 3.11)}$$

where $\alpha_1 = \pi/2$ the Warburg element is recovered.

All fitting parameters for the data sets can be seen in the Appendix, Table S3.1.

3.3. Results and discussion

Presented in Figure 3.4 ((a) to (e)) are the Nyquist plots of eumelanin thin films exposed to a water vapour (D_2O data with fits are presented in the Appendix, Figure S3.1) measured on samples with an Ag top gate. It can be observed that the plots display a circular-like shape in the high-frequency region and an inclined tail in the low-frequency region. However, there is a clear progression with exposing eumelanin to a hydrated atmosphere. At vacuum, when the eumelanin film is completely dry, only a part of a semicircle can be seen, which is indicative of a parallel capacitor/resistor circuit with no evidence of a tail. This is expected, since the protonic charge density of eumelanin should be very low under vacuum. When the pressure is increased to 5 (relative pressure 0.21) and then to 10 mbar (relative pressure 0.42), a low frequency tail (right side of the plot) manifests itself and indicates a potential ionic diffusion contribution. This tail starts to dominate with further increases in pressure until at a high hydration level the tail is the only significant feature.

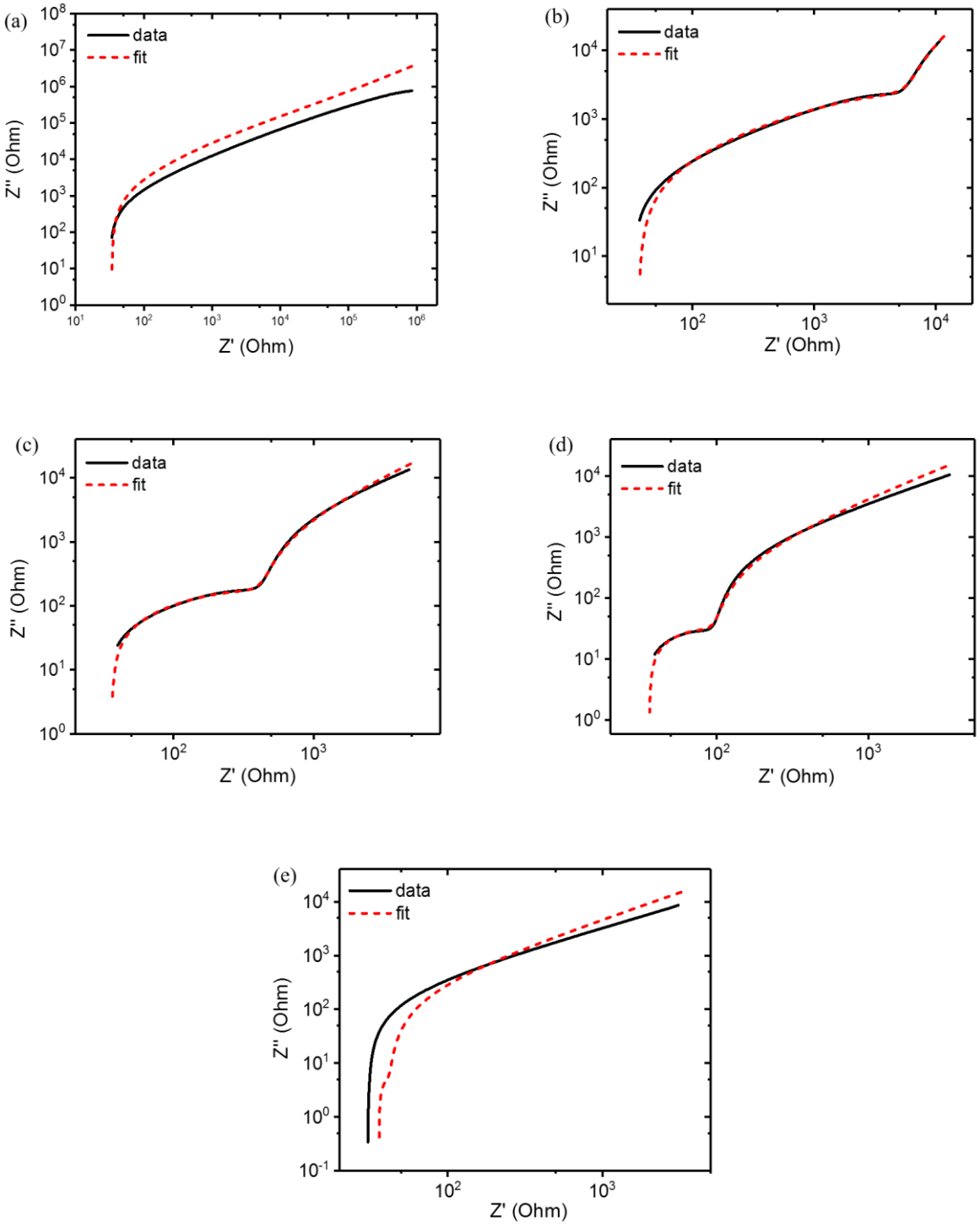

Figure 3.4. Nyquist plots for eumelanin films exposed to H_2O with associated modelling (relative pressures are 0 (a), 0.21 (b), 0.42 (c), 0.63 (d) and 0.83 (e) respectively). Note: the low frequency regime corresponds to high Z′ and vice versa.

The model captures the high frequency response, especially when the film is hydrated, but fails in the low frequency regime. The model fits are shown as dashed red lines. It is clear that the low frequency data does not exhibit a uniform slope as a function of frequency. To the author's knowledge, no diffusion circuit element is currently able to capture a changing gradient diffusion tail.

Hence, it is believed that the circuit is a reasonable, simple model that captures the essence of the material behaviour in relation to ion diffusion. It should also be noted, as one would expect, that the dry films show no low frequency tail since according to Figure 3.1 there will be a low concentration of free protons. However, for consistency the same equivalent circuit was applied to all hydrations.

To obtain a more complete set of hydration dependent data and to cross-check the equilibrium conditions, samples were prepared without the Ag top contact and utilising the EGaIn top contact as described in Section 3.2.3. The hydration chamber was evacuated for 2 hours to reach vacuum. Each next pressure was held for an hour before taking data to insure equilibrium was reached. The results obtained with the EGaIn contact are shown in Figure 3.5.

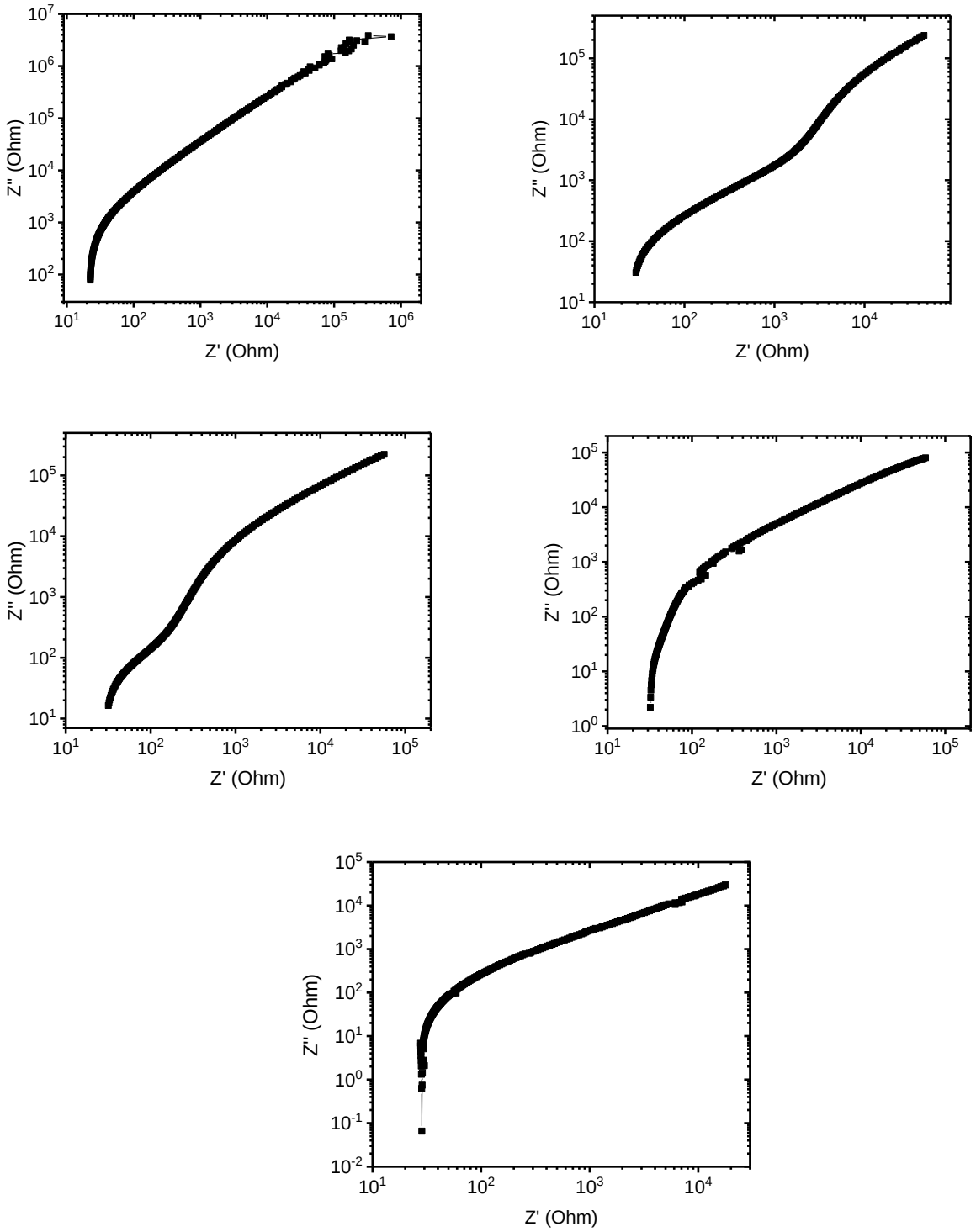

Figure 3.5. Nyquist plots for eumelanin films exposed to H_2O (relative pressures are 0 (a), 0.21 (b), 0.42 (c), 0.63 (d) and 0.83 (e) respectively), utilising the EGaIn top contact.

It can be observed that the plots look similar to those obtained for the samples with the top Ag contact. At vacuum, when the eumelanin film is dry, a tail cannot be observed, indicating a parallel capacitor/resistor circuit (low proton concentration). The tail feature appears when the pressure is increased to 5 mbar (relative pressure 0.21) and 10 mbar (relative pressure 0.42), indicating ionic

diffusion in the film. At 15 mbar (relative pressure 0.63) and 20 mbar (relative pressure 0.83) the tail dominates and no semicircle-like feature is present.

Comparing the results obtained from the above two sets of experiments, it can be seen that the trends are the same with pressures up to 15 mbar, which shows that standard devices, which have an evaporated top contact, come into equilibrium with the environment. However, the latter data set shows some distorted behaviour at high frequencies, especially at the higher hydration levels. This can be ascribed to a high frequency contact response in the EGaIn, which would be expected in a liquid metal.

Considering all the above, the data set with the Ag top contact will now be treated as the nominal data set. Comparing the effects of H_2O and D_2O reveals that there are no major differences in extracted parameters (Figure 3.6 and Figure 3.8). However, a puzzle remained since previous work on melanin showed a significant difference between the effects of D_2O and H_2O [113]. In addition, other related work on cephalopod proteins [83] showed that kinetic isotope effects could be observed. Upon inspecting the previous literature more carefully, it became clear that the AC measurements under consideration in this current work were performed on thin films with far narrower electrode gaps (of order 70 nm, i.e., the film thickness) and hence the amount of active material available to enhance the KIE appears to be far too small. As such the used thin film configuration was simply not sensitive to them. As such, the conclusions drawn are applicable to both H_2O and D_2O for the thin film eumelanin samples.

As mentioned previously, the literature suggests that eumelanin is a mixed electronic/ionic conductor [66, 81]. However, there is no electronic component included in the model, nor did our attempts to include one lead to any reasonable fit of the experimental data. To further confirm this observation, the displacement current resistance (R_2) and the capacitance of the CPE were plotted as a function of hydration (Figure 3.6).

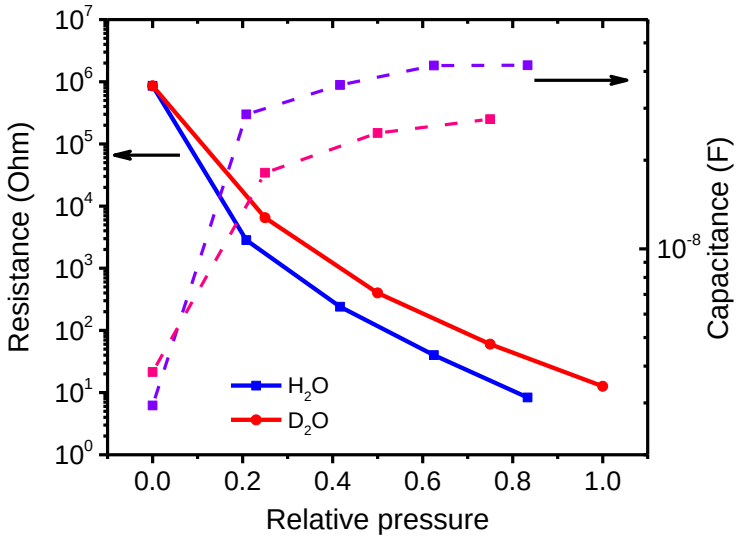

Figure 3.6. The modelled displacement current resistance (R_2) and CPE capacitance as a function of hydration in eumelanin thin films. The type of water is indicated in the legend.

From the figure it can be seen that the displacement resistance decreases exponentially with hydration over 5 orders of magnitude. This indicates that the ionic current is increasing exponentially, which based upon previous work, is in line with an exponential increase in the proton charge density. The dramatic change observed here is unexpected, because previous work on pressed powder samples achieved only about 1 ½ orders increase for H_2O exposure and 2 ½ orders for D_2O exposure. The capacitance shows a much smaller change, only about one order of magnitude increase. This increase is most likely due to a change in the dielectric constant of the sample, since water (a high dielectric constant material) is absorbed in large quantities into the film.

The frequency dependent plots were normalised to real and complex dielectric response functions. To do so, the thicknesses of the samples had to be known and the change with hydration had to be anticipated. As such the thicknesses were measured at ambient using a Dektak XT profilometer, with films thicknesses of ~70 nm determined. To calculate the dielectric constant for the real and imaginary parts of the impedance, the determined following equations were used:

$$\varepsilon' = \frac{C \times d}{\varepsilon_0 A}; \; \varepsilon'' = \frac{d}{\omega R_p A \varepsilon_0} \qquad \text{(Eq. 3.12)}$$

where C is the measured capacitance, d is the thickness (different for each hydration), ε_0 is the permittivity, R_p is the measured resistance, A is the sample area. The hydration dependent thickness changes were determined using the neutron reflectometry data [129] in Chapter 2, Section 2.5. These thickness changes were taken into account when calculating the dielectric response for each level of hydration (Figure 3.7).

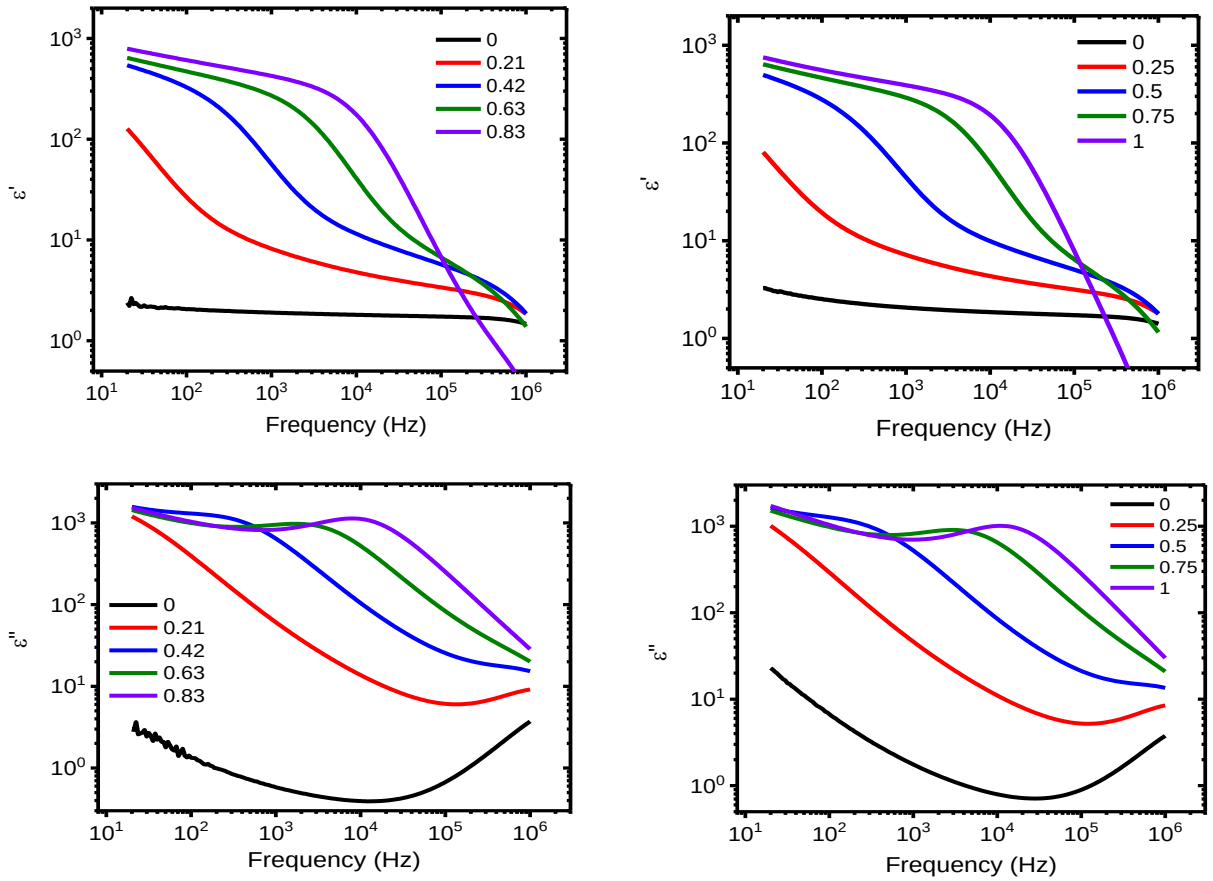

Figure 3.7. Real (top) and imaginary (bottom) components of the dielectric response as a function of frequency for eumelanin thin films exposed to H_2O (left) and D_2O (right). The relative pressure is indicated in the legend.

Returning to the ionic conductivity discussion, in order to estimate the ion conductivity, it is useful to first present the dielectric responses ε (both the real and imaginary components) *versus* frequency for both D_2O and H_2O hydration (Figure 3.7) [146]. Surprisingly, for the hydrated samples, the real component maintains a high value between 0.5 – 1.0 x 10^3 across a wide frequency range (20 – 10^4 Hz). This observation is consistent with recent reports of eumelanin being used a battery storage medium [147], but nonetheless is an important and intriguing outcome of these dielectric measurements. Whether these values are attributed to electrostatic or pseudo capacitive or a combination of effects are to be determined.

Using the data presented in Figure 3.7, the ionic conductivity can be estimated by observing that ionic currents dominate at low frequency [146]. Hence, the simple relationship $\varepsilon'' \sim \sigma/\omega$ can be used for the low frequency regime, where σ is the conductivity (ionic) and ω is the radial frequency [146]. However, it is important to note that there may be two competing effects at low hydration, the ion current, but also electrode polarization effects (i.e. the formation of an electric double layer at the electrode interface) [146, 148]. A signature feature for the latter is if a secondary "step" increase can be observed in ε′ with a concomitant increase in ε″ at low frequencies (typically around 10^{-2} Hz) [146].

Such features are not observed here, thus the low frequency behaviour in Figure 3.7 can be assigned to ion charge transport.

Using this knowledge and the data from Figure 3.7, a conductivity curve was plotted as a function of relative pressure (Figure 3.8). This plot is essentially equivalent to the DC data of Figure 3.6.

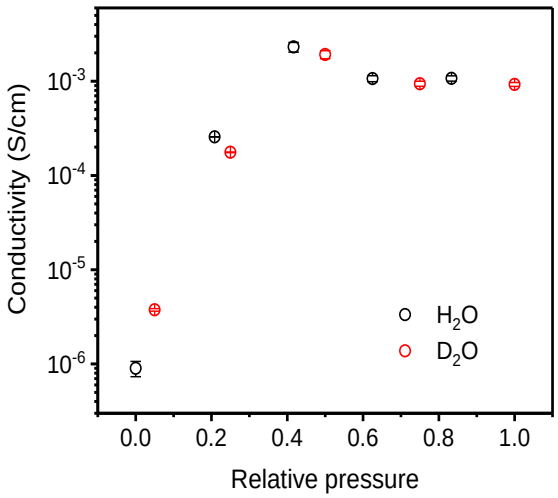

Figure 3.8. The conductivity of eumelanin thin films as a function of relative pressure for both H2O and D2O. The conductivity data was determined within a frequency range of 20-60 Hz. Error bars are indicated and were calculated to 2 times the standard error.

The calculated conductivity in Figure 3.8 shows three orders of magnitude increase over a range vacuum to fully hydrated, which is significantly larger than the results obtained for pressed eumelanin pellets. Thin films used in the work described in this Chapter, were dense and swell, which effected the thickness of the sample. Conductivity is dependent on thickness, so the fact that such differences in the results are observed between pellets and thin films could be due to the fact that the thickness of the pellets was assumed to be constant, because no other evidence was available at that time. For the results presented in this thesis, the data has been normalised using recently published findings on Neutron Reflectometry of hydrated eumelanin thin films [129], described in Chapter 2. Because the morphology of the film and geometry of the sample make the effective applied voltages different to those used previously, the conductivity calculated here is more accurate. Furthermore, Figure 3.8 shows saturation in conductivity after 0.4 RP. As discussed in previously (Chapter 1), the comproportionation reaction stands behind the origins of eumelanin's conductivity and it can be modulated with hydration. It seems plausible that saturation of the comproportionation reaction would lead to saturation in conductivity.

Finally, it is clear that the low frequency conductivity determined in Figure 3.8 is protonic in origin and as such is the dominating DC component.

3.4. Summary

In conclusion, using hydration controlled impedance measurements the nature of the dominant charge carrier in solid-state eumelanin has been probed. A systematic growth in the low frequency response was observed as hydration increased for both D_2O and H_2O adsorption. The high frequency component appeared invariant. This is strongly suggestive of the main component of the current being ionic. A minimal equivalent circuit was developed to describe this behaviour, the salient features of which were a constant phase element and resistor representing the ionic displacement current with a modified restricted diffusion element in series. All the Nyquist impedance plots fit this circuit, and no combination of elements delivered a significant electronic component. The modelling therefore confirms the dominant current component to be ionic (protonic). Determination of the dielectric constant (real and imaginary parts) allowed the ionic conductivity to be estimated. Significant changes dry-to-wet of ~3 orders of magnitude were observed. An unexpected and interesting finding from these measurements was the high real part of the dielectric constant (~10^3) over a wide frequency range (20 to 10^4 Hz). The findings described in this Chapter are significant since they strongly indicate that eumelanin is not a mixed hybrid electronic-ionic conductor as previously thought – but a proton transport material, which makes it an ideal proton top gate material for a solid state OECT. Since there is no electronic charge contribution to the charge transport in eumelanin, it can be assumed that there will be no significant electronic injection from the eumelanin bulk into the bulk of a PEDOT:PSS channel film, which makes the interpretation of solid state eumelanin based OECTs much simpler.

4. Eumelanin-based OECTs

4.1. Introduction

State-of-the-art OECTs are intrinsically limited by the liquid electrolytic gate. Although the biological environment is 'wet and warm', any read–write–sense device should ideally be all solid-state from the perspectives of stability, long term operation, reproducibility and very importantly, miniaturization and integration, therefore the realization of scalable all-solid-state architectures is now a priority in bioelectronics. As was discussed in Chapter 2, eumelanin is a great potential material for the fabrication of thin films that can be incorporated into devices. Furthermore, eumelanin is a proton conductor (see Chapter 3), which makes an excellent candidate for making a proton top gate for a solid state OECT. This is the subject of the work described in this Chapter.

4.2. Experimental methodology

4.2.1. Eumelanin synthesis and device fabrication

Euelanin was synthesized and solutions were prepared as described in Chapter 2, section 2.1. Glass slides (14.9 mm x 14.9 mm) were cleaned as described previously. The solid-state OECTs were prepared as follows: gold source and drain electrodes were thermally evaporated using a shadow mask to define the length and width of the channel area (100 μm and 11.2 mm respectively) onto the pre-cleaned glass slides. The mask had interdigitated contact patterns to increase the active area of the channel and reduce resistance, hence improving sensitivity. PEDOT:PSS (Clevios PH 1000, Heraeus Holding GmbH) films were spin-coated on the substrates for 5 s at 500 rpm followed by 60 s at 1500 rpm and annealed for 15 min at 140°C. A monolayer of Hexamethyldisilazane (Sigma-Aldrich) was spin coated on top of the PEDOT:PSS at 800 rpm for 60 s followed by 15 min annealing at 110°C. Hexamethyldisilazane is a compound that is used in photolithography as a passivation layer. In this case it acted as a hydrophobic layer between the PEDOT:PSS and eumelanin. A thin film of eumelanin was spin coated on top of the PEDOT:PSS at 1500 rpm for 60 s and the device was finished with a 30 nm Au top gate contact (thermally evaporated). Capacitance measurements were performed using different thicknesses of PEDOT:PSS channel of 50 nm, 100nm, 200nm and 400nm. To obtain films of different thickness, the same solution was used, however, the spin-coating procedure was modified. Faster spin speeds (up to 2500 rpm) were used to create thinner films, while slower spin speeds (down to 1000 rpm) and shorter spin times were used to obtain thicker films. All thicknesses were measured using a DEKTAK XT profilometer. Each sample consisted of 3 transistors with multiple samples fabricated for each type of experiment. Humidity dependent experiments were performed without gold top gate contact. A schematic of the created devices is shown in Figure 4.1.

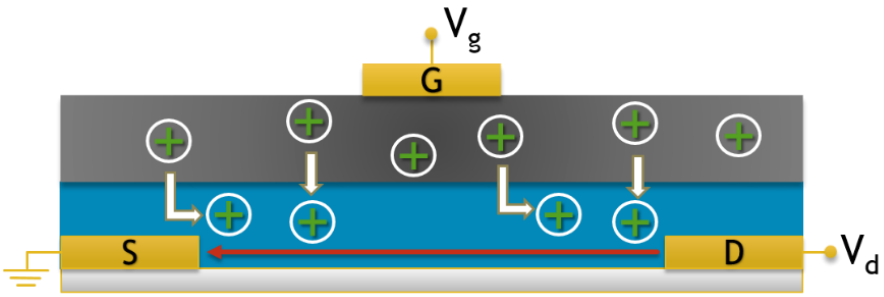

Figure 4.1. Schematic representation of an eumelanin-based organic electrochemical transistor. Blue corresponds to a PEDOT:PSS channel, dark grey to the eumelanin gate and S, D and G are the source, drain and gate electrodes respectively. Red arrow shows the direction of the current flow.

4.2.2. Hydration dependent conductivity

Humidity dependent experiments were performed in a vacuum capable chamber using a custom made temporary contact system utilizing EGaIn (eutectic gallium–indium, Sigma-Aldrich) as a top gate electrode, as described in Chapter 3. The chamber was pumped down to a vacuum of ~10^{-2} Torr for 2 hours using a rotary pump. The desired water pressure was reached by isolating the pump and bleeding in water (Milli-Q, freeze-that-pumped 3 times) vapour measured with a BOC-Edwards GK series (0–50 mbar) gauge. Each pressure was held for an hour to insure an equilibrium was reached. Adsorption isotherm measurements [112, 129] previously demonstrated that at least an hour is required to achieve equilibrium water content in eumelanin pressed powder pellets and films. To ensure equilibrium hydration conditions, a time dependent current measurement was performed before each of the pressure points (Figure 4.2). The figure shows that less than 30 min is needed to reach equilibrium. Nevertheless, all samples were stored in a chamber for an hour before each change of pressure to insure equilibrium was reached. Furthermore, the decrease in the channel current with hydration indicates that the PEDOT:PSS is being hydrated, and incorporating passively diffusing protons from eumelanin into its matrix.

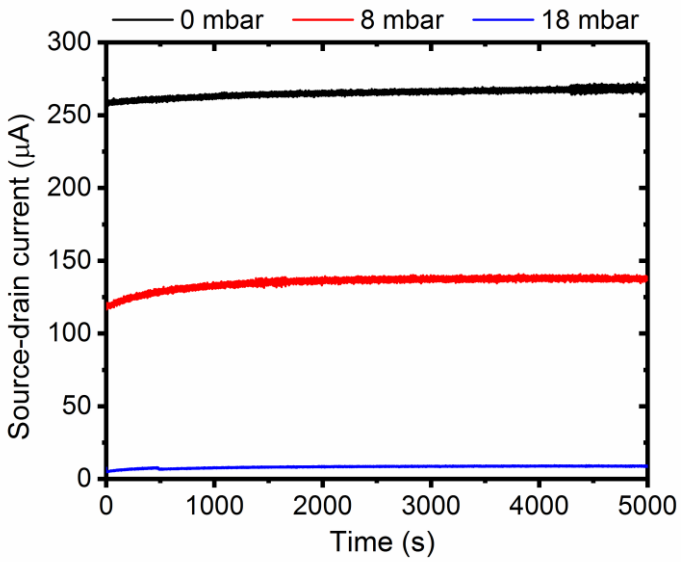

Figure 4.2. Time dependent current measurements for an OECT exposed to a wet atmosphere without the EGaIn top contact.

After equilibration transistor devices were placed into contact with the liquid gate, and then the transistor characteristics were measured. Before increasing the pressure, the top liquid gate contact was lifted to insure an equilibrium in the eumelanin film was reached for the next pressure. The stability of devices and reproducibility of obtained results were also tested by performing multiple transfer cycles (Figure 4.3). For a gold-contact OECT (Figure 4.3(a)) each transfer curve was measured 2 min after the previous. For the EGaIn-electrode device (Figure 4.3(b)) each transfer curve was measured after lifting the sample up and lowering it back down to create the same contact area.

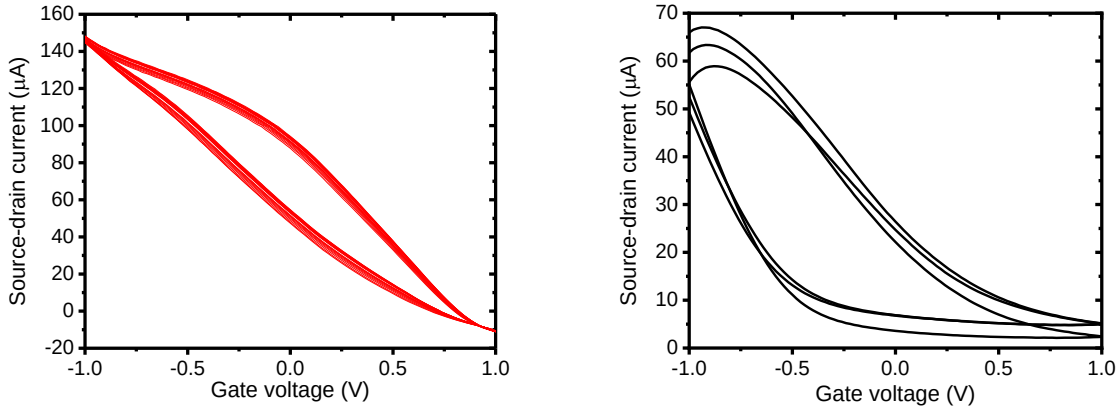

Figure 4.3. Reproducibility curves of a eumelanin-based OECT measured at ambient conditions. Reproducibility of a eumelanin based OECT with a gold top gate contact (a), and an EGaIn top-gate electrode (b). The source-drain voltage was 100 mV. For both types of devices very good reproducibility was achieved. Three cycles for each device are presented.

An example of the gate leakage current can be seen in Figure 4.4. Using a liquid gate contact decreased the source-gate leakage by almost an order of magnitude. The gold contact evaporated on the eumelanin gate surface partially blocks water penetration through the film.

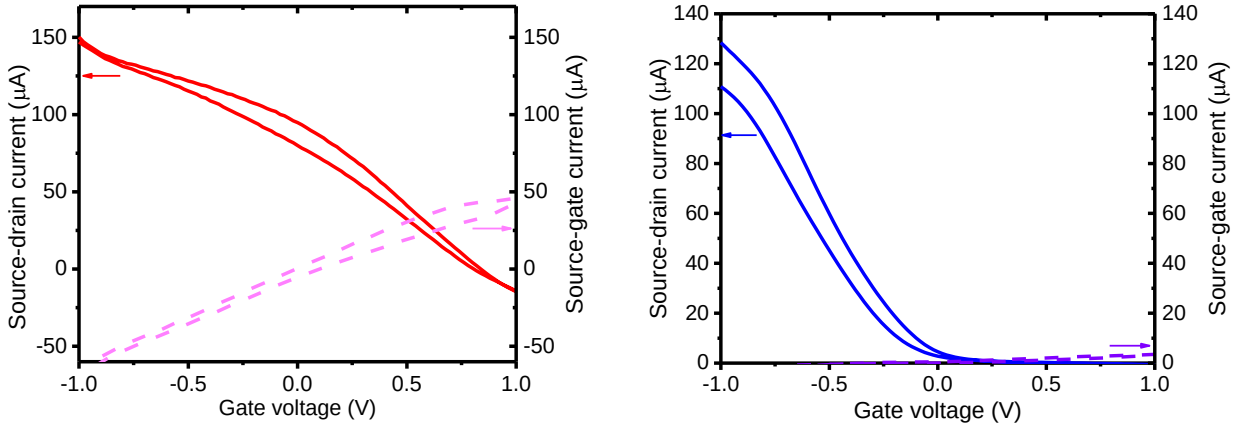

Figure 4.4. Source-gate leakage current examples measured at ambient conditions. Source-gate leakage current for a gold top gate contact (a), and an EGaIn top gate contact (b) OECT. The source-drain voltage was 100 mV.

4.3. Results and discussion

4.3.1. Electrical characteristics under ambient conditions

The electrical characteristics of devices were measured using a probe-station and an Agilent Semiconductor Device Analyzer (B1500A). Transfer curves were obtained with applied source-drain voltage (V_d) of 100 mV and gate voltage (V_g) sweeping from -1 V to 1 V. The hold time (the time before taking the first data point) for all measurements remained constant at 60 s. The influence of the delay time (the time between data points) on the transfer characteristics of the devices was inspected using delay times of 100 ms, 200 ms, 500 ms, 1 s, 2 s and 5 s. All output curves were measured slowly enough to allow steady state to be reached (delay time 5 s, hold time 60 s).

A critical step in the transistor fabrication was the deposition of a Hexamethyldisilozane (HMDS) monolayer on top of the channel prior to spin coating the gate. As it was mentioned in Section 4.2, the HMDS hydrophobically modified the PEDOT:PSS which otherwise would have re-dissolved in the basic pH, aqueous eumelanin deposition solution causing shorting between gate and source–drain contacts. The eumelanin gate was contacted using a gold top electrode thermally evaporated at low energy such as not to cause electrode ingress. In the first instance, these transistors were tested under ambient laboratory conditions in a standard manner by obtaining forward and back sweep transfer (Figure 4.5(a)) and output (Fig. 4.5(b)) characteristics. These ambient laboratory conditions provided enough natural moisture to render the eumelanin ‘conducting’, i.e. sufficient water to facilitate proton percolation [66] and hence test the solid-state gating concept.

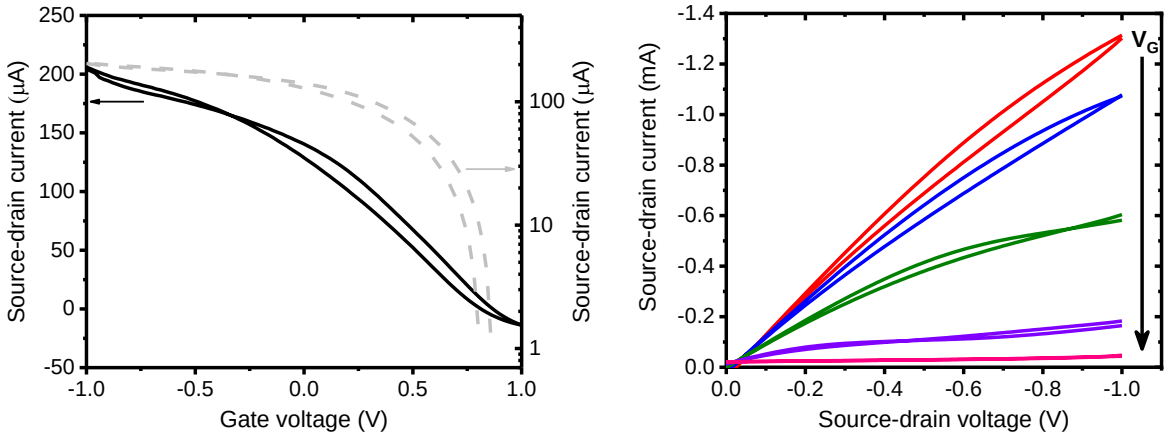

Figure 4.5. (a) Transistor transfer characteristic of a PEDOT:PSS channel (100 nm thick film, 100 μm channel length) eumelanin top gate and gold gate electrode measured at ambient conditions. The source-drain voltage 100 mV. Proton injection from the eumelanin top gate de-dopes the PEDOT:PSS channel reducing the source–drain current. The dashed line represents the on/off ratio. (b) Transistor output characteristic. The device behaves as a p-type transistor and as would be expected for positive ion injection.

The transfer curve on Figure 4.5(a) reveals that at zero gate voltage (V_g = 0 V) the transistor is in the "On" state with high current flowing through the channel (I_d). Upon application of a small positive gate voltage (~ 1 V), the transistor turns "Off". This behaviour is consistent with protons moving into the PEDOT:PSS, electrochemically de-doping and reducing the number density of free carriers available for conduction across the polymer backbone. The output characteristics in Figure 4.5(b) confirm p-type channel behaviour: in general, the relationship between I_d and V_d is almost linear for low V_d and all applied V_g, and with the application of larger negative V_d the current begins to saturate depending on V_g. In addition, Figure 4.5(b) shows almost complete channel turn-off with modest gate voltages (<1.0 V).

These transfer characteristics were obtained at V_d = 100 mV at a delay time of 1 s (1 data point per second). In Figure 4.5 ((a) and (b)) forward-back scan hysteresis is clearly visible. This is not unexpected in a device in which dynamics and operational principles originate from drift of ions (protons) under an applied field: the eumelanin gate is in essence a capacitor. To demonstrate this principle, the delay time (the time between data points) was varied. One would naturally expect the hysteresis to increase significantly with shorter delay times. This is indeed the case as shown in Figure 4.6, and at the shortest delay time (100 ms between data points), the device does not even turn off completely due to persistence of the space charge.

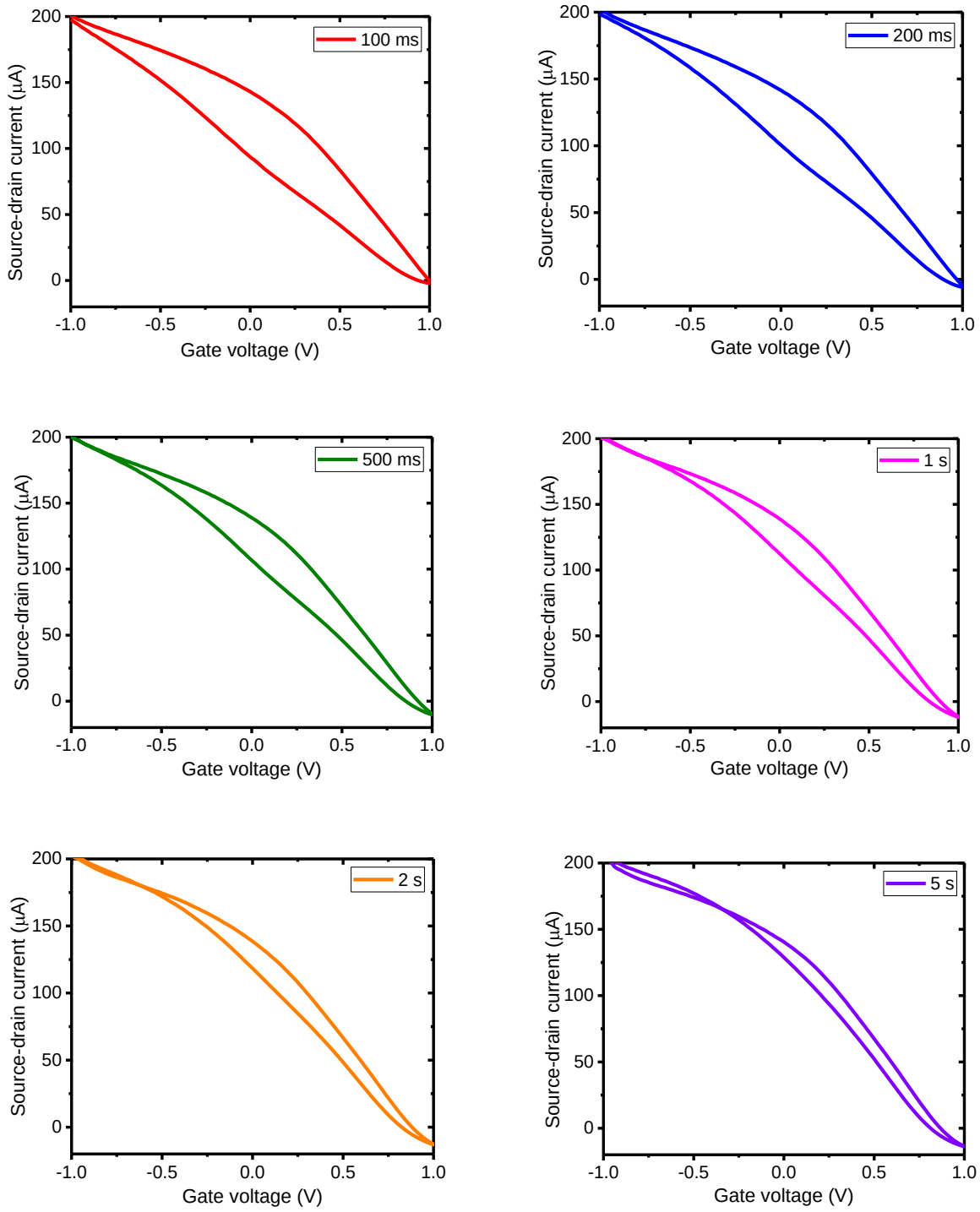

Figure 4.6. Transfer characteristics of a eumelanin-based OECT (100 nm channel thickness) measured at different delay times (time before data points). The source-drain voltage was 100 mV in all cases and the top contact was gold.

The lowest degree of hysteresis and complete device turn off was obtained at a delay time of 5 s. These behaviours are consistent with the proposed mechanism of proton injection into the PEDOT:PSS gate. Because the protons are large centre of mass that diffuse and/or drift slowly, it takes longer for a device to switch off. To add further credence to this assertion, an attempt was made

to prove the eumelanin gate to be a proton source (as merely opposed to an inductive dielectric) by varying the proton concentration. This is described in the next section.

4.3.2. Eumelanin conductivity as a function of hydration

As previously discussed, the electrical conductivity of eumelanin in various solid-state forms is strongly dependent upon its degree of hydration. This behaviour stems from the comproportionation reaction introduced previously, and can be simply understood as an increase in the number of free carriers (protons) with increased water content. Furthermore, the electrical conductivity appears to undergo a percolation transition at ~9–12% by weight hydration as a continuous water network is formed to facilitate complete site-to-site hopping [66, 81]. Thus, it can be predicted that as the eumelanin top gate of an OECT is hydrated, the following predictions can be made: an increased on/off ratio; a lower turn on/off gate voltage; lower source–drain current at a specific gate voltage; and a higher channel transconductance (g_m).

To test these predictions the hydration chamber described in Chapter 2 was used, once again utilising a liquid metal gate electrode EGaIn. This enabled exposure of the eumelanin top gate to a controlled hydrating atmosphere without the capping gold contact, and OECT characteristics to be obtained after the attainment of water adsorption equilibrium [81]. Figure 4.7 shows typical transfer characteristics of a device measured at different vapour pressures of water (0 mbar – dry; 8 mbar – low hydration below the percolation transition; 18 mbar – high hydration and above the percolation transition).

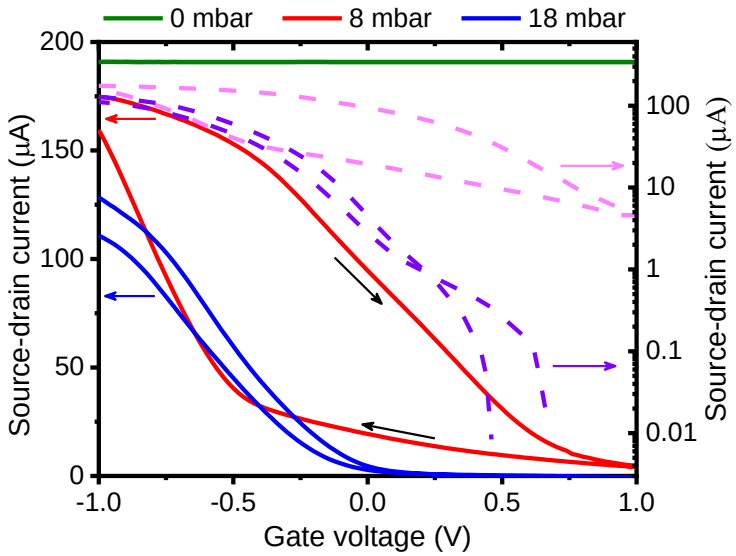

Figure 4.7. Hydration dependent transfer characteristics of a eumelanin-based OECT at 0 mbar water vapour pressure (green line), 8 mbar (red line) and 18 mbar (blue line). On/off ratio is represented by the dashed lines and is approximately 220 at 8 mbar and approximately 10^4 at 18 mbar pressure. The noise in the data at 0 mbar is negligible compared with the scale of the transfer curves.

The corresponding output curves are shown in Figure 4.8. A positive gate bias de-dopes the channel and decreases the absolute value of the current. These output characteristics show *p*-type behaviour.

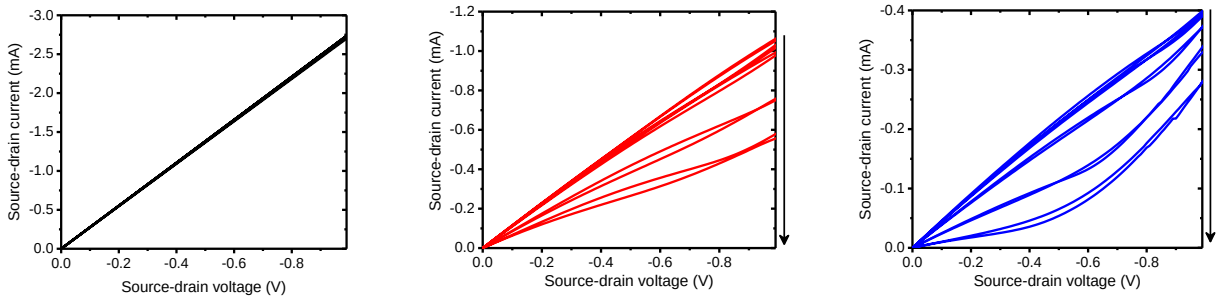

Figure 4.8. Output characteristics of a typical OECT (100 nm channel thickness) with a liquid top gate (EGaIn) contact under negative bias at the drain and held at 0 mbar (a), 8 mbar (b) and 18 mbar (c). The arrows indicate the direction of the gate voltage being changed from -1 to 1 V with a step of 0.5 V.

It can be noted that:

(1) when the gate is dry there is no transistor behaviour;

(2) there is a dramatic decrease in source–drain current and transistor characteristics are recovered at low hydrations(8 mbar);

(3) the transistor turn off voltage decreases considerably at 18 mbar (0.2 V) *versus* 8 mbar (1.0 V);

(4) the on/off ratio increases from ~200 at 8 mbar to $>10^4$ (comparable with a liquid gate OECT) at 18 mbar with V_d held at 100 mV.

The ratio of the change in I_d versus change in V_g is known as the channel transconductance (g_m). It is essentially the first derivative of the transfer characteristics and is used as an indication of device sensitivity, and a measure of the transistor switching voltage range. Figure 4.9 shows the transconductances derived from Figure 4.7 for the three hydration levels. As predicted the transconductance increases and the voltage operating range narrows as the gate hydration is increased.

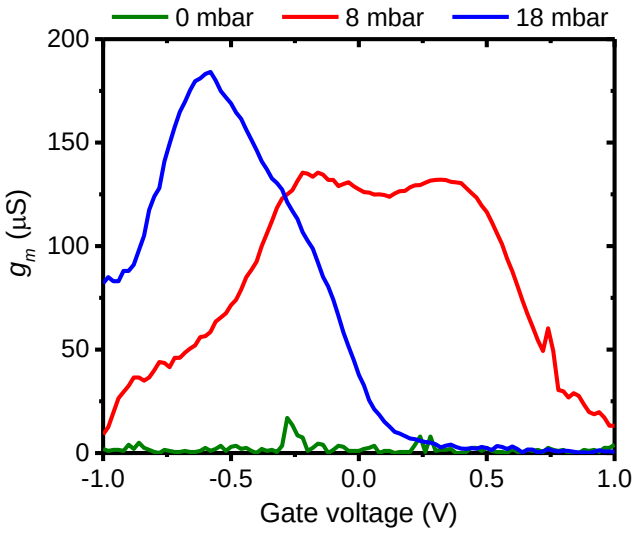

Figure 4.9. The corresponding transconductance (forward sweep), which reaches 175 mS at its peak.

A maximum transconductance of ~175 µS was recorded at 0.5 V and 18 mbar pressure. These observations agree with the predictions, and strongly support the assertion that the eumelanin is acting as a proton source and injecting gate.

4.3.3. Mechanistic discussion

In addition to the predictions and observations outlined above, it makes sense to test now whether this device is a true OECT rather than some novel organic field effect transistor (OFET) where the channel is inductively gated [14]. Rivnay *et al.* [27] recently demonstrated that the key difference between an OECT and an OFET is the role of capacitance. In an OFET, the surface capacitance of the dielectric/channel interface is paramount, while for the OECT the volumetric capacitance of the channel is the main operational driver. In the latter case, the 'thickness' of the PEDOT:PSS layer forming the channel becomes a relevant control parameter, and the basic transistor equations defining the source–drain current (I_d) and transconductance can be written:

$$I_d = (W\mu/L)dC_p^*\left[V_T - V_G + \frac{V_d}{2}\right]V_d \qquad \text{(Eq. 4.1)}$$

$$g_m = (W\mu/L)dC_p^*[V_T - V_G] \qquad \text{(Eq. 4.2)}$$

where W, L and d are the width, length and thickness of the channel, µ is the hole mobility of the channel, C_p* is the volumetric capacitance of the channel, V_T the threshold voltage, and g_m is the transconductance under saturation conditions.

To demonstrate that the volumetric capacitance is the active driving parameter in the devices (and hence confirm OECT operation), an additional set of experiments was performed, where the total charge injected was measured for different channel thicknesses (Figure 4.10(a)). There is a clear

linear behaviour for each channel thickness confirming volumetric capacitance, noting that surface capacitive gating would have yielded a thickness independence.

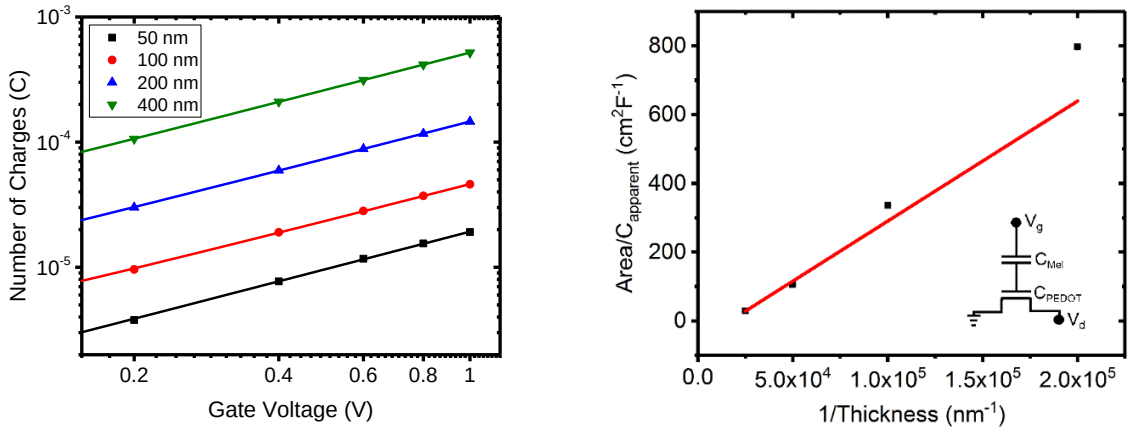

Figure 4.10. Capacitance measurements. (a) Charge injected into the OECT channel as a function of V_g for different PEDOT:PSS channel thicknesses while maintaining a eumelanin top gate of 70 nm. (b) The inverse capacitance against inverse thickness of the PEDOT:PSS channel. Inset shows the device to be a transistor with a two capacitor gate. Uncertainties were calculated to 2 times the standard error, but are too small for the resolution of the figure.

The volumetric capacitance can be determined from the slope of these charge-thickness plots, and for a liquid gated OECT this parameter remains constant [27]. However, slightly different slopes and hence volumetric capacitances as a function of channel thickness are observed. This behaviour can be assigned to the fact that the PEDOT:PSS and eumelanin top gate should be considered as two capacitors in series. This requires a modification of the model represented by Eq. 4.1 and Eq. 4.2. A full derivation of this generalized two capacitor OECT model is given below and the equivalent circuit shown as an inset in Figure 4.10(b).

Considering that eumelanin and PEDOT:PSS form two capacitors in series, the total capacitance of the system is given by:

$$\frac{1}{C_{tot}} = \frac{1}{C_m} + \frac{1}{C_p} \qquad \text{(Eq. 4.3)}$$

where *tot* indicates the total value, *m* is for eumelanin and *p* is for the PEDOT:PSS. The above now can be rewritten to account for the volumetric capacitances and the volumes of the materials:

$$\frac{1}{C_{tot}} = \frac{1}{C_m^* xyt} + \frac{1}{C_p^* xyd} \qquad \text{(Eq.4.4)}$$

where *xy* is the area of the electrical contacts, *d* is the PEDOT:PSS thickness and *t* is the eumelanin thickness, C_m^* is the volumetric capacitance of eumelanin and C_p^* is the volumetric capacitance of the PEDOT:PSS. The above can be normalized to contact surface area as follows:

$$\frac{xy}{C_{tot}} = \frac{1}{C_m^* t} + \frac{1}{C_p^* d} \qquad \text{(Eq. 4.5)}$$

This is the equation modelled in Figure 4.10b. Essentially, since the eumelanin thickness does not change, the equation shows that one can expect the left side to vary linearly with 1/*d*.

The original model for understanding liquid based OECTs was developed by Barnards *et al.* [31] and Rivnay *et al.* [27]. Below is an amendment to account for the eumelanin top gate which requires knowledge of how much protonic charge is in the PEDOT:PSS (assuming that the eumelanin is the proton source). Given the comproportionation reaction (presented in Chapter 2), it follows that the number of protons, from eumelanin, in PEDOT:PSS is equal to the number of semiquinone anions (SQ^-) stabilized at a given voltage. As such it can be assumed, under steady state conditions, that eumelanin is a capacitor stabilizing SQ^- ions and PEDOT:PSS is a capacitor housing protons. Therefore, at steady state, the total gate voltage across the device is given by:

$$V_g = V_m + V_p \quad \text{(Eq. 4.6)}$$

where *m* represents eumelanin and *p* PEDOT:PSS. Applying Kirchhoff's laws it can be stated that the charge on both capacitors is equal, thus:

$$V_g = \frac{Q}{C_m} + \frac{Q}{C_p} \quad \text{(Eq. 4.7)}$$

Given that the number of semiquinone anions equal to the number of protons, it can be written:

$$V_g = eN_H\left(\frac{1}{C_m} + \frac{1}{C_p}\right) \quad \text{(Eq. 4.8)}$$

where *e* is the fundamental charge, and N_H is the number of protons. It now can be rearranged:

$$N_H = \frac{V_g}{e\left(\frac{1}{C_m^* WLt} + \frac{1}{C_p^* WLd}\right)} \quad \text{(Eq. 4.9)}$$

where *W* is width of channel, *L* is length of the channel, *d* is thickness of PEDOT:PSS and *t* is thickness of eumelanin, and the * indicates volumetric capacitance. Continuing the derivation:

$$N_H = \frac{V_g}{\frac{e}{WL}\left(\frac{1}{C_m^* t} + \frac{1}{C_p^* d}\right)} \quad \text{(Eq. 4.10)}$$

$$N_H = \frac{V_g WL}{e\left(\frac{1}{C_m^* t} + \frac{1}{C_p^* d}\right)} \quad \text{(Eq. 4.11)}$$

$$N_H = \frac{V_g WL}{e\left(\frac{C_m^* t + C_p^* d}{C_m^* t C_p^* d}\right)} \quad \text{(Eq. 4.12)}$$

$$N_H = \frac{V_g WL C_m^* t C_p^* d}{e\left(C_m^* t + C_p^* d\right)} \quad \text{(Eq. 4.13)}$$

The density of charges in the PEDOT:PSS can be written as:

$$n_H = \frac{V_g C_m^* t C_p^*}{e\left(C_m^* t + C_p^* d\right)} \quad \text{(Eq. 4.14)}$$

Having derived the proton charge density in PEDOT:PSS, this new definition can be applied into the derivation of Bernards *et al.* and Rivnay *et al.* Beginning with Ohm's law for the PEDOT:PSS channel:

$$I_d = Wde\mu p(x)\frac{dV(x)}{dx} \quad \text{(Eq. 4.15)}$$

Where μ is the hole mobility and $p(x)$ is the hole density in a given position x in the channel. The hole density is given by:

$$p(x) = [SO_3^-] - H^+(x) \quad \text{(Eq. 4.16)}$$

where $[SO_3^-]$ is the density of sulfonate groups that are compensated with holes in neat PEDOT:PSS, and $H^+(x)$ is the proton density. This proton density given the gate voltage and source drain voltage at a given point $x(V(x))$ is then given by:

$$H^+(x) = \frac{C_m^* t C_p^*}{e\left(C_m^* t + C_p^* d\right)} V_g - \frac{C_m^* t C_p^*}{e\left(C_m^* t + C_p^* d\right)} V(x) \quad \text{(Eq. 4.17)}$$

Now this proton density can be substituted into the hole density and Ohm's law:

$$I_d = Wde\mu \frac{dV(x)}{dx}\left([SO_3^-] - \frac{C_m^* t C_p^*}{e\left(C_m^* t + C_p^* d\right)} V_g + \frac{C_m^* t C_p^*}{e\left(C_m^* t + C_p^* d\right)} V(x)\right) \quad \text{(Eq. 4.18)}$$

Let $\alpha = C_m^* t/\left(C_m^* t + C_p^* d\right)$, then:

$$I_d = Wd\mu\alpha C_p^* \frac{dV(x)}{dx}\left(\frac{e[SO_3^-]}{\alpha C_p^*} - V_g + V(x)\right) \quad \text{(Eq. 4.19)}$$

Integrating:

$$I_d L = Wd\mu\alpha C_p^* \left(\frac{e[SO_3^-]}{\alpha C_p^*} V_d - V_g V_d + \frac{V_d^2}{2}\right) \quad \text{(Eq. 4.20)}$$

where, L is the channel length and V_d is the source drain voltage. Continuing:

$$I_d = \frac{Wd\mu\alpha C_p^*}{L}\left(\frac{e[SO_3^-]}{\alpha C_p^*} - V_g + \frac{V_d}{2}\right) V_d \quad \text{(Eq. 4.21)}$$

$$I_d = \frac{Wd\mu\alpha C_p^*}{L}\left(\frac{V_T}{\alpha} - V_g + \frac{V_d}{2}\right) V_d \quad \text{(Eq. 4.22)}$$

To obtain the saturation condition, it can be assumed that $V_d = V_g - V_T/\alpha$, obtaining:

$$I_d = \frac{Wd\mu\alpha C_p^*}{L}\left(\frac{V_T}{\alpha} - V_g + \frac{V_g - \frac{V_T}{\alpha}}{2}\right)\left(V_g - \frac{V_T}{\alpha}\right) \quad \text{(Eq. 4.23)}$$

$$I_d = \frac{Wd\mu\alpha C_p^*}{L}\left(\frac{\frac{V_T}{\alpha} - V_g}{2}\right)\left(V_g - \frac{V_T}{\alpha}\right) \quad \text{(Eq. 4.24)}$$

$$I_d = \frac{Wd\mu\alpha C_p^*}{2L}\left(\frac{V_T}{\alpha} - V_g\right)\left(V_g - \frac{V_T}{\alpha}\right) \quad \text{(Eq. 4.25)}$$

$$I_d = -\frac{Wd\mu\alpha C_p^*}{2L}\left(\frac{V_T}{\alpha} - V_g\right)^2 \quad \text{(Eq. 4.26)}$$

which is the saturation current. Taking the derivative with respect to gate voltage yields the transconductance at saturation:

$$g_m = \frac{Wd\mu\alpha C_p^*}{L}\left(\frac{V_T}{\alpha} - V_g\right) \quad \text{(Eq. 4.27)}$$

Using these calculations, the capacitances of the eumelanin gate and PEDOT:PSS channel can be determined. The results of that analysis are shown in Figure 4.10b (inverse apparent capacitance versus inverse channel thickness). From the slope of Figure 4.10b a volumetric capacitance is obtained for the PEDOT:PSS channel 224 ±14 (2SE) F cm^{-3} and thus from α the eumelanin gate capacitance of 1420 ± 470 (2SE) F cm^{-3} (t = 70 nm).

The results outlined above confirm that volumetric gating in the OECT-based eumelanin-PEDOT:PSS transducer has been achieved. In general the capacitance measurements were also consistent with expectations. It should be noted that in literature PEDOT:PSS volumetric capacitance ranges between 34 F/cm^3 [155] and 327 F/cm^3 [156]. The difference between measured volumetric capacitance and the one reported by Rivnay *et al.* [27] can be simply understood by observing that the PEDOT:PSS was used as is, and not modified as in ref. [27]. The eumelanin top gate large capacitance is consistent with its reported supercapacitor properties [157]. In addition, Eq. 4.27 predicts that the transconductance at saturation (g_m) should vary linearly with channel thickness ($g_m \propto d \times \alpha C_p^*$, where αC_p^* is the apparent capacitance C_{app}^*). This is plotted in Figure 4.11 for numerous devices and the relationship is indeed linear. An example of the modelled output data is shown in Figure S4.1 of the Appendix.

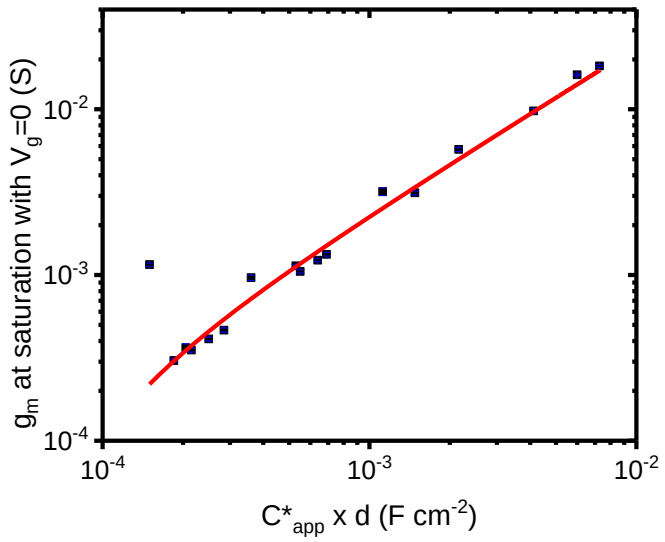

Figure 4.11. Transconductance at saturation calculated from the measured output characteristics (at V_g = 0 V) for multiple devices with different channel thicknesses. The red line shows a linear fit as predicted from Eq. 4.22 and Eq. 4.27. Uncertainties were calculated to 2 times the standard error, but are too small for the resolution of the figure.

Finally, it is worth noting that these results confirm that the aforementioned ENODe reported by van der Burgt *et al.* could indeed be functioning by direct cation injection into the postsynaptic electrode as proposed [154]. This underlines the importance of volumetric capacitance for low voltage operation of bioelectronic transducing interfaces. Like many reported transducing interfaces, it is important to note that these devices at this stage are merely proof of concept and have not been optimized for actual biological models and measurements. For example, the gold top contact for the device should be ultimately replaced by a biological target, which will act as the gate. Furthermore, the device architecture was not optimised for frequency response, which will most likely be required to improve the response time. This will be a necessary step in order to sense at high frequency neuronal cell activity as has been noted for other interfaces [32].

Bearing in mind that the reported devices are proof of concept, it is instructive to discuss their future potential by benchmarking performance against current PEDOT:PSS-based liquid OECTs. One figure of merit that can be used for benchmarking is the transconductance [26], since it is the main transistor parameter that governs signal amplification. State of the art PEDOT:PSS based OECTs have been reported [26, 27, 158, 159] with maximum/peak transconductances of ~5–20 mS and saturation transconductances of around 20 mS. For the eumelanin OECTs with fully hydrated top gates, a maximum/peak transconductance of around 0.175 mS (see Figure 4.9) and transconductances at saturation (Figure 4.11) of around 0.4–20 mS (depending on conductive channel thickness) were achieved. However, it is worthy of note that the most stable devices possessed channel thicknesses of ~100 nm, which yielded ~1 mS saturation transconductance. Thus, these devices are currently one order of magnitude lower in transconductance than state-of-the-art OECTs. However, OECT transconductances depend on device geometry/aspect ratio, as a simple inspection of Eq. 4.1 – 4.27 will show. These geometric considerations are well understood [27]. Transistors described in this thesis have aspect ratios (Wd/L) in the range of $4 \times 10^{-4} – 4 \times 10^{-3}$ µm. In contrast, as an example, Rivnay *et al.* [27] demonstrated devices in the range of $5 \times 10^{-2} – 5$ µm. Considering Rivnay *et al.*'s work as normative for what can be achieved easily with device engineering, re-engineering the devices presented in this thesis may increase the transconductance by a factor of 10^2, thus potentially surpassing current state-of-the-art devices by an order of magnitude.

These transconductance considerations have natural implications for transistor gain and hence sensitivity. OECT devices take a voltage input at the gate (ion signal) and translate it to a current signal at the drain [26, 158]. In order to extract a voltage signal, a load resistor can be connected to the drain of the transistor, from which the gain can be determined. At saturation, gain = $|dV_L/dV_g| = g_m R_L$, where g_m is the transconductance at saturation and R_L is a load resistor that is connected across the drain [26, 158]. Unfortunately, the transistors have not been operated in this drain resistor mode,

but the potential gain can be discussed by reference to the transconductance. The data in Figure 4.7 is for saturation at $V_g = 0$ V. This makes it comparable with recently published work on determining the gain in PEDOT:PSS-based OECTs [158]. These devices, with saturation transconductance values around 5 mS, yielded approximate gains of ~20 V/V. Assuming all else is equal, it would imply that the stable devices may have an amplification of 4 V/V if similar loads were utilised. It is worth of noting again that appropriate device engineering may yield devices of higher gain exceeding state-of-the-art. From the knowledge of the device scaling it can be estimated that a gain in the proton to electronic signal of around 100 V/V could be possible.

This potential for future performance promises new opportunities for direct bioelectronic transducing interfaces. Coupled with the solid-state architecture, real, functional devices that enhance and process signals, and which can be miniaturised, it opens up the exciting route of bioelectronics computing at the biological interface in vivo.

4.4. Summary

A functional, all-solid-state organic electrochemical *p*-type transistor was demonstrated with a proton injecting top gate made from the conducting bio-macromolecule eumelanin. On/off ratios of ~10^4 were achieved with low voltage operation (<1.0 V). These transducers operate by "volumetric gating" – direct injection of protons into the semiconductor channel which modulates the channel current. Also a generic transistor model was developed to test and explain its operation, which should in principle be broadly applicable to all solid state OECT architectures by the inclusion of multiple volumetric capacitances. This simple all-solid-state architecture is amenable to miniaturization and a definitive step on the pathway to integrated bioelectronic logic.

5. Cu-eumelanin OECTs

5.1. Background and rationale

After developing the solid state OECT as reported in Chapter 4, the next natural step would be improving device characteristics (such as on/off ratio). The eumelanin based OECT performance could be improved or degraded depending on the hydration state of the eumelanin, with a higher hydration state, i.e. higher proton charge density, improving the transistor performance. This observation, that higher proton charge density improves transistor performance, naturally raises the question as to whether eumelanin as a material can be modified to yield more protons and thus enable the fabrication of improved devices.

Since the central mechanism for generating protons is based upon the comproportionation reaction (presented in Chapters 2 and 3), it is clear that perturbing this reaction so to generate more protons could be one approach. As such a promising method is to "dope" eumelanin with transition metal ions, with eumelanin known to be an excellent metal ion chelator [r]. It is worthy of note the term "dope" used here refers to the process of adding dilute concentrations of an element into a conducting material for the purpose of enhancing the charge carrier density.

It is well documented that metal ions bind to eumelanin. There are different binding sites in eumelanin, depending on the metal-ion. These binding sites include amine groups, carboxylic acids, and hydroquinone catechol [104, 160]. Some of these binding sites directly affect the comproportionation reaction by binding to the semiquinone catechol moiety. Therefore, the prediction is that by appropriately selecting the metal ion, which could be bound to the semiquinone, the comproportionation reaction can be driven towards the production of additional semiquinone and protons. In turn, this shift in the reaction will lead to an increased proton charge density. There is a variety of transition metal-ions which have affinity for eumelanin, including Ni^{2+}, Fe^{2+}, Co^{2+}, Zi^{2+}, and Mn^{2+}. The addition of copper (II) (Cu II) to eumelanin is described in this Chapter. Cu (II) was chosen as a chelator due to the body of literature available on Cu-eumelanin solutions [104, 160-163]. Furthermore, copper has a high affinity for and tight binding [160, 162] to eumelanin. Among other metal ions found to be naturally bound to eumelanin, copper is unique due to its importance in eumelanin biosynthesis [93], where it plays a central role for eumelanin regulation and function in the human body. Furthermore, the metalloenzyme tyrosinase, the enzyme responsible for eumelanin synthesis *in vivo*, is activated by copper.

There are previously reported conductivity studies on synthetic eumelanin doped with Cu(II) ions [97]. The electrical measurements, performed under vacuum (dry), showed no significant changes with the addition of copper at room temperature. However, some differences were revealed

with the variation of temperature. As highlighted earlier, eumelanin's conductivity is hydration dependent and increases by orders of magnitude from dry (under vacuum) to wet (fully saturated) [66]. It is clear that a major gap of inquiry exist, i.e. investigation of the hydration dependent electrical conductivity of copper bound eumelanin.

Given the above, the fabrication, characterisation and the implementation of Cu-eumelanin thin films in an OECT device is the focus of this chapter. The increase in eumelanin conductivity will be shown by comparing a hydration controlled DC conductivity of Cu-eumelanin thin films against the synthetic neat eumelanin data presented in Chapter 2. Furthermore, the electrical characteristics of an OECT device based on Cu-eumelanin as a gating material will also be presented.

5.2. Cu-eumelanin thin films

5.2.1. Thin film fabrication technology

Eumelanin was synthesized and a eumelanin solution was prepared as described in Chapter 2, section 2.1. To obtain a Cu-eumelanin solution, 8 mg of a Cu salt (Copper II chloride dihydrate, Sigma-Aldrich) was mixed with 2 ml of eumelanin solution and stirred for 1 min, 2min, 3 min and 5 min to obtain different concentrations of Cu bound into the eumelanin structure. Film thicknesses were measured using a Dektak XT. Thicknesses for the films produced with different solution stirring times are presented in Table 5.1.

Stirring time	1 min	2 min	3 min	5 min
Thickness	70 nm	190 nm	300 nm	1080 nm

Table 5.1. Thickness of the Cu-eumelanin thin films, stirred for a different amount of time and measured with a Dektak XT. One thickness is an average of three measurements.

It is important to note that the solution became thicker with stirring time and after stirring it for longer than 5 min it turned into paste and was impossible to be used in a spin coating fabrication procedure. The films made with longer stirring time became brittle and not suitable for measurements. The solution was filtered through a 0.45 μm PVDF/L filter (Simplepure) to eliminate larger particles and insure the homogeneity of the film. Then it was spin-coated (G3P Spincoater, Specialty Coating Systems) onto the substrates for 60 s at 1500 rpm.

5.2.2. UV-Vis characterisation

Since Cu-eumelanin thin films to date have not been reported, a comparative characteristic study was undertaken, essentially to see whether the Cu addition changed the optical and electrical properties of standard synthetic eumelanin. The first characteristic studied was the optical absorbance behaviour. For that purpose, a UV-Vis-NIR Spectrophotometer 5000 (Varian) was utilised and Cary WinUV (Agilent Technologies) software was used to record the data. Similarly to described in Chapter 2, the absorbance of a Cu-eumelanin thin film spun cast onto a glass substrate was measured against a clear glass slide. This was repeated for each of the Cu concentrations (i.e. stirring times). Figure 5.1(a) shows typical Cu-eumelanin thin film spectra for different stirring times. As can be seen, the spectra exhibit a decaying exponential behaviour as a function of increasing wavelength, as was observed for pristine eumelanin thin films (See Chapter 2, Figure 2.1). Furthermore, it can be observed that the absorbance increases with increasing stirring time, which is likely due to an increased thickness of the films (see Table 5.1), with no essential change in the qualitative behaviour of the absorbance. Essentially, the change in the absorbance is due to an increasing absorption length. Note, the thicknesses of the films were determined after the UV-Vis measurements were completed and are highlighted in Section 5.2.1.

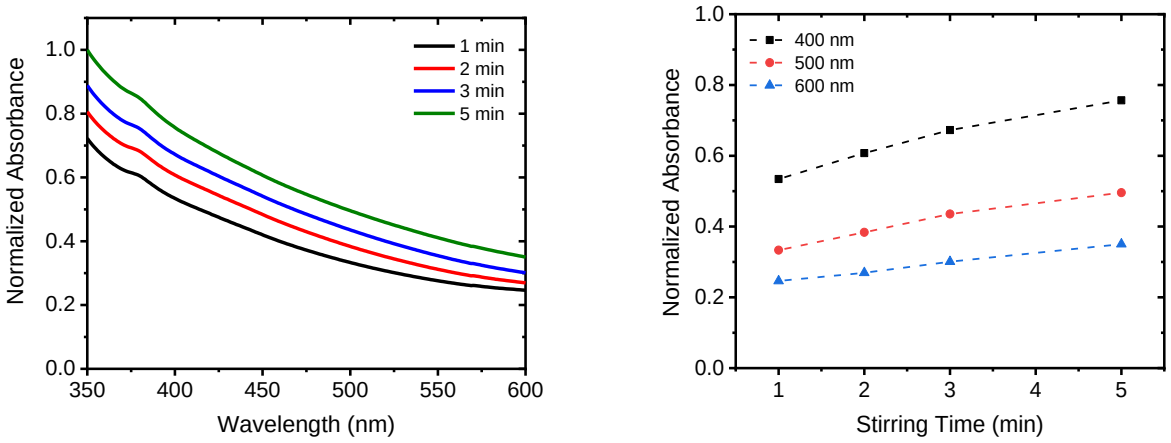

Figure 5.1. (a) The UV-visible absorption spectra of Cu-eumelanin thin films, as a function of thickness. The spectra follow decaying exponential behaviour. The data indicate that the Cu-eumelanin thin films show the same optical behaviour as eumelanin films. (b) The normalised absorption as a function of stirring time (film thickness) for different wavelengths, which indicates that the change in the absorbance is due to an increasing absorption length.

As can be seen from Figure 5.1, the same qualitative optical behaviour was observed for the Cu-eumelanin thin films as for eumelanin films. This would indicate that the light absorbing chemical moieties are not affected by the presence of Cu.

5.2.3. XPS characterisation

An elemental analysis of the Cu-eumelanin films was performed using XPS. XPS measurements were obtained using a Kratos Axis Ultra XPS Surface Analysis System with a monochromatic Al Ka X-ray source. Survey and high resolution scans were taken at 120 and 20 eV pass energies, respectively. The XPS spectra were analysed using CASA XPS software. Atomic ratios for C, N, Cu and O were determined from integrating areas under the C 1s, N 1s, Cu 2p and O 1s peaks using Shirley backgrounds for the peak modelling. As it was described in Chapter 2, the structure of the standard synthetic eumelanin is based on two heterogeneous polymers (DHI and DHICA). For DHI, the atomic percentages come to approximately 72% C, 18% O and 9% N. For DHICA, these percentages are 64% C, 29% O and 7% N. Figure 5.2(a) presents an example data set for Cu-eumelanin stirred for 5 min. The rest of the data for different stirring times can be found in the Appendix, Figure S5.1. The data shows that C, N, O ratios for Cu-eumelanin films are similar to that expected for standard eumelanin based on DHI and DHICA. Moreover, the atomic percentages previously obtained on pristine eumelanin (Chapter 2, section 2.4) are also in line with those presented here. Since the Cu concentration overall is low, it can be neglected in the calculation and the conclusion can be drawn that the synthesised material is still a true eumelanin.

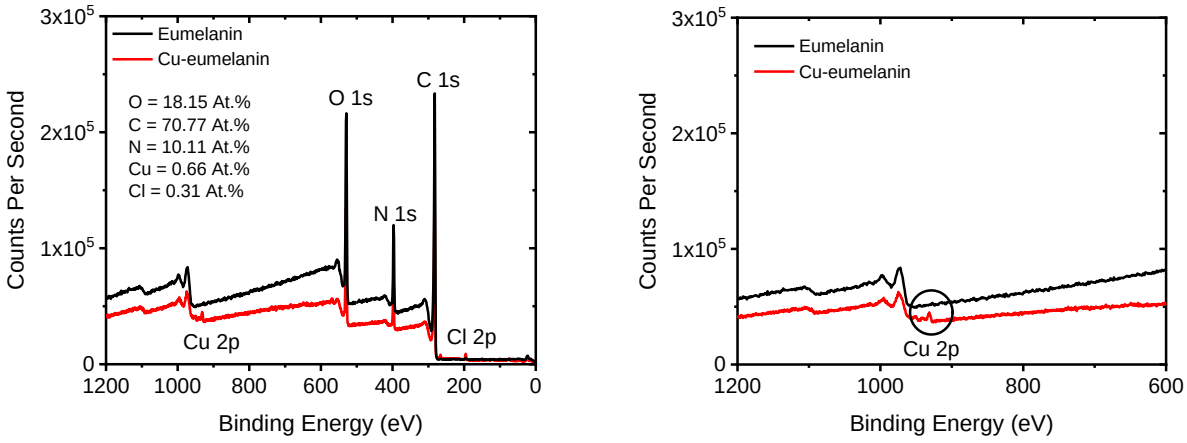

Figure 5.2. (a)XPS scans obtained on Cu-eumelanin thin film on glass substrates fabricated from a solution spun cast for 5 min (red) and eumelanin thin film on glass substrate (black). The curves are offset for clarity. (b) Cu peak region of the spectrum shown in (a). Atomic ratios indicated.

It is worthy of note that the Cu concentration increases with stirring time (Figure 5.3), which means that more copper is present in the film over time. This behaviour is indicative of enhanced polymerisation and is in line with the observations of the Cu-eumelanin thin film morphology and thickening of the casting solution.

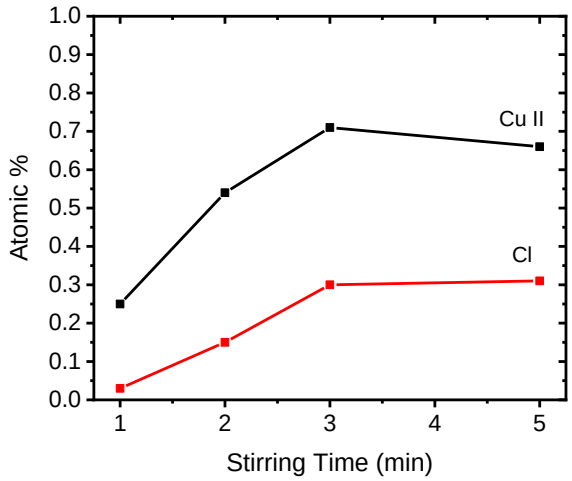

Figure 5.3. Percentage of Cu and Cl in Cu-eumelanin thin films as a function of a solution stirring time.

It can be seen that the atoms of Cu and Cl are present in the film, which is indicative of Cu salt being present in the solution. This suggests that the procedure for fabricating Cu-eumelanin thin films, described here, allows Cu to be incorporated into eumelanin and the only structural difference between the obtained films and pristine eumelanin is the presence of copper salt.

XPS data presented here confirms that increasing of the solution stirring time leads to the increased Cu (II) concentration in the eumelanin film. The atomic percentage of copper ions increases until the eumelanin becomes saturated. After stirring the solution for more than 3 min, no more copper can be bound.

5.2.4. AFM characterisation

To further characterise the Cu-eumelanin thin film properties, the surface morphology was investigated using tapping-mode Atomic Force Microscopy (AFM). Cu-eumelanin solutions were prepared, as described in section 5.2.1, and spun cast onto glass substrates which were pre-cleaned as described in section 2.1. to increase the hydrophilicity of the surface and improve the quality of the films. The AFM machine utilised was an Asylum Cypher High Resolution. The cantilevers (Budget Sensors) used for imaging had a resonant frequency of 75 kHz and a force constant of 3 N/m. All experiments were carried out under ambient conditions. Asylum Research software was used to collect and analyse the data. Data was obtained as a function of scan window size, i.e. image dimension, for each kind of film. This was especially important to determine the surface roughness of the films, since roughness can depend on image size and may not be representative of the entire film. Figure 5.4 ((a) to (e)) shows AFM images obtained for Cu-eumelanin thin films.

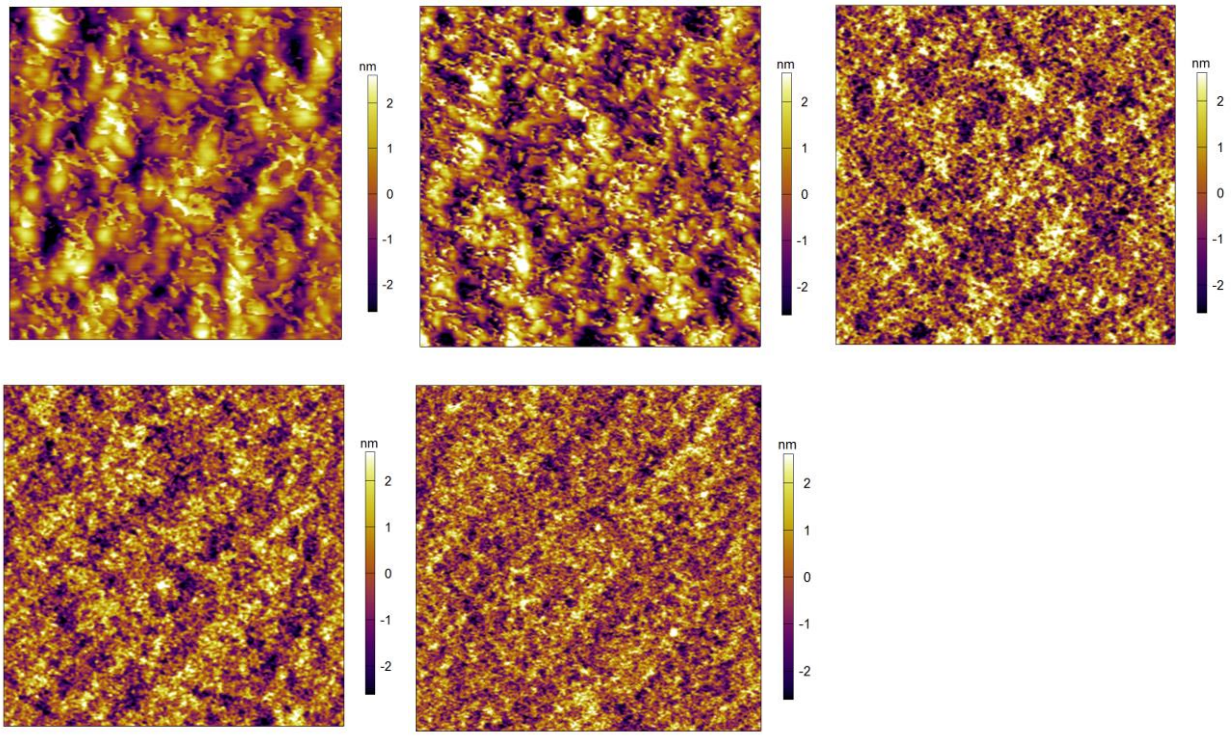

Figure 5.4. Topographic AFM images of a Cu-eumelanin thin film on a glass substrate taken at different image dimensions/magnifications: (a) 500x500 nm^2, (b) 1x1 μm^2, (c) 5x5 μm^2, (d) 10x10 μm^2, (e) 20x20 μm^2.

As can be seen in Figure 5.4, as the image dimension increases, the film morphology does not appear to change. This indicates that the Cu-eumelanin film remains homogeneous across a sample. The films presented here did not show any significant features, such as cavities or peaks. However, some large round formations can be seen (Figure 5.4(a)). The same formations were observed on eumelanin samples, described in Chapter 2. The bulb-looking formations indicate that Cu-eumelanin absorbed atmospheric water vapour [105], since Cu-eumelanin, like eumelanin, is hygroscopic and the measurements were done under ambient laboratory conditions. Adsorption isotherms measured on Cu-eumelanin pellets, showing the water absorption abilities of Cu-eumelanin [164], are presented in the Appendix (Figure S5.2).

At the highest magnification (Figure 5.4 (a) and (b)) the images indicate that the eumelanin film consists of densely packed granules. It can be concluded that similarly for eumelanin thin films, Cu-eumelanin "solutions" at high pH are likely to be colloidal suspension.

The surface roughness profiles for films on all substrates were obtained at each magnification, from which, the root-mean-square roughness of the films were determined by averaging over three images of the same sample. The resultant data is shown in Figure 5.5.

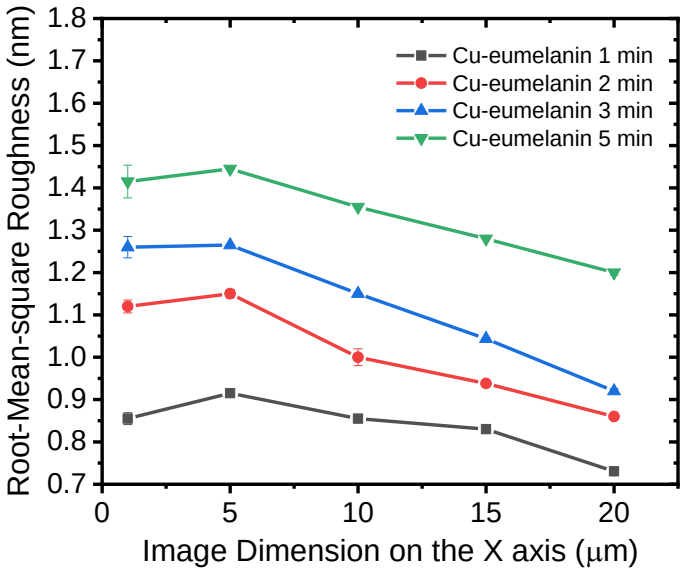

Figure 5.5. Root-mean-square roughness as a function of image size for different thickness (stirring time) of Cu-eumelanin thin films. As can be seen, the data indicates that the films do not exceed a roughness of greater than 2 nm. The error bars presented on the graph were calculated (2SE) across three different samples.

Figure 5.5 shows that regardless of the thickness (stirring time) the Cu-eumelanin casting process forms smooth films. Furthermore, this smoothness is relatively insensitive to image dimension. Since the solutions was observed to thicken with the stirring time (due to polymerisation, described in section 5.2.1), this may indicate that the film itself became less uniform due to formation of eumelanin lumps, increasing the surface roughness. However, over the entire image dimension spectrum, the roughness observed between the samples remained within a tight band between 0.7 – 1.5 nm.

Cu-eumelanin thin films fabricated above were homogenous and smooth, which means that the addition of Cu to eumelanin did not affect the film morphology relative to standard synthetic eumelanin thin films. Therefore, Cu-eumelanin thin films, like their eumelanin thin film counterparts, are viable to be used in devices.

5.2.5. Hydration dependent conductivity

In this section the DC conductivity experiments are described on Cu-eumelanin thin films that were fabricated on glass substrates. The samples were prepared as described in Chapter 2, Section 2.6. The Cu-eumelanin solutions were stirred for 1 min, 2 min, 3 min and 5 min for comparison. The source-drain electrodes were in a bottom contact geometry. Fabricated samples were placed within a vacuum-capable chamber, described in Chapter 2, Section 2.6.

The basic current-voltage (IV) characteristics required for determining the conductivity were obtained using an Agilent Semiconductor Device Analyzer B1500A. The voltage was swept forwards

and backwards from -1 to 1 V, with a hold time of 60 s and a scan rate of 1 point per second. The experimental procedure including the hydration steps used in this experiment was the same as described in Chapter 2, Section 2.6.

Presented in Figure 5.6, is an example set of an IV data for a thin Cu-eumelanin film, stirred for 2 min, as a function of water vapour pressure. The remaining data, obtained at different solution stirring times can be found in the Appendix, Figure S5.3. It is clear from Figure 5.6 that the current increases as a function of hydration. Furthermore, similar to the neat eumelanin thin films, there is hysteresis between the forward and backward sweeps, which is an indication of capacitive effects. This is predictable, given that Cu-eumelanin (as for eumelanin) conducts protons, which tend to exhibit capacitive behaviour due to their slow motion and inability to be extracted at blocking electrical electrodes.

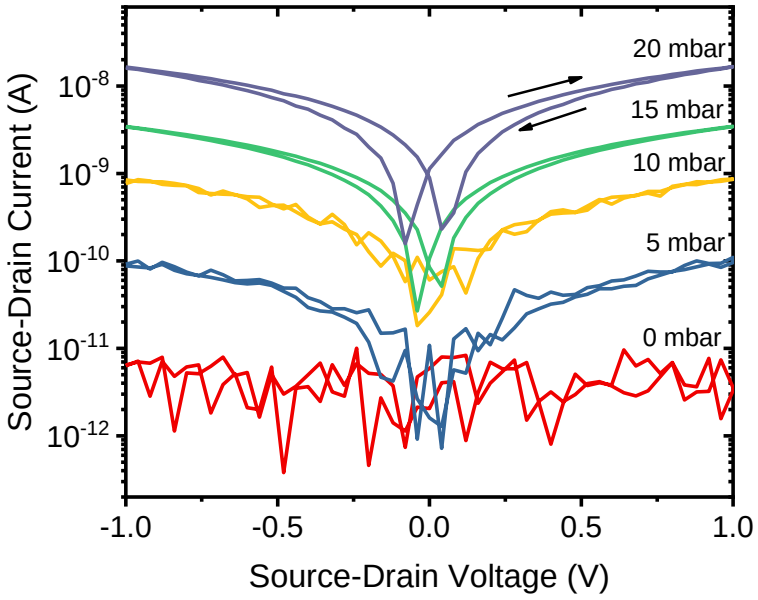

Figure 5.6. Source-drain current as a function of voltage for a Cu-eumelanin thin film (2 min stirring time). Each IV measurement was taken at different water vapour pressures, which are indicated. Each curve is an average of three measurements.

The obtained IV data was normalised to create a conductivity plot (Figure 5.7). The data represented on the graph is the calculated conductivity as a function of hydration for Cu-eumelanin thin films with different thicknesses and a comparative eumelanin thin film set. Each data point on the graph represents measurements taken from three different samples. The standard errors were propagated from the random uncertainty determined from the IV data sets and the overall error was calculated (2SE across multiple samples).

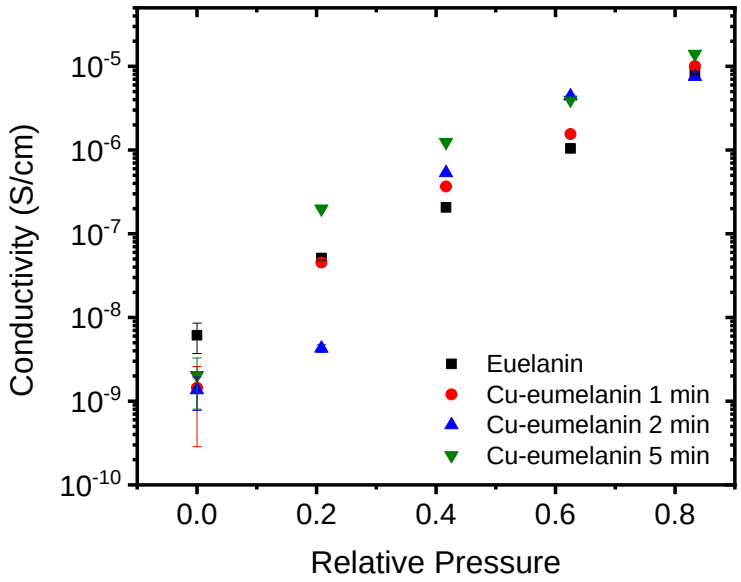

Figure 5.7. Eumelanin and Cu-eumelanin conductivity as a function of relative pressure of water vapour. The error has been calculated and is presented on the graph, however for some data points the bars are smaller than the actual data point resolution. Uncertainties were calculated to 2 times the standard error.

The graph is plotted in a way to show the comparison between eumelanin thin film conductivity and Cu-eumelanin conductivity. It can be seen that in both cases the conductivity increases exponentially with increase of the relative pressure of the surrounding water vapour. However, Cu-eumelanin samples fabricated from the solution stirred for 5 min have the highest conductivity values. This accords with both the comproportionation reaction prediction and the observation from the XPS data that shows that with increasing the stirring time the concentration of Cu in the film increases. Similarly, Cu-eumelanin solution stirred for 1 min yields the lowest conductivity of all due to the lowest amount of copper in the film.

Thus far, the observations that have been made about Cu-eumelanin conductivity are in line with the prediction that the comproportionation reaction is being perturbed such as to generate more protons for conduction. However, thus far the evidence presented does not demonstrate that the conductivity is indeed due to an increase in proton charge density. To do so, an experiment is required which shows that a larger number of protons are present. To this end, a Cu-eumelanin-based OECT was fabricated, and it is the subject for the next section. Since the OECT switching mechanism depends on mobile protons, the Cu-eumelanin OECT should deliver enhanced performance.

5.3. Cu-eumelanin based OECTs

5.3.1. Device fabrication

Glass slides (14.9 mm x 14.9 mm) were cleaned as described in Chapter 2. Source and drain electrodes, PEDOT:PSS film and HMDS layer were deposited as presented in Chapter 4 with the same material thicknesses, Section 4.2. The Cu-eumelanin solution used in these measurements was prepared as highlighted above and stirred for 2 min, as it was found to be the optimal time in terms of solution viscosity (see Section 5.2.1) and film thickness. A 0.45µm hydrophobic filter was used to spin-coat Cu-eumelanin solution at 1500 rpm for 60 s. Finally, a 30 nm Au top gate contact was thermally evaporated. All thicknesses were measured using a Dektak XT. Each sample consisted of 3 transistors with multiple samples fabricated for each type of experiment, as per the process in Chapter 4, Section 4.2.

5.3.2. Electrical characterisation under ambient conditions

The electrical characteristics of the Cu-eumelanin OECT devices were measured using a probe-station and an Agilent Semiconductor Device Analyser (B1500A). Transfer curves were measured with V_d at 100 mV and V_g sweeping from -1 V to 1 V. The hold time for all measurements was 60 s and the delay time was 1 s. All transfer and output curves were measured slowly enough to allow steady state to be reached (see Chapter 4, Section 4.3). The measurements were performed under ambient conditions. These ambient laboratory conditions provided enough natural moisture to render the eumelanin "conducting", i.e. sufficient water to facilitate proton percolation [66] and hence test the solid-state gating concept. Transfer and Output curves are presented in Figure 5.8.

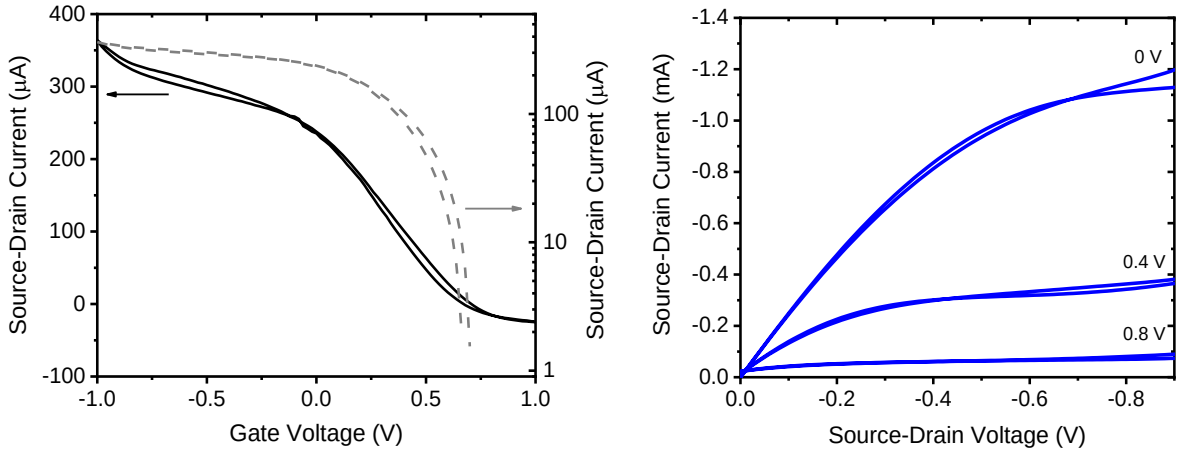

Figure 5.8. (a) An example transistor transfer characteristic of a PEDOT:PSS channel (100 nm thick film, 100 µm channel length) Cu-eumelanin top gate and gold gate electrode contact. Proton injection from the top gate de-dopes the PEDOT:PSS channel reducing the source–drain current. The dashed line represents the on/off ratio. (b) Transistor output characteristics. The device behaves as a p-type transistor and as would be expected for positive ion injection.

The transfer curve on Figure 5.8(a) shows that at zero gate voltage (V_g = 0 V) the transistor is in the "On" state with high current flowing through the channel (I_d). Upon application of a small positive gate voltage (~ 1 V), the transistor turns "Off". This behaviour is consistent with protons moving into the PEDOT:PSS, electrochemically de-doping and reducing the number density of free carriers available for conduction across the polymer backbone. Essentially, the behaviour is qualitatively the same as for the eumelanin OECTs in Chapter 4. The output characteristics in Figure 5.8(b) confirm *p*-type channel behaviour: in general, the relationship between I_d and V_d is almost linear for low V_d and all applied V_g, and with the application of larger negative V_d the current begins to saturate depending on V_g. In addition, Figure 5.8(b) shows almost complete channel turn-off with low gate voltages (<1.0 V). The transfer characteristics were obtained at V_d = 100 mV at a delay time of 1 s (1 data point per second).

From the above electrical characteristics obtained for a Cu-eumelanin OECT one can see a narrower hysteresis, higher on/off ratio and sharper curvatures than eumelanin-based devices (compare to data in Chapter 4). A significant increase in on/off ratio (about two orders of magnitude) at the same ambient laboratory conditions was observed for the Cu(II)-eumelanin OECTs. This suggests that incorporating copper-ions into eumelanin leads to the increase of the proton charge density in the film. For additional confirmation of the above inference, the channel transconductance (g_m) of the Cu-eumelanin based OECT was assessed. As previously discussed, transconductance is an important characteristic of a solid-state OECT device, since it is a measure of its sensitivity and the transistor switching voltage range. Figure 5.9 shows the transconductances derived from the transfer curves of the OECTs gated with eumelanin (black curve) and Cu-eumelanin (red curve) measured under ambient conditions.

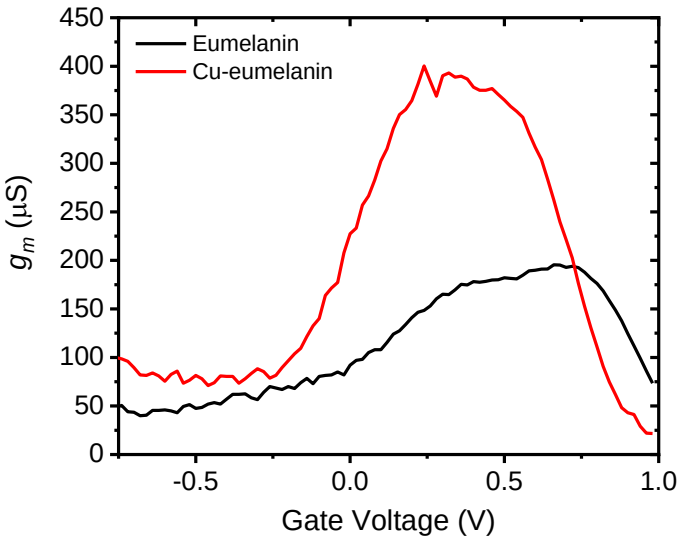

Figure 5.9. The corresponding transconductance (forward sweep) for eumelanin and Cu-eumelanin OECTs. The peak of transconductance for a Cu-eumelanin device is approximately 400 µS.

Table 5.2 presents key quantifiable parameters from Figure 5.9, enabling comparisons between eumelanin based OECTs and Cu-eumelanin OECTs. These parameters include the peak height relative to the baseline, peak width and peak position. As was discussed in detail in Chapter 4, the peak behaviour of the transconductance a) increases; b) narrows and c) shifts towards a lower gate voltage with an increase in the proton concentration of the eumelanin proton top gate.

Characteristic	**Eumelanin OECT**	**Cu-eumelanin OECT**
Baseline (μS)	50	80
Relative peak height (μS)	188	393
Peak width (V)	1.15	0.91
Peak position (V)	0.6	0.3

Table 5.2. Key characteristics of the transconductance for eumelanin and Cu-eumelanin OECTs.

From Table 5.2 it can be seen that the transconductance peak of the Cu-eumelanin based OECT is ~ x2 that for a neat eumelanin OECT and the voltage operating range narrows. Moreover, the peak position shifts even further to the negative gate voltage. This behaviour indicates an increase in proton charge density and validates the prediction made at the start that upon doping the eumelanin with Cu(II) one will increase the material's proton charge density.

It is important to note that the hydration dependent experiment was performed on Cu-eumelanin based OECTs. However, the devices experienced a contacting issue with the EGaIn and behaved differently to the standard eumelanin-based OECTs in that the EGaIn appeared not to wet the Cu-eumelanin properly. It appears that the surface energy of Cu-eumelanin thin films is different from neat eumelanin. In the research time remaining for the project, this issue could not be investigated. Hence, the Cu-eumelanin OECT study presented here should be viewed as preliminary.

5.4. Summary

Cu-eumelanin thin films were fabricated and characterised. AFM and XPS studies were undertaken and showed that the material was in fact eumelanin with copper chloride incorporated into it. Smooth and homogeneous films were obtained and used later in device fabrication. UV-Vis measurement showed that Cu-eumelanin possesses the same optical properties as eumelanin

regardless of the amount of Cu presented in the film. Conductivity measurements on Cu-eumelanin thin films showed that the electrical conductivity was hydration dependent and increased exponentially as a function of hydration. Moreover, higher conductivity values than for neat eumelanin films were obtained. A functional, all-solid-state organic electrochemical *p*-type transistor was demonstrated with substitution of eumelanin for Cu-eumelanin. On/off ratios of ~10^3 were achieved with low voltage operation (<1.0 V). These preliminary devices show a significant promise and require further investigation.

6. Conclusions

6.1. Summary

The Context

Bioelectronics is a growing field that lies at the intersection of physical, chemical and life sciences. The main challenge in creating such symbiosis is to find a way to put together electrical signals in biological systems, which are predominantly due to the flow of ions, and electrical signals in semiconductors, where the charge carriers are electronic. One of the most successful device architectures that enable this ion to electron transduction is the Organic Electrochemical Transistor (OECT), which are devices similar to organic field effect transistors (OFETs). The main differences between the two platforms are: 1) switching off the conductive channel in an OECT is via an electrochemical doping/de-doping process, which modulates the charge carrier density in the channel material. In contrast in an OFET channel switching is modulated due to the electric potential applied; 2) The gating mechanism in an OECT is volumetric, i.e. the ion capacitance of the entire volume of the channel is involved, as opposed to an OFET where the surface capacitance of the dielectric is the determining variable.

To date, the majority of the OECTs reported in literature, are liquid electrolyte based, which means that the gating is achieved via a liquid media. There are several problems associated with such an architecture including inability to miniaturization, integration and long-term stability. To overcome these challenges, a solid-state alternative is desirable. The main aim of the work described in this thesis was to demonstrate a functioning all-solid-state OECT based on a natural material, such as the pigment eumelanin. To this end, a thorough review of eumelanin as pertinent to its potential solid-state electrolyte capabilities was given. Furthermore, it was argued that PEDOT:PSS is a suitable candidate for the conductive channel material for these devices due to its availability, well known properties and preference for application in reported OECTs.

Eumelanin thin film characterisation

A first step in creating an all-solid-state device was a complete characterisation of the proposed gate material, eumelanin, in order to understand and optimise design and operation of the OECT. Eumelanin thin films were fabricated and characterised using a newly developed procedure. AFM and XPS studies were undertaken to ensure that the synthesised material was in fact eumelanin. The AFM indicated that smooth and homogeneous films were obtained. The ratio of atoms measured by XPS showed that the synthesised eumelanin mostly contained DHI moieties. UV-Vis absorption measurements showed that the synthesised eumelanin possessed the same optical properties as

standard melanin: broad-band monotonic, featureless absorption. Because eumelanin's conductivity is dependent on its hydration state, it is important to understand eumelanin's morphological behaviour in the presence of water. Neutron Reflectometry measurements showed that the eumelanin films swelled upon water absorption and that water is evenly distributed through the film. Further conductivity measurements on eumelanin thin films proved that the electrical conductivity was indeed hydration dependent and increased exponentially as a function of hydration. It should also be noted that DC current-voltage measures the capacitive displacement currents and extraction currents of small population of electrons. These findings were further used as a foundation for design and realisation of eumelanin-based bioelectronic devices.

AC and dielectric properties of eumelanin

After analysing eumelanin's hydration dependent DC conductivity, a natural question arises whether eumelanin's charge transport is dominated by ionic or electronic carriers. This question has been a matter of debate for several decades. One way to probe the nature of the dominant charge carrier in solid-state eumelanin is to use hydration controlled impedance measurements. In the AC measurements described in this thesis the data showed a systematic trend as a function of hydration. At low frequencies a characteristic diffusion tail was observed in the Nyquist plots which grew with increased water content. In contrast, the high frequency component was found to be virtually invariant. This is strongly suggestive that the main charge carrier in eumelanin is ionic in origin. A minimal equivalent circuit was developed to describe this behaviour, the salient features of which were a constant phase element, capturing dielectric double layer behaviour, and a resistor representing the ionic displacement current with a modified restricted diffusion element in series. All the Nyquist impedance plots fitted this circuit, and no combination of elements delivered a circuit containing an electronic component. The modelling therefore confirmed the dominant current component to be ionic (protonic), and the absence of an electronic contribution. Determination of the dielectric constant (real and imaginary parts) allowed the ionic conductivity to be estimated in the low frequency limit. Significant changes dry-to-wet of ~3 orders of magnitude were observed. An unexpected and interesting finding from these measurements was the high real part of the dielectric constant (~10^3) over a wide frequency range (20 to 10^4 Hz). These findings are significant since they strongly indicate that eumelanin is not a mixed hybrid electronic-ionic conductor as previously thought – but a proton transport material, and hence an ideal material for a solid state electrolyte in an OECT device.

Eumelanin-based OECT

Based on the knowledge obtained from the fabrication techniques and measurements described above, a functional, all-solid-state organic electrochemical *p*-type transistor was fabricated with a proton injecting top gate made from the conducting bio-macromolecule eumelanin. On/off ratios of ~10^4 were achieved with low voltage operation (<1.0 V) at high hydrations. It was also shown that such devices operate by "volumetric gating" – direct injection of protons into the semiconductor channel which modulates the channel current. Also, a generic transistor model was developed to test and explain its operation, which should in principle be broadly applicable to all OECT architectures by the inclusion of multiple volumetric capacitances. This simple all-solid-state architecture is amenable to miniaturization and a definitive step on the pathway to integrated bioelectronic logic.

Cu-eumelanin OECT

After developing the solid state organic electrochemical transistors, the next step was to improve device operating performance. Since eumelanin's conductivity is regulated by the comproportionation reaction, it was reasoned that the addition of transition metal ions could perturb the reaction to yield a higher proton charge density. To achieve higher proton charge densities, eumelanin was modified with a Copper II salt. Cu-eumelanin thin films were fabricated and characterised. AFM and XPS studies were undertaken and showed that the material was in fact eumelanin with copper chloride incorporated into it. Smooth and homogeneous films were obtained and used later in device fabrication. UV-Vis measurement showed that Cu-eumelanin possesses the same optical properties as eumelanin regardless of the amount of Cu present in the film. Conductivity measurements on Cu-eumelanin thin films showed that the electrical conductivity was hydration dependent and increased exponentially as a function of hydration. Moreover, higher conductivity values than for neat eumelanin films were obtained, showing that an increased Cu(II) content increased the conductivity. A functional, all-solid-state organic electrochemical *p*-type transistor was demonstrated with substitution of eumelanin for Cu-eumelanin. On/off ratios of ~10^3 were achieved with low voltage operation (<1.0 V). Hydration dependent experiments were performed on Cu-eumelanin based OECTs. However, the devices experienced a contacting issue with the EGaIn and behaved differently to the standard eumelanin-based OECTs. Therefore, the obtained results should be considered as preliminary and require further investigation.

6.2. Future outlook

The work described in this thesis opens multiple possibilities for further investigation and improvement of the existing solid state Organic Electrochemical Transistors. Some of these ideas will be described below.

Channel materials

One of the issues of the solid-state OECTs that needs to be addressed is the choice of the channel material. Although PEDOT:PSS is used widely due to its attractive properties and reasonable performance, these materials have some disadvantages and limitations. For example, the morphology of PEDOT:PSS is complex, which makes it difficult to be used as a model system for structure–function interactions [25]. In terms of electrical properties, the volumetric capacitance of the PEDOT:PSS film is affected by the bulky structure of PSS [165]. Furthermore, biocompatibility is an important characteristic that potential materials for OECTs should have, and even though PEDOT:PSS is found to be cytologically compatible [6], development of materials with more versatile properties is advantageous. When considering solution processing, which is an important component of creating an organic OECT, the acidity of PSS can also be a problem, as it may cause corrosion. The limitations of PEDOT:PSS as a material for OECTs, mentioned above motivate researchers to develop new materials.

There have been attempts at substituting the acidic PSS with polymers containing (trifluoromethylsulfonyl)imide side groups [166], which would produce OECTs similar in performance to those based on PEDOT:PSS. Another approach includes replacing PSS with ionic groups and attaching them directly to the thiophene backbone. The conjugated polymers synthesised this way can be semiconducting, when the ion is compensated by a counter ion or conducting, when the ion is compensated by an electronic charge. An example of using such materials for OECTs was an accumulation-mode OECT based on a polythiophene with a sulfonate group attached to its backbone (PTHS) [167]. A depletion-mode OECT has been developed utilising PEDOT modified with a pendant sulfonate group (PEDOT-S) [168]. An OECT that could be tuned by varying the stoichiometry of the channel can be created by mixing a semiconducting and a conducting conjugated polymers [168]. The creation of an accumulation mode OECT is preferable since it requires less power to operate. Currently, devices presented in this thesis are depletion mode, which is a disadvantage.

An alternative approach, which yields the covalent linkage of biological entities into the films without affecting the electrical properties, is mixing PEDOT:PSS with poly(vinyl alcohol) [169]. It has been shown that these polymer films can be functionalized with proteins that keep their biological activity. Electrochemical polymerization is a method that allows integration of biomolecules into

conducting polymers [170]. One of the first OECTs was fabricated using this method [149]. However, this approach has lost favour due to the difficulty of electrochemical deposition from a conducting surface of OECTs. Moreover, the strategy would not be suitable for the fabrication of the eumelanin-based OECTs described in this thesis, as growing biomolecules on the surface of the polymer would make it impossible to use eumelanin as a gate material.

An alternative method, vapour-phase polymerization, was proposed for the incorporation of biomolecules into the semiconducting channel. In this method, a conducting polymer PEDOT:TOS is fabricated by exposing a film cast from a precursor solution containing tosylate (TOS) to EDOT vapour [171]. High quality composites can be obtained by blending different polymers in the precursor solution. For example, blends of PEDOT:TOS with polyethylene glycol showed similar performance to PEDOT:TOS [172]. Furthermore, gelatin, which is the denatured form of collagen, can be incorporated into PEDOT:TOS without changing the electrochemical properties of the conducting polymer or the OECT performance [173]. These materials were shown to support adhesion and growth of bovine brain capillary endothelial cells *in vitro*. This technique could be potentially useful for designing flexible solid-state OECTs, where PEDOT:TOS would be used to improve adhesion on the substrate. The eumelanin deposition in this case should not be affected.

The materials discussed above are all *p*-type polymers. To further advance the field of bioelectronics in the direction of creating computational logic, the use of *n*-type materials is required. However, *n*-type polymers are difficult to obtain. Besides, making such polymers air and water stable is another challenging task. Nevertheless, some progress has been made in this class of materials recently. For example, a conjugated polymer with hydrophilic or ion-transporting side chains has been reported. It has been demonstrated that OECTs based on poly(2-(3,3´-bis(2-(2-(2-methoxyethoxy) ethoxy)ethoxy)-[2,2´-bithiophen]-5-yl)thieno[3,2-b] thiophene) p(g2T-TT) possess higher transconductances than those based on PEDOT:PSS [172]. An ambipolar OECT showing a high stability in liquid media during 2 hours measurements was fabricated using an *n*-type copolymer poly((ethoxy)ethyl 2-(2-(2-methoxyethoxy) ethoxy)acetate)-naphthalene-1,4,5,8-tetracarboxylicdiimide-co-3,3´-bis(2-(2-(2-methoxyethoxy)ethoxy) ethoxy)-(bithiophene)) p(gNDI-g2T) [175]. These polymers appear to be a promising avenue to expand the range of solid state OECT devices and the fields where OECTs can be used.

Proton transparent electrodes

Gold contacts used in the work presented here are known to be proton blocking electrodes, which to some extent affects the performance of the OECTs. One of the options to avoid this issue and possibly improve the device characteristics, is replacing Au with proton-transparent electrodes (for example, PdH_x). There are some examples of using palladium hydride (PdH_x) electrodes

available in the literature [82, 84]. As a metal, palladium serves as a good electronic conductor and can be used to measure electronic conductivity of different materials. Under exposure of H_2 Pd turns into PdH_x. PdH_x can transfer protons between the contacts and the desired material due to the reaction: $PdH \rightleftharpoons Pd + H^+ + e^-$. When a proton is injected into the material, an electron is collected, completing the circuit [84]. In liquid based OECTs metals are not used as the gate electrode since they accumulate a dielectric double layer. Usually this issue is overcome using an Ag/AgCl electrode [26, 151]. In the device architecture described in this thesis gold electrodes did not inject or extract protons from the device. Instead the ions in eumelanin formed a dielectric layer at the surface of the gold, reducing the effective electric field. Therefore, a proton injecting/extracting gate contact (such as PdH_x) would solve this problem and improve the transistor characteristics of the existing OECTs. The work described in literature used PdH_x contacts on eumelanin thin films, but not under the experimental conditions outlined in this thesis. A thorough investigation is needed to define and understand the change in eumelanin properties (including hydration dependent conductivity) in relation to PdH_x. Once this has been accomplished, PdH_x contacts can be implemented in a eumelanin-based OECT, which would provide more thorough understanding of proton transport in solid state OECTs.

Cu-melanin OECTs

Considering the experiments described above, it is clear that further work needs to be done to gain more understanding on the doped eumelanin characteristics. So far it was proven that incorporation of the transition metal ions into the eumelanin structure is possible and it can be advantageous for the OECT's performance. However, a complete hydration dependence experiment needs to be performed on such devices. Furthermore, no AC measurements have been performed to tease out the effects on the transport behaviour due to Cu(II) doping. Thus this should be a priority. Furthermore, thinking further afield, eumelanin can be doped with other metals to enhance the device characteristics, with potential candidates being Fe(II) and Fe(III), which are known to bind in large quantities, similar to Cu(II) to eumelanin [160].

Incorporation with biological materials

The ultimate goal of bioelectronics and the purpose of most existing solid-state OECTs is the interfacing with biological entities. Hence, the natural next step would be to perform an *in vitro* study, in which, for example, the gold electrodes would be replaced with electrically active cells (such as cardiomyocytes, neurons, receptors, etc.) to apply a potential to the device to affect its performance. Biological cells and tissues function in wet environment, which is why the vast majority of the literature available on the biological entities interfaced with OECTs describe the experiments, where

a liquid electrolyte is used as a gate in the device architecture [7, 9, 172, 176, 177]. Such devices are not compatible with a vision of solid-state organic electronics, hence new ways need to be found to interface biological samples. This will include a necessary study of cell culturing on eumelanin thin films, and then the culturing of cells on eumelanin based devices. The next complicated, but interesting task would be to create a device that would be stable and sensitive, keeping the cells active over long periods of time.

In summary, the work presented in this thesis is an advance in both, understanding the properties of eumelanin and its application to bioelectronics. This progress and the findings of the research point to many new avenues of enquiry both fundamental and applied.

References

1. Nikam, M., Singh, R. and Bhise, S., Organic Light Emitting Diodes: Future of Displays, in International Conference on Advances in Communication and Computing Technologies. 2012. p. 31-34.
2. Kalyani, N.T., Swart, H. and Dhoble, S.J., Principles and Applications of Organic Light Emitting Diodes (OLEDs). 2017: Woodhead Publishing. 332.
3. Meredith, P., et al., Electronic and optoelectronic materials and devices inspired by nature. Rep. Prog. Phys., 2013. 76: p. 034501.
4. Noy, A., Bionanoelectronics. Adv Mater, 2011. 23(7): p. 807-20.
5. Svennersten, K., et al., Organic bioelectronics in nanomedicine. Biochim Biophys Acta, 2011. 1810(3): p. 276-85.
6. Berggren, M. and Richter-Dahlfors, A., Organic Bioelectronics. Advanced Materials, 2007. 19: p. 3201–3213
7. Rivnay, J., Owens, R.M., and Malliaras, G.G., The Rise of Organic Bioelectronics. Chemistry of Materials, 2014. 26: p. 679–685.
8. Lin, P. and Yan, F., Organic Thin-Film Transistors for Chemical and Biological Sensing. Advanced Materials, 2012. 24: p. 34–51.
9. Owens, R.M. and Malliaras, G.G., Organic Electronics at the Interface with Biology. MRS Bulletin, 2011. 35: p. 449-456.
10. Xu, K., Nonaqueous liquid electrolytes for lithium-based rechargeable batteries. Chem Rev, 2004. 104(10): p. 4303-417.
11. Ratner, M.A. and Shriver, D.F., Ion-Transport in Solvent-Free Polymers. Chemical Reviews, 1988. 88(1): p. 109-124.
12. Mott, N.F. and Davis, E.A., Electronic processes in non-crystalline materials. 1979, Clarendon Press.
13. Miyake, T. and Rolandi, M., Grotthuss mechanisms: from proton transport in proton wires to bioprotonic devices. J. Phys.: Condens. Matter, 2016. 28: p. 023001.
14. Horowitz, G., Organic Field-Effect Transistors. Advanced Materials, 1999. 10: p. 365-377.
15. Tybrandt, K., et al., Ion bipolar junction transistors. Proceedings of the National Academy of Sciences of the United States of America, 2010. 107: p. 9929–9932.
16. Cui, Y., et al., Nanowire nanosensors for highly sensitive and selective detection of biological and chemical species. Science, 2001. 293: p. 1289-1292.

17. Misra, N., et al., Bioelectronic silicon nanowire devices using functional membrane proteins. Proceedings of the National Academy of Sciences of the United States of America, 2009. 106: p. 13780-13784.
18. Root, S.E., et al., Mechanical Properties of Organic Semiconductors for Stretchable, Highly Flexible, and Mechanically Robust Electronics. Chem Rev, 2017. 117(9): p. 6467-6499.
19. Simon, D.T., et al., Organic Bioelectronics: Bridging the Signaling Gap between Biology and Technology. Chem Rev, 2016. 116(21): p. 13009-13041.
20. Safarikova, E., et al., Evaluation and improvement of organic semiconductors' biocompatibility towards fibroblasts and cardiomyocytes. Sensors and Actuators B-Chemical, 2018. 260: p. 418-425.
21. Lei, T., et al., Biocompatible and totally disintegrable semiconducting polymer for ultrathin and ultralightweight transient electronics. Proceedings of the National Academy of Sciences of the United States of America, 2017. 114(20): p. 5107-5112.
22. Sytnyk, M., et al., Cellular interfaces with hydrogen-bonded organic semiconductor hierarchical nanocrystals. Nature Communications, 2017. 8.
23. Fang, Y., Li, X. M., and Fang, Y., Organic bioelectronics for neural interfaces. Journal of Materials Chemistry C, 2015. 3(25): p. 6424-6430.
24. Bassler, H. and Kohler, A., Charge Transport in Organic Semiconductors. Top Curr Chem, 2012. 312: p. 1-66.
25. Rivnay, J., et al., Organic electrochemical transistors. Nature Reviews Materials, 2018. 3(2).
26. Khodagholy, D., et al., High transconductance organic electrochemical transistors. Nat Commun, 2013. 4: p. 2133.
27. Rivnay, J., et al., High-performance transistors for bioelectronics through tuning of channel thickness. Science Advances, 2015. 1(4).
28. Strakosas, X., Bongo, M., and Owens, R.M., The organic electrochemical transistor for biological applications. Journal of Applied Polymer Science, 2015. 132(15).
29. Nilsson, D., et al., Electrochemical logic circuits. Advanced Materials, 2005. 17(3): p. 353-+.
30. Hutter, P.C., et al., All Screen-Printed Logic Gates Based on Organic Electrochemical Transistors. Ieee Transactions on Electron Devices, 2015. 62(12): p. 4225-4230.
31. Bernards, D.A. and Malliaras, G.G., Steady-State and Transient Behavior of Organic Electrochemical Transistors. Advanced Functional Materials, 2007. 17(17): p. 3538-3544.
32. Carrad, D.J., et al., Hybrid Nanowire Ion-to-Electron Transducers for Integrated Bioelectronic Circuitry. Nano Lett, 2017. 17(2): p. 827-833.
33. Strukov, D.B., et al., The missing memristor found. Nature, 2008. 453(7191): p. 80-83.

34. Gadjourova, Z., et al., Ionic conductivity in crystalline polymer electrolytes. Nature, 2001. 412(6846): p. 520-523.
35. Angell, C.A., Liu, C. and Sanchez, E., Rubbery Solid Electrolytes with Dominant Cationic Transport and High Ambient Conductivity. Nature, 1993. 362(6416): p. 137-139.
36. Hickner, M.A., Ion-containing polymers: new energy & clean water. Materials Today, 2010. 13: p. 34-41.
37. Rikukawa, M. and Sanui, K., Proton-conducting polymer electrolyte membranes based on hydrocarbon polymers. Progress in Polymer Science, 2000. 25: p. 1463±1502.
38. Bernards, D.A., et al., Enzymatic sensing with organic electrochemical transistors. Journal of Materials Chemistry, 2008. 18: p. 116-120.
39. Lin, P., et al., Organic electrochemical transistors integrated in flexible microfluidic systems and used for label-free DNA sensing. Advanced Materials, 2011. 23: p. 4035-4040.
40. Kim, D., et al., Organic electrochemical transistor based immunosensor for prostate specific antigen (PSA) detection using gold nanoparticles for signal amplification. Biosensors and Bioelectronics, 2010. 25: p. 2477–2482.
41. Leleux, P., et al., Organic electrochemical transistors for clinical applications. Advanced Healthcare Materials, 2015. 4: p. 142-147.
42. Khodagholy, D., et al., Organic electrochemical transistor incorporating an ionogel as a solid state electrolyte for lactate sensing. J. Mater. Chem. , 2012. 22: p. 4440–4443.
43. Nilsson, D., et al., An all-organic sensor-transistor based on a novel electrochemical transducer concept printed electrochemical sensors on paper. Sens. Actuators B Chem. Sci., 2002. 86: p. 193–197.
44. Tarabella, G., et al., Effect of the gate electrode on the response of organic electrochemical transistors. Appl. Phys. Lett., 2010. 97: p. 123304.
45. Tang, H., et al., Highly sensitive dopamine biosensors based on organic electrochemical transistors. Biosensors and Bioelectronics, 2011. 26.
46. Aristotle, The History of Animals, Book IX: Of the habits of the fishing-frog, of the torpedo, and of other fishes; and of the sepia and the argonaut. 315 B.C.
47. Meredith, P. and Sarna, T., The physical and chemical properties of eumelanin. Pigment Cell Res, 2006. 19(6): p. 572-94.
48. Prota, G., Melanins and Melanogenesis. 1992: Academic Press. 290.
49. Gottesberge, A.M.M., Physiology and Pathophysiology of Inner Ear Melanin. Pigment Cell Melanoma Res., 1988. 1: p. 238-249.
50. Zucca, F.A., et al., The neuromelanin of human substantia negra: Physiological pathological states. Pigment Cell Res., 2004. 17: p. 610-617.

51. Ito, S. and Wakamatsu, K., Quantitative analysis of eumelanin and pheomelanin in humans, mice, and other animals: A comparative review. Pigment Cell Res., 2003. 2003: p. 523-531.
52. Sansinenea, E. and Ortiz, A., Melanin: a photoprotection for Bacillus thuringiensis based biopesticides. Biotechnol. Lett., 2015. 37: p. 483–490.
53. Greco, G., et al., Uncovering the structure of human red hair pheomelanin: benzothiazolylthiazinodihydroisoquinolines as key building blocks. Journal of Natural Products, 2011. 74: p. 675–682.
54. Langfelder, K., et al., Biosynthesis of fungal melanins and their importance for human pathogenic fungi. Fungal Genet. Biol., 2003. 38: p. 143-158.
55. Kim, Y.J. and Uyama, H., Tyrosinase inhibitors from natural and synthetic sources: structure, inhibition mechanism and perspective for the future. Cellular and Molecular Life Sciences, 2005. 62: p. 1707–1723.
56. Bush, W.D., et al., The surface oxidation potential of human neuromelanin reveals a spherical architecture with a pheomelanin core and a eumelanin surface. Proc Natl Acad Sci U S A, 2006. 103(40): p. 14785-9.
57. Fedorow, H., et al., Neuromelanin in human dopamine neurons: comparison with peripheral melanins and relevance to Parkinson's disease. Prog Neurobiol., 2005. 75: p. 109–124.
58. Hamilton, A.J. and Gomez, B.L., Melanins in fungal pathogens. Journal of Medical Microbiology, 2002. 51: p. 189–191.
59. Bókony, V., et al., Melanin-based plumage coloration and flight displays in plovers and allies. Proc. Biol. Sci., 2003. 270: p. 2491–2497.
60. Nappi, A.J. and Christensen, B.M., Melanogenesis and associated cytotoxic reactions: applications to insect innate immunity. Insect Biochem. Mol. Biol., 2005. 35: p. 443–459.
61. Manvelyan, L.R., Gevorkyan, O.V., and Petrosyan, T.P., Recovery of instrumental conditioned reflexes in rats after pyramidotomy and action of bacterial melanin. J. Evol. Biochem. Physiol., 2008. 44: p. 316–321.
62. Petrosyan, T.R., Bacterial melanin favors regeneration after motor tract and peripheral nerve damage. J. Sci. Technol., 2013. 1: p. 1-6.
63. Gallas, J.M., Optical lens system incorporating melanin as an absorbing pigment for protection against electromagnetic radiation, U.S. Patent, Editor. 1991, Photoprotective Technologies Inc Unated States of America.
64. Pawelek, J.M. and Platt, J.T., Cosmetic melanins, U.S. Patent, Editor. 1998, Yale University: Unated States of America.
65. Blois, M.S., Zahlan, A.B., and Maling, J.E., Electron spin resonance studies on melanin. Biophys. J., 1964. 4: p. 471-490.

66. Mostert, A.B., et al., Role of semiconductivity and ion transport in the electrical conduction of melanin. Proc Natl Acad Sci U S A, 2012. 109(23): p. 8943-7.
67. Blois, M.S., The Melanins: Their Synthesis and Structure. Photochem. Photobiol., 1978. 3: p. 115-134.
68. Hill, H.Z., Li, W., and Mitchell, D.L., Melanin: a two edge sword? Pigment Cell Res., 1997. 3: p. 158-161.
69. Sarna, T., New trends in photobiology: Properties and function of the ocular melanin — a photobiophysical view. J. Photochem. Photobiol. B: Biol., 1992. 12: p. 215-258.
70. Bothma, J.P., et al., Device-Quality Electrically Conducting Melanin Thin Films. Advanced Materials, 2008. 20(18): p. 3539-3542.
71. Watt, A.R., Bothma, J.P., and Meredith, P., The supramolecular structure of melanin. Soft Matter, 2009. 5(19): p. 3754.
72. Pawelek, J., Osber, M.P., and Orlow, S.J., Synthetic melanin, U. Patent, Editor. 1993. p. 459.
73. Plonka, P.M. and Grabacka, M., Melanin synthesis in microorganisms-biotechnological and medical aspects. Acta Biochim. Pol., 2006. 53: p. 429–443.
74. Matamá, T., Gomes, A.C., and Cavaco-Paulo, A., Hair coloration by gene regulation: fact or fiction? Trends in Biotechnology, 2015. 33: p. 707-711.
75. Wolbarsht, M.L., Walsh, A.W., and George, G., Melanin, a unique biological absorber. Appl Opt, 1981. 20(13): p. 2184-6.
76. Riesz, J., Gilmore, J., and Meredith, P., Quantitative scattering of melanin solutions. Biophys J, 2006. 90(11): p. 4137-44.
77. Tran, M.L., Powell, B.J., and Meredith, P., Chemical and structural disorder in eumelanins: A possible explanation for broadband absorbance. Biophysical Journal, 2006. 90(3): p. 743-752.
78. Meredith, P., et al., Towards structure-property-function relationships for eumelanin. Soft Matter, 2006. 2(1): p. 37-44.
79. McGinness, J., Corry, P., and Proctor, P., Amorphous semiconductor switching in melanins. Science, 1974. 183: p. 853-855.
80. Rosenberg, B. and Postow, E., Semiconduction in proteins and lipids - its possible biological import. Ann. N. Y. Acad. Sci., 1969. 158: p. 158-162.
81. Mostert, B.A., et al., On the origin of electrical conductivity in the bio-electronic material melanin. Applied Physics Letters, 2012. 100(9): p. 093701.
82. Zhong, C., et al., A polysaccharide bioprotonic field-effect transistor. Nat Commun, 2011. 2: p. 476.

83. Ordinario, D.D., et al., Bulk protonic conductivity in a cephalopod structural protein. Nat Chem, 2014. 6(7): p. 596-602.
84. Wünsche, J., et al., Protonic and Electronic Transport in Hydrated Thin Films of the Pigment Eumelanin. Chemistry of Materials, 2015. 27(2): p. 436-442.
85. Larsson, B. and Tjalve, H., Studies on melanin-affinity of metal ions. Acta Physiol. Scand., 1978. 104: p. 479-484.
86. Kaczara, P., et al., Melanosome-iron interactions within retinal pigment epithelium-derived cells. Pigment Cell Melanoma Res., 2012. 25: p. 804-814.
87. Zecca, L., et al., Interaction of neuromelanin and iron in substantia nigra and other areas of human brain. Neuroscience, 1996. 73: p. 407-415.
88. Larsson, B.S., Interactions between chemicals and melanin. Pigment Cell Melanoma Res., 1993. 6: p. 127-133.
89. Araujo, M., Natural melanin: A potential pH-responsive drug release device. Int. J. Pharm., 2014. 469: p. 140-145.
90. Enochs, W.S., Paramagnetic metal scavenging by melanin: MR imaging. Radiology, 1997. 204: p. 417-423.
91. Mann, D.M.A. and Yates, P.O., Possible role of neuromelanin in the pathogenesis of Parkinson's disease. Mech. Age. Dev., 1983. 21: p. 193-203.
92. Pal, A., et al., Towards a Unified Vision of Copper Involvement in Alzheimer's Disease: A Review Connecting Basic, Experimental, and Clinical Research. J. Alzheimers Dis., 2015. 44: p. 343-354.
93. Otsuka, S. and Yamanaka, T., Metalloproteins: Chemical Properties and Biological Effects in Bioactive Molecules, in Elsevier. 1988.
94. Palumbo, A., et al., Effect of metal ions on the rearrangement of dopachrome. Biochim. Biophys. Acta, 1987. 925: p. 203-209.
95. Chodurek, E., et al., Effect of Cu 2+ and Zn 2+ ions on DOPA-melanin structure as analyzed by pyrolysis–gas chromatography–mass spectrometry and EPR spectroscopy. J. Anal. Appl. Pyrolysis, 2003. 70: p. 43-54.
96. Jastrzebska, M., Kocot, A., and Tajber, L., Photoconductivity of synthetic dopa-melanin polymer. Photochem. Photobiol., 2002. 66: p. 201-206.
97. Jastrzebska, M.M., et al., Effect of Cu^{2+} -ions on semiconductor properties of synthetic DOPA melanin polymer. Journal of Biomaterials Science Polymer Ed, 1996. 7: p. 781-793.
98. Bässler, H., Charge Transport in Disordered Organic Photoconductors a Monte Carlo Simulation Study. Phys. Stat. Sol. (b), 1993. 175: p. 15-56.

99. Houili, H., et al., Investigation of the charge transport through disordered organic molecular heterojunctions. Journal of Applied Physics, 2006. 100: p. 033702.
100. Sheliakina, M., Mostert, A.B., and Meredith, P., An all-solid-state biocompatible ion-to-electron transducer for bioelectronics. Materials Horizons, 2018. 5(2): p. 256-263.
101. Roseman, J.M., et al., Hybrid integrated biological-solid-state system powered with adenosine triphosphate. Nat Commun, 2015. 6: p. 10070.
102. Najafi, K., Integrated Sensors in Biological Environments. Sensors and Actuators B-Chemical, 1990. 1(1-6): p. 453-459.
103. Chiang, C.K., et al., Synthesis of highly conducting films of derivatives of polyacetylene, (CH)x. J. Am. Chem. Soc., 1978. 100: p. 1013-1015.
104. Felix, C.C., et al., Interactions of melanin with metal ions. Electron spin resonance evidence for chelate complexes of metal ions with free radicals. Journal of the American Chemical Society, 1978. 100: p. 3922-3926
105. da Silva, M.I.N., et al., Synthetic melanin thin films: Structural and electrical properties. Journal of Applied Physics, 2004. 96: p. 5803-5807.
106. Wünsche, J., et al., Eumelanin thin films: solution-processing, growth, and charge transport properties. Journal of Materials Chemistry B, 2013. 1(31): p. 3836.
107. Abbas, M., et al., Structural, electrical, electronic and optical properties of melanin films. Eur Phys J E Soft Matter, 2009. 28(3): p. 285-91.
108. da Silva, M.P., et al., Melanin as an active layer in biosensors. Aip Advances, 2014. 4(3).
109. Salomaki, M., et al., Preparation of Thin Melanin-Type Films by Surface-Controlled Oxidation. Langmuir, 2016. 32: p. 4103−4112.
110. Bronze-Uhle, E.S., et al., Synthesis of water-soluble melanin. arXiv e-print 2015: p. 23.
111. Beamson, G. and Briggs, D., High Resolution XPS of Organic Polymers: The Scienta ESCA300 Database. Journal of Chemical Education, 1993. 70: p. 25.
112. Mostert, A.B., et al., Gaseous adsorption in melanins: hydrophilic biomacromolecules with high electrical conductivities. Langmuir, 2010. 26(1): p. 412-6.
113. Rienecker, S.B., et al., Heavy Water as a Probe of the Free Radical Nature and Electrical Conductivity of Melanin. J Phys Chem B, 2015. 119(48): p. 14994-5000.
114. Penfoldt, J. and Thomas, R.K., The application of the specular reflection of neutrons to the study of surfaces and interfaces. J. Phys.: Condens. Matter., 1990. 2: p. 1369-1412.
115. Caluwe, S.C.D., et al., Phase segregation of sulfonate groups in Nafion interface lamellae, quantified via neutron reflectometry fitting techniques for multi-layered structures. Soft Matter, 2014. 10: p. 5763–5776.

116. Russell, T.P., X-ray and neutron reflectivity for the investigation of polymers. Materials Science Reports, 1990. 5: p. 171-271.
117. Sears, V.F., Neutron scattering lengths and cross section. Neutron News, 1992. 3: p. 26-37.
118. Nelson, A., Co-refinement of multiple-contrast neutron/X-ray reflectivity data using MOTOFIT. Journal of Applied Crystallography, 2006. 39: p. 273–279.
119. Nelson, A., et al., X-ray and neutron reflectometry study of glow-discharge plasma polymer films. Langmuir, 2005(22): p. 112-123.
120. James, M., et al., The multipurpose time-of-flight neutron reflectometer "Platypus" at Australia's OPAL reactor. Nuclear Instruments and Methods in Physics Research Section A, 2011. 632: p. 112-123.
121. Harvey, A.H. and Lemmon, E.W., Correlation for the vapor pressure of heavy water from the triple point to the critical point. Journal of Physical and Chemical Reference Data, 2002. 31: p. 173.
122. Nelson, A., Motofit – integrating neutron reflectometry acquisition, reduction and analysis into one, easy to use, package. Journal of Physics: Conference Series, 2010. 251.
123. Szent-Gyorgyi, A., Towards a New Biochemistry. Science, 1941. 93: p. 609-61 1.
124. Rosenberg, B., Electrical Conductivity of Proteins .2. Semiconduction in Crystalline Bovine Hemoglobin. Journal of Chemical Physics, 1962. 36(3): p. 816-&.
125. Glasser, L., Proton conduction and injection in solids. Chemical Reviews, 1975. 75: p. 21-65.
126. Morgan, H., Pethigt, R., and Stevens, G.T., A proton-injecting technique for the measurement of hydration dependent protonic conductivity. J. Phys. E: Sci. Instrum., 1986. 19: p. 80-82.
127. Carmo, M., et al., A comprehensive review on PEM water electrolysis. International Journal of Hydrogen Energy, 2013. 38: p. 4901-4934.
128. de Levie, R., The electrolysis of water. Journal of Electroanalytical Chemistry, 1999. 476: p. 92–93.
129. Clulow, A.J., et al., The structural impact of water sorption on device-quality melanin thin films. Soft Matter, 2017. 13(21): p. 3954-3965.
130. Powell, M.R. and Rosenberg, B., The Nature of the Charge Carriers in Solvated Biomacromolecules. Bioenergetics, 1970. 1: p. 493-509.
131. Wu, T.-F., Wee, B.-H., and Hong, J.-D., An Ultrasensitive and Fast Moisture Sensor Based on Self-Assembled Dopamine-Melanin Thin Films. Advanced Materials Interfaces, 2015. 2(15): p. 1500203.
132. Son, E.J., et al., Quinone and its derivatives for energy harvesting and storage materials. Journal of Materials Chemistry A, 2016. 4(29): p. 11179-11202.

133. Della Vecchia, N.F., et al., Tailoring melanins for bioelectronics: polycysteinyldopamine as an ion conducting redox-responsive polydopamine variant for pro-oxidant thin films. Journal of Materials Chemistry C, 2015. 3(25): p. 6525-6531.
134. Tarabella, G., et al., A hybrid living/organic electrochemical transistor based on the Physarum polycephalum cell endowed with both sensing and memristive properties. Chem Sci, 2015. 6(5): p. 2859-2868.
135. Khafaji, M., Shahrokhian, S., and Ghalkhani, M., Electrochemistry of levo-thyroxin on edgeplane pyrolytic graphite electrode: application to sensitive analytical determinations. Electroanalysis, 2011. 23: p. 1875–1880.
136. Fischer, J., Dejmkova, H., and Barek, J., Electrochemistry of pesticides and its analytical applications. Current Organic Chemistry, 2011. 15: p. 2923–2935.
137. Vidal, C.V. and Muñoz, A.I., Effect of physico-chemical properties of simulated body fluids on the electrochemical behaviour of CoCrMo alloy. Electrochimica Acta, 2011. 56: p. 8239–8248.
138. Wolner, C., Nauer, G.E., and Trummer, J., Possible reasons for the unexpected bad biocompatibility of metal-on-metal hip implants. Materials Science and Engineering, 2006. 26: p. 34–40.
139. Xhoffer, C., Van de Bergh, K., and Dillen, H., Electrochemistry: a powerful analytical tool in steel research. Electrochimica Acta, 2004. 49: p. 2825–2831.
140. Barsoukov, E. and Macdonald, J.R., Impedance Spectroscopy: Theory, Experiment, and Applications. 2005: John Wiley & Sons. 608.
141. Bisquert, J. and Fabregat-Santiago, F., Impedance Spectroscopy: A General Introduction and Application to Dye-Sensitized Solar Cells. 2010.
142. Macdonald, J.R., Impedance speciroscopy and its use in analyzing the steady-state ac response of solid and liquid electrolytes J. Eleciroanal. Chem., 1987. 223: p. 25-50
143. Zia, A.I. and Mukhopadhyay, S.C., Chapter 2. Impedance Spectroscopy and Experimental Setup. Electrochemical Sensing: Carcinogens in Beverages. Vol. 20. 2016, Smart Sensors, Measurement and Instrumentation: Springer International Publishing Switzerland.
144. Barsoukov, E. and Macdonald, J.R., Impedance Spectroscopy: Theory, Experiment, and Applications. 3 ed, ed. J.R. MacDonald. 2005: John Wiley & Sons, Inc.
145. Mayer, J., Khairy, K., and Howard, J., Drawing an elephant with four complex parameters. American Journal of Physics, 2010. 78(6): p. 648-649.
146. Floudas, G., Polymer Science: A Comprehensive Reference. Elsevier B.V., ed. T. Hashimoto, H.W. Spiess, and M. Takenaka. Vol. 2. 2012.

147. Kim, Y.J., et al., Biologically derived melanin electrodes in aqueous sodium-ion energy storage devices. Proceedings of the National Academy of Sciences USA, 2013. 110: p. 20912–20917.
148. Ishai, P.B., et al., Electrode polarization in dielectric measurements: a review. Measurement Science and Technology, 2013. 24: p. 102001.
149. White, H.S., Kittlesen, G.P., and Wrighton, M.S., Chemical derivatization of an array of three gold microelectrodes with polypyrrole: fabrication of a molecule-based transistor. Journal of American Chemical Society, 1984. 106: p. 5375–5377.
150. Nikolou, M. and Malliaras, G.G., Applications of poly (3,4-ethylenedioxythiophene) doped with poly(styrene sulfonic acid) transistors in chemical and biological sensors. Chemical Record, 2008. 8(1): p. 13-22.
151. Bernards, D.A., et al., Gating of an organic transistor through a bilayer lipid membrane with ion channels. Applied Physics Letters, 2006. 89: p. 053505-1-3.
152. Lin, P., Yan, F., and Chan, H.L.W., Ion-Sensitive Properties of Organic Electrochemical Transistors. Applied Materials and Interfases, 2010. 2: p. 1637–1641.
153. Kim, S.H., et al., Electrolyte-Gated Transistors for Organic and Printed Electronics. Advanced Materials, 2013. 25(13): p. 1822-1846.
154. van de Burgt, Y., et al., A non-volatile organic electrochemical device as a low-voltage artificial synapse for neuromorphic computing. Nat Mater, 2017. 16(4): p. 414-418.
155. Volkov, A.V, et al., Understanding the capacitance of PEDOT:PSS. Adv. Func. Mater, 2017. 27(28).
156. Kurra, N., et al., A conducting polymer nucleation scheme for efficient solid-state supercapacitors on paper. J. Mater. Chem. A, 2014. 2.
157. Kumar, P., et al., Melanin-based flexible supercapacitors. Journal of Materials Chemistry C, 2016. 4(40): p. 9516-9525.
158. Braendlein, M., et al., Voltage Amplifier Based on Organic Electrochemical Transistor. Adv Sci (Weinh), 2017. 4(1): p. 1600247.
159. Rivnay, J., et al., Organic electrochemical transistors with maximum transconductance at zero gate bias. Adv Mater, 2013. 25(48): p. 7010-4.
160. Hong, L. and Simon, J.D., Current understanding of the binding sites, capacity, affnity, and biological significance of metals in melanin. Journal of Physical Chemistry B, 2007. 111: p. 7938-7947.
161. Froncisz, W., Sarna, T., and Hyde, J.S., Cu2+ probe of metal-ion binding sites in melanin using electron paramagnetic resonance spectroscopy. I. Synthetic melanins. Arch Biochem Biophys, 1980. 202(1): p. 289-303.

162. Szpoganicz, B., et al., Metal binding by melanins: studies of colloidal dihydroxyindole-melanin, and its complexation by Cu(II) and Zn(II) ions. Journal of Inorganic Biochemistry, 2002. 89: p. 45-53.
163. Gidanian, S. and Farmer, P.J., Redox behavior of melanins: direct electrochemistry of dihydroxyindole-melanin and its Cu and Zn adducts. Journal of Inorganic Biochemistry, 2002. 89: p. 54-60.
164. Rienecker, S., Opto-Electronic Properties of Melanin: Solid-State Characterisation via EPR, Conductivity, and Copper Chelation, in School of Chemistry and Molecular Biosciences. 2017, The University of Queensland.
165. Proctor, C.M., Rivnay, J., and Malliaras, G.G., Understanding volumetric capacitance in conducting polymers. J. Polym. Sci. Part B Polym. Phys., 2016. 54: p. 1433–1436.
166. Inal, S., et al., Organic electrochemical transistors based on PEDOT with different anionic polyelectrolyte dopants. J. Polym. Sci. Part B Polym. Phys., 2015. 54: p. 147–151
167. Inal, S., et al., A high transconductance accumulation mode electrochemical transistor. Adv Mater, 2014. 26(44): p. 7450-5.
168. Zeglio, E., et al., Conjugated polyelectrolyte blends for electrochromic and electrochemical transistor devices. Chem. Mater., 2015. 27: p. 6385–6393.
169. Strakosas, X., et al., A facile biofunctionalisation route for solution processable conducting polymer devices. J. Mater. Chem. B, 2014. 2: p. 2537-2545.
170. Skotheim, T.A. and Reynolds, J., Handbook of Conducting Polymers. Conjugated Polymers: Processing and Applications. 2007: CRC Press. 1680.
171. Winther-Jensen, B. and West, K., Vapor-phase polymerization of 3,4-ethylenedioxythiophene: a routeto highly conducting polymer surface layers. Macromolecules, 2004. 37: p. 4538–4543
172. Jimison, L.H., et al., PEDOT:TOS with PEG: a biofunctional surface with improved electronic characteristics. J. Mater. Chem. , 2012. 22: p. 19498–19505.
173. Bongo, M., et al., PEDOT:gelatin composites mediate brain endothelial cell adhesion. J. Mater. Chem. B, 2013. 1: p. 3860-3867
174. Giovannitti, A., et al., Controlling the mode of operation of organic transistors through side-chain engineering. Proc Natl Acad Sci U S A, 2016. 113(43): p. 12017-12022.
175. Giovannitti, A., et al., N-type organic electrochemical transistors with stability in water. Nat Commun, 2016. 7: p. 13066.
176. Rivnay, J., et al., Organic electrochemical transistors for cell-based impedance sensing. Applied Physics Letters, 2015. 106(4).

177. Curto, V.F., et al., Organic transistor platform with integrated microfluidics for in-line multi-parametric in vitro cell monitoring. Microsystems & Nanoengineering, 2017. 3.

Appendix

Figures

Chapter 2

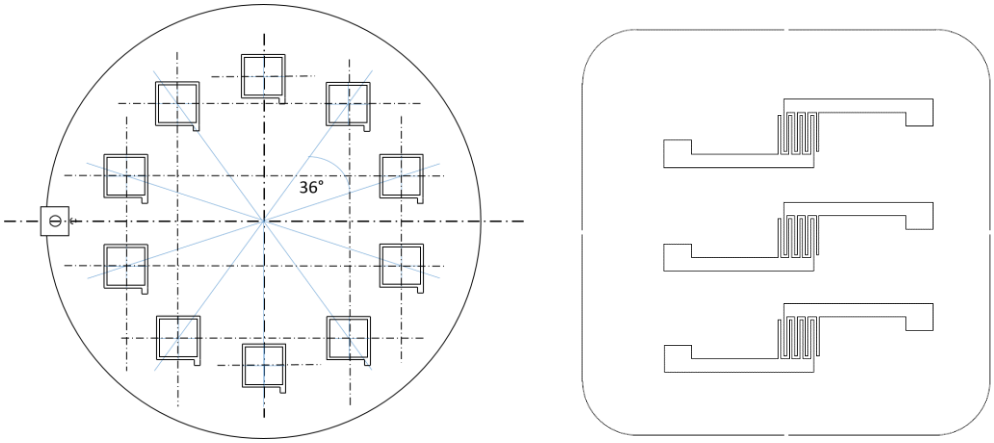

Figure S2.1. The schematic of the evaporation plate (left) and electrodes on the glass substrate (right). The channel length and width are 100 µm and 11.2 mm respectively.

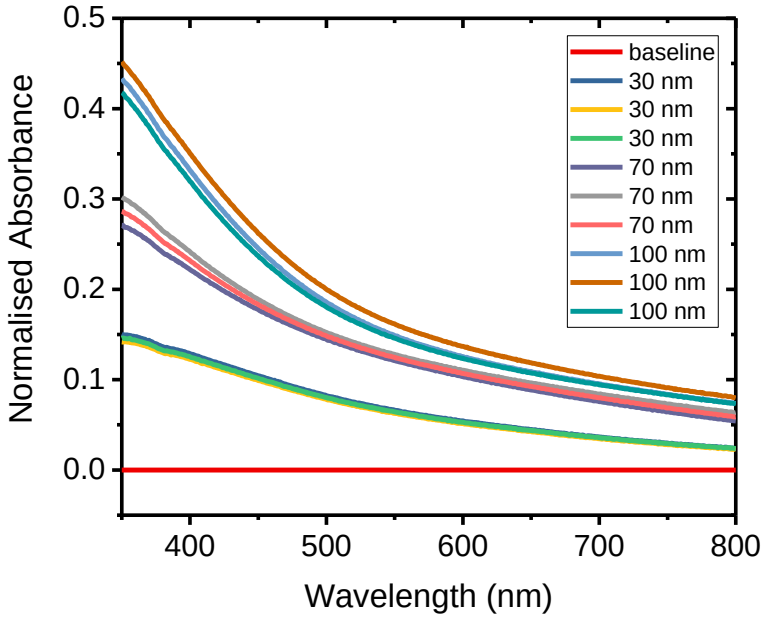

Figure S2.2. The complete data set of the UV-visible absorption spectra of synthetic eumelanin thin films, as a function of thickness. The red line represents the base line: a spectra taken from a clean glass slide. As it was mentioned in the main text, this data indicates that the eumelanin thin films show the same optical behaviour as eumelanin solutions.

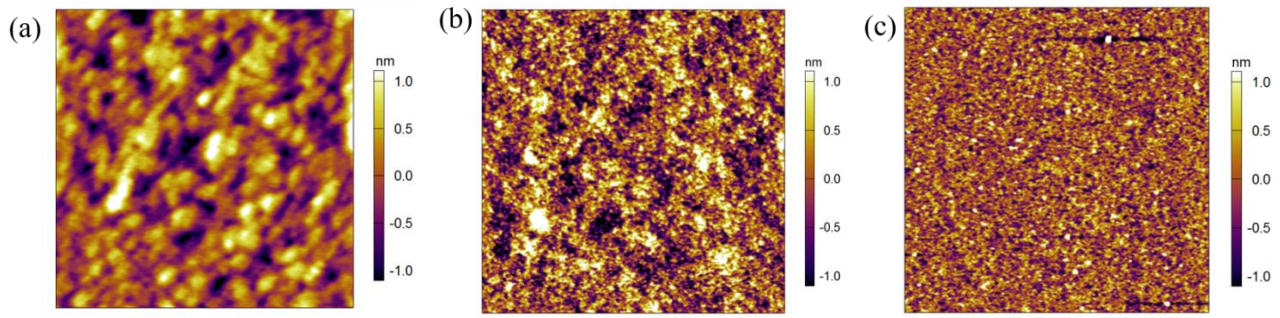

Figure S2.3. Topographical AFM images of eumelanin thin film on a Si substrate taken at different image dimensions/magnification: (a) 1x1 µm, (b) 5x5 µm, (c) 30x30 µm. At higher levels of magnification the film look smooth, however bulb-like structures can be observed on 1x1 µm image.

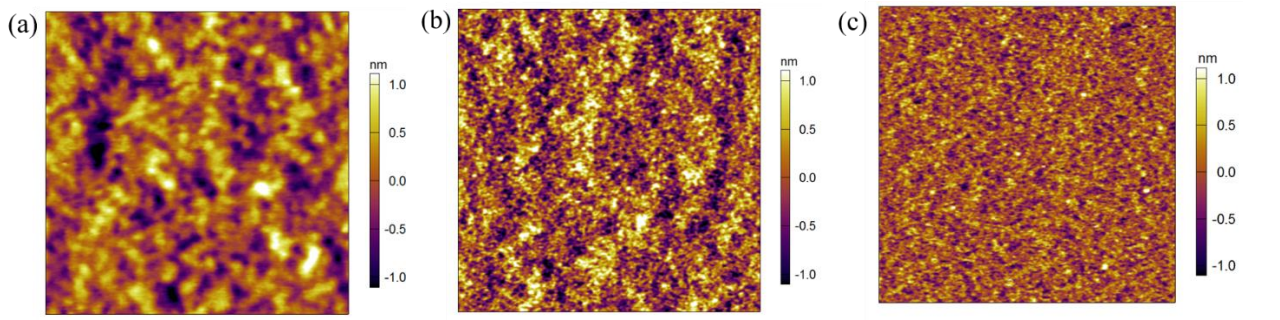

Figure S2.4. Topographical AFM images of eumelanin thin film on Mica substrate taken at different image dimensions/magnification: (a) 1x1 µm, (b) 5x5 µm, (c) 30x30 µm. The film looks smooth.

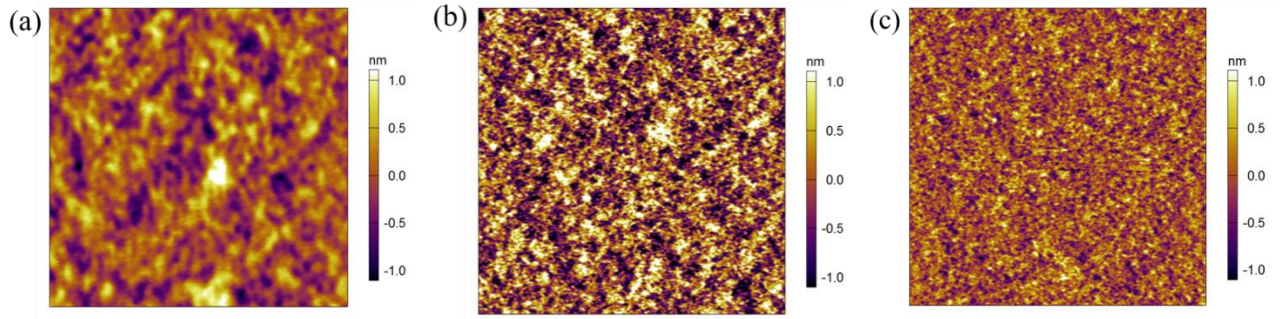

Figure S2.5. Topographical AFM images of eumelanin thin film on a silicon wafers with Si_3N_4 top layer taken at different image dimensions/magnification: (a) 1x1 µm, (b) 5x5 µm, (c) 30x30 µm. The film looks smooth.

Overall, AFM profiles of eumelanin thin films deposited onto a range of different substrates show a lot of similarity. Topographical maps and roughness calculations show that regardless of the substrate eumelanin can produce device quality films.

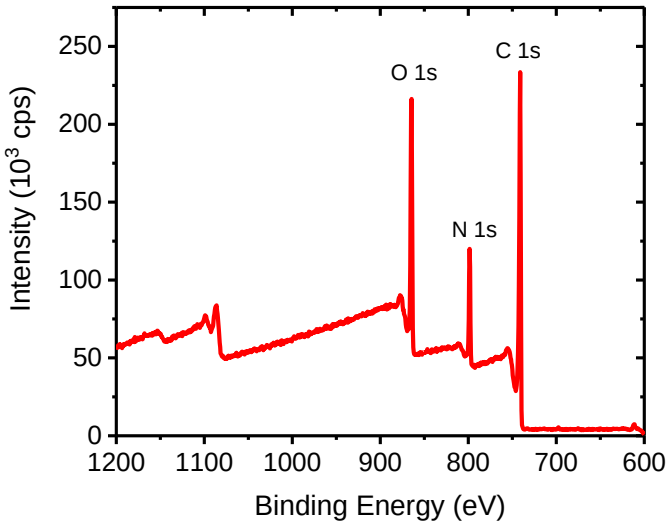

Figure S2.6. XPS scan obtained on eumelanin films on a glass substrate. The peaks represent the atoms presented in the material. Atomic ratios indicated.

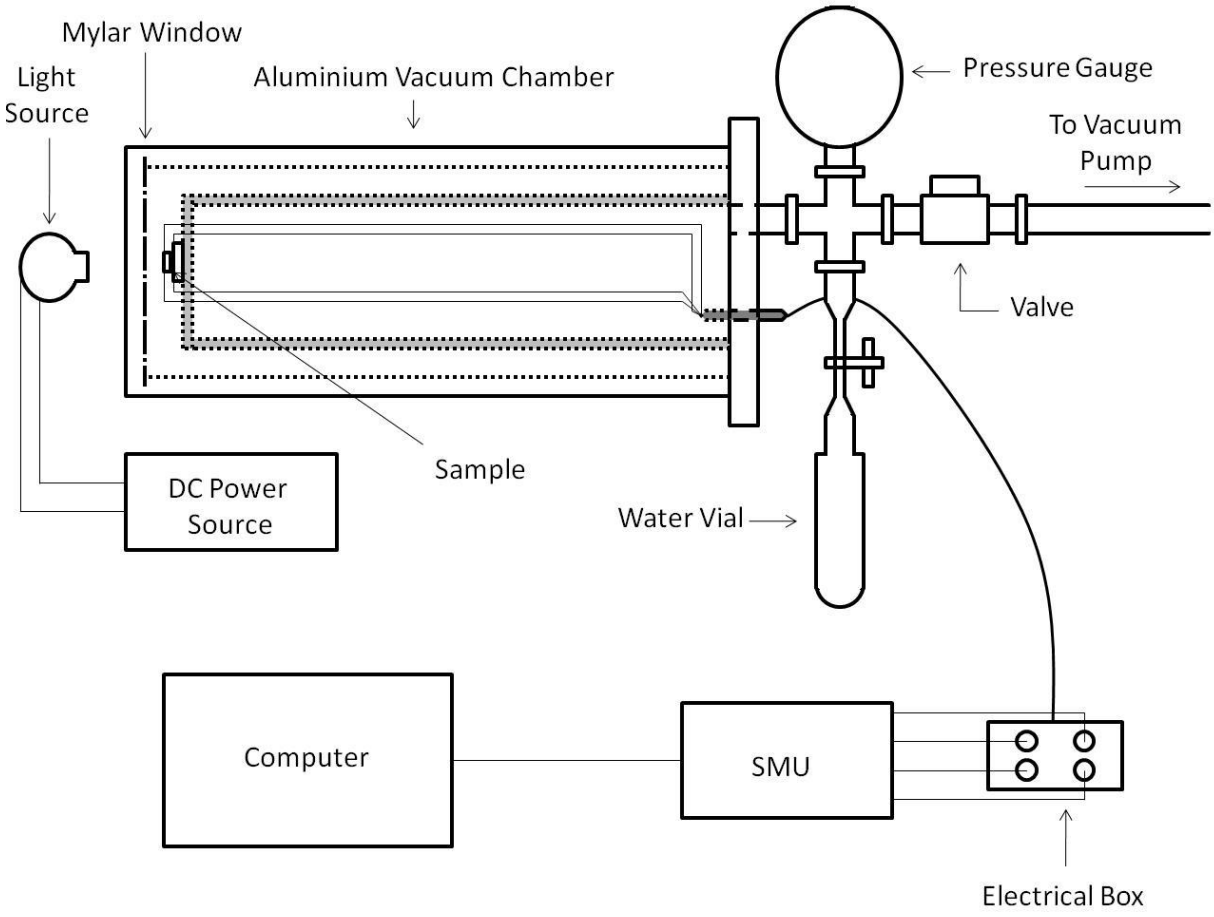

Figure S2.7. A vacuum-capable chamber used for the hydration dependent conductivity experiment.

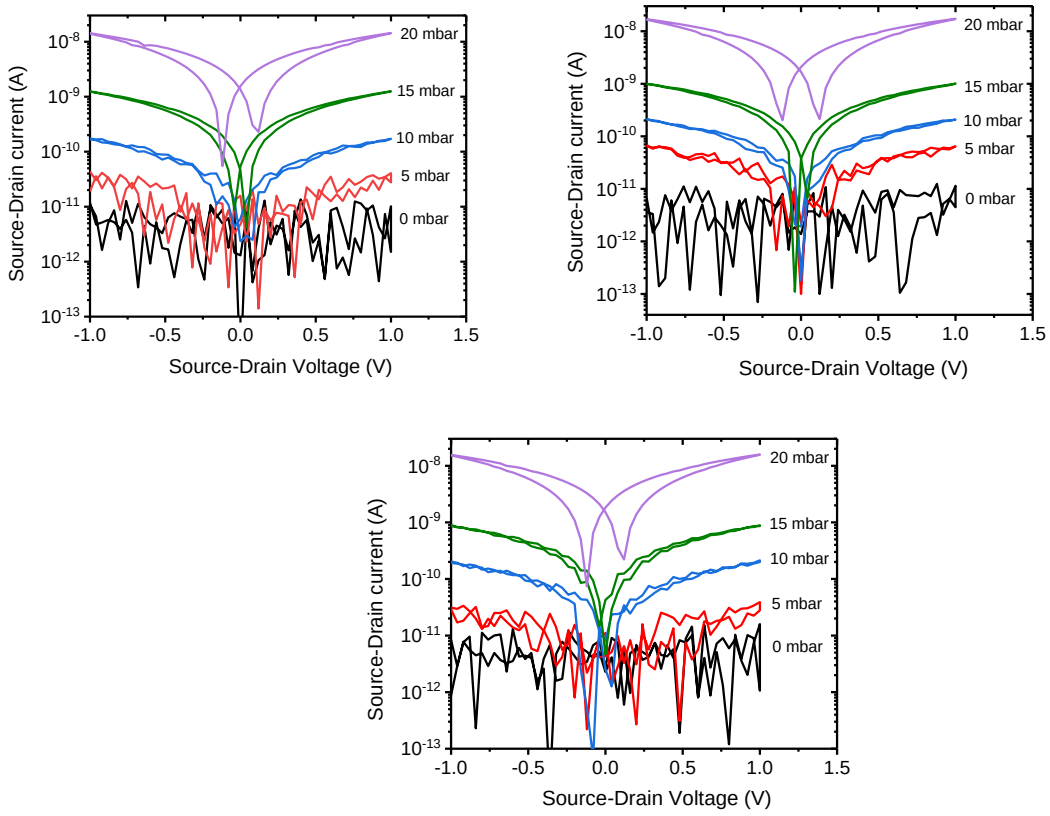

Figure S2.8. Complete data set of the channel current measured as a function of applied voltage for eumelanin thin films on three different samples at different water vapour pressures. The data was recalculated to the absolute values. Forward and reverse scans are shown. As indicated in the main text, the measurements were taken on three different substrates for each pressure point. The graph shows consistency of results from sample to sample and proves that the proposed procedure produces uniform and reproducible eumelanin thin films. Three orders of magnitude conductivity increase is observed when going from a fully dry to a fully wet film.

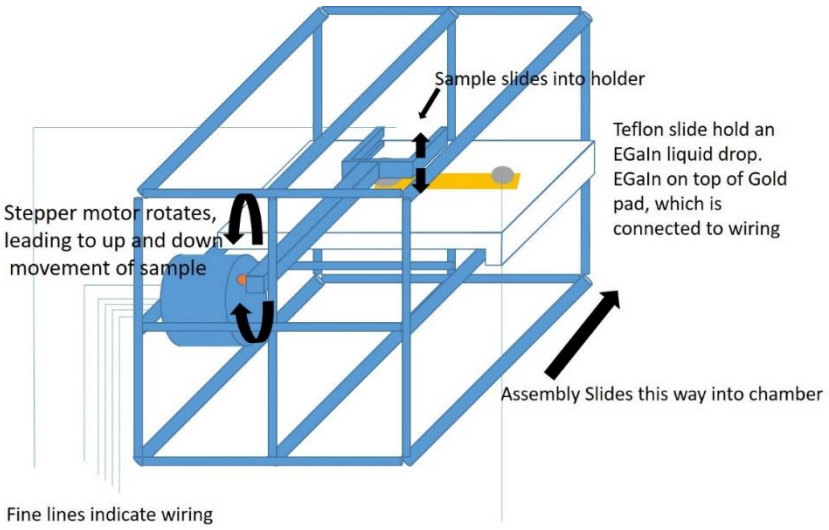

Figure S2.9. Schematic representation of the system used for the EGaIn gating to the sample.

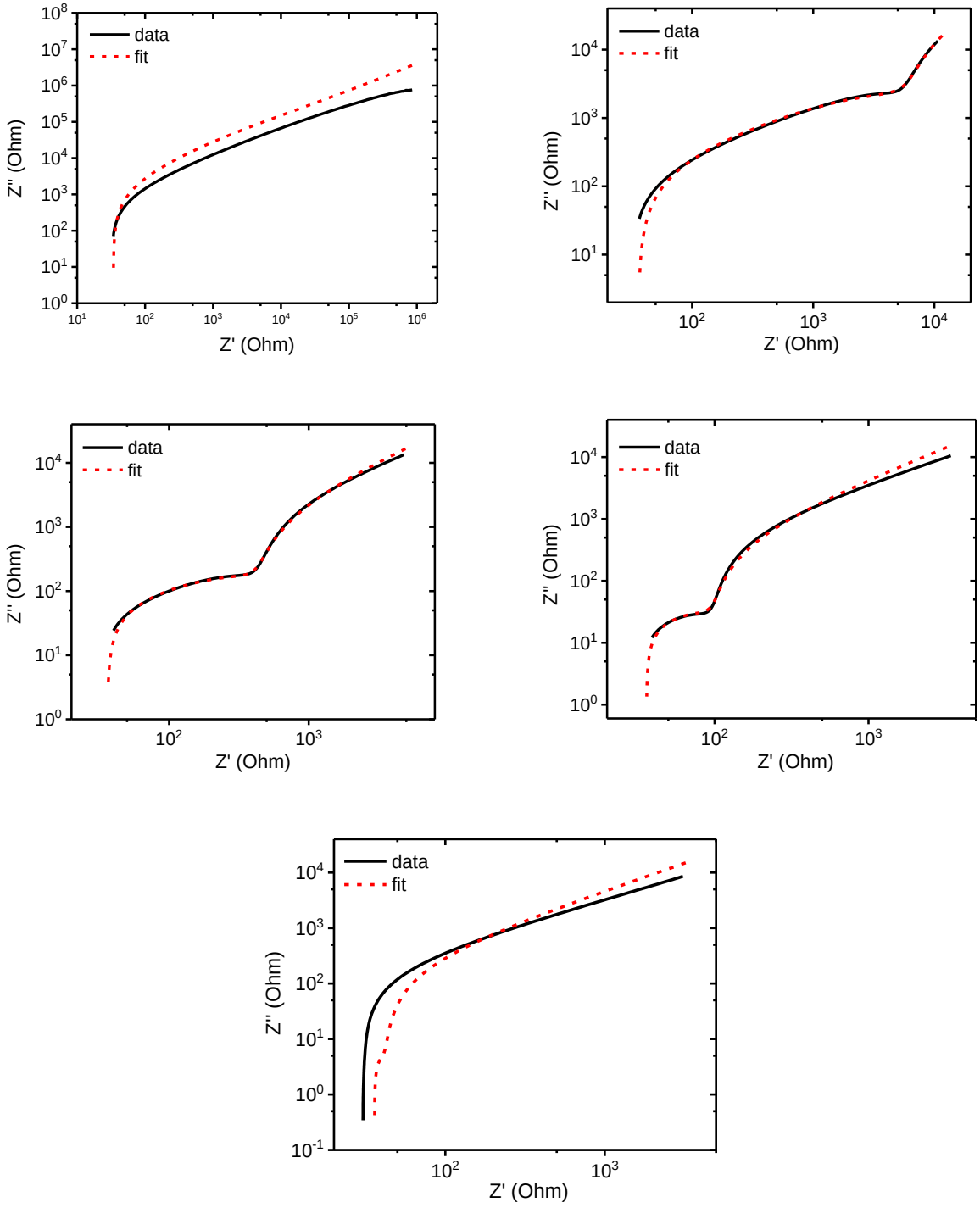

Figure S3.1. Nyquist plots obtained for a eumelanin thin film exposed to D_2O. The relative pressures are 0 (a), 0.25 (b), 0.5 (c), 0.74 (d) and 1.00 (e).

Chapter 4

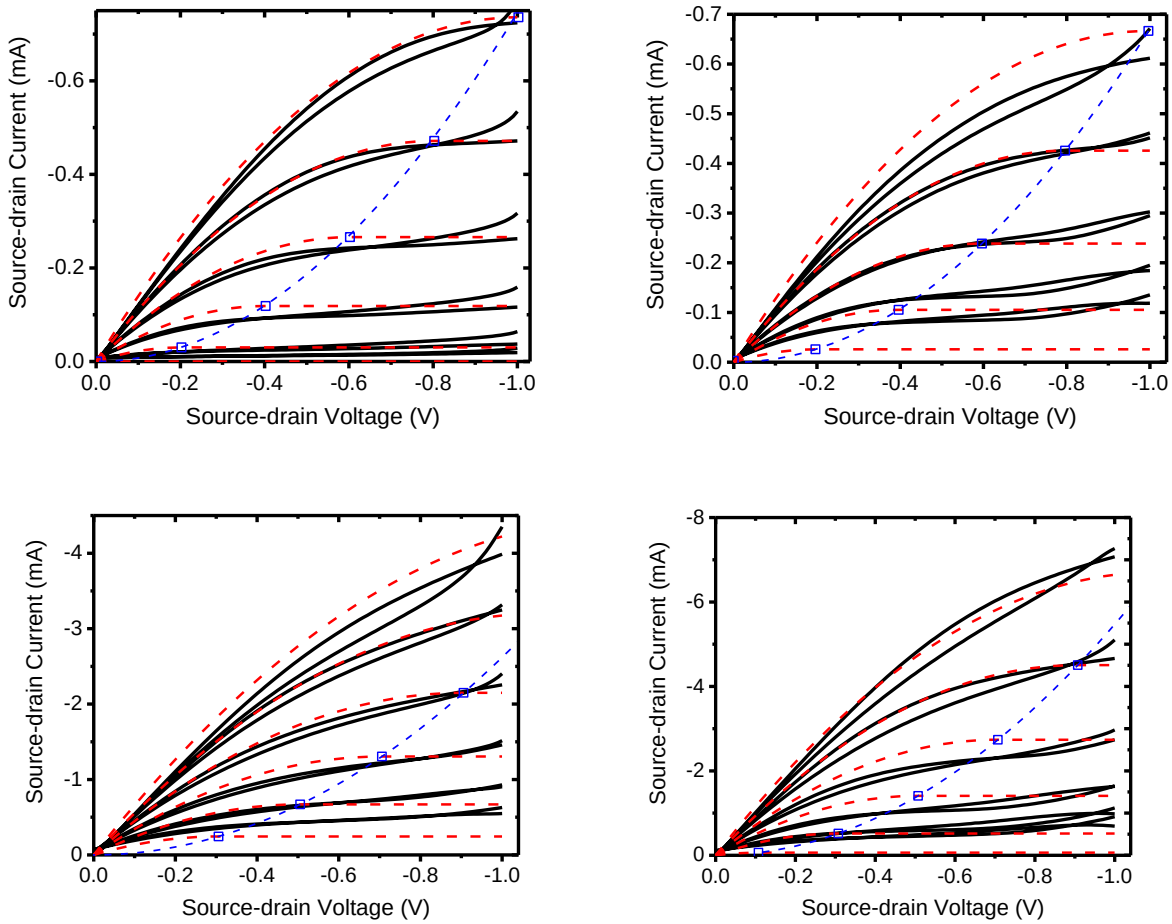

Figure S4.1. Output characteristics of OECTs with 50 nm (a), 100 nm (b), 200 nm (c) and 400 (nm) thick channels (black lines), V_g = -0.2 to 0.8 V (top to bottom), with the corresponding fits (red dashed lines). Blue empty squares are the saturation values.

Chapter 5

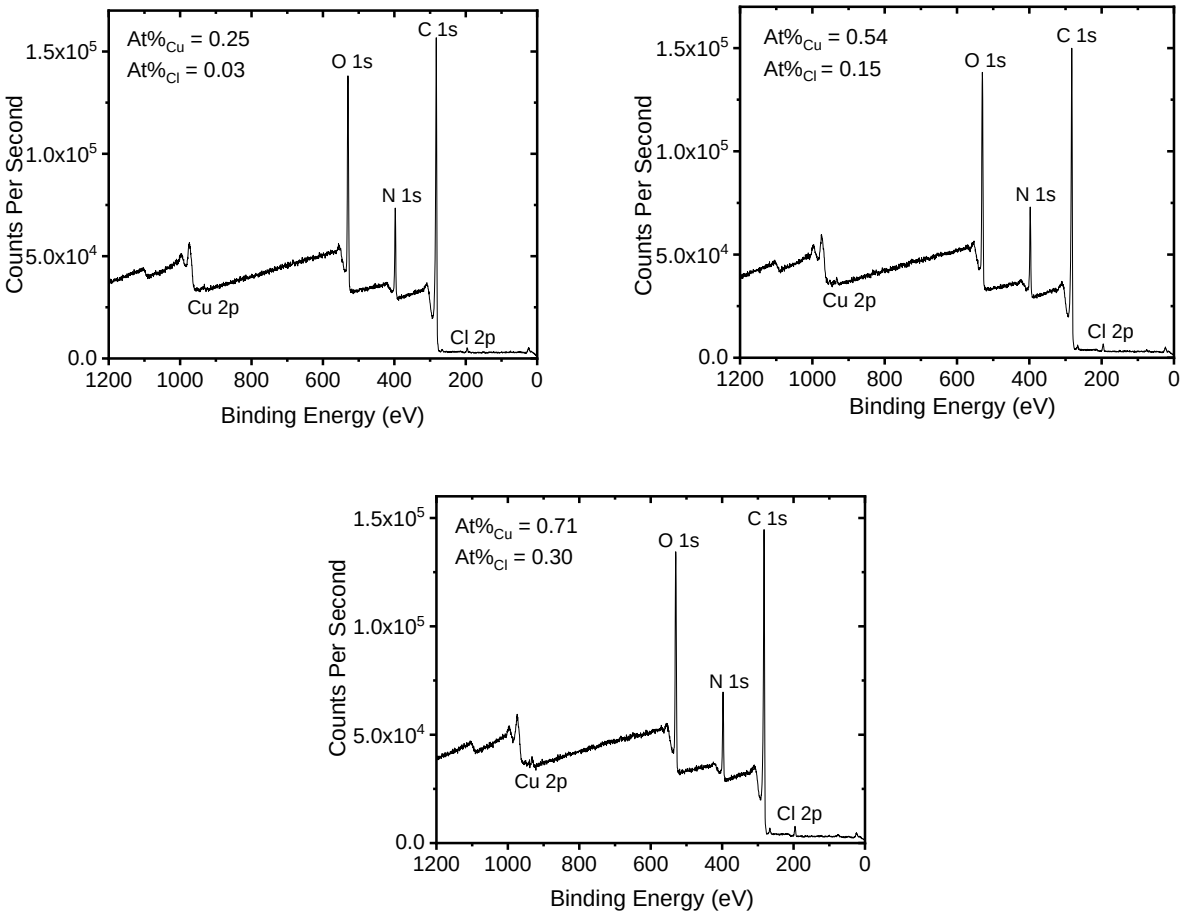

Figure S5.1. XPS scans obtained on Cu-eumelanin thin film on glass substrate fabricated from a solution spun cast for 1 min (a), 2 min (b), 3 min (c). Atomic ratios of Cu and Cl are indicated.

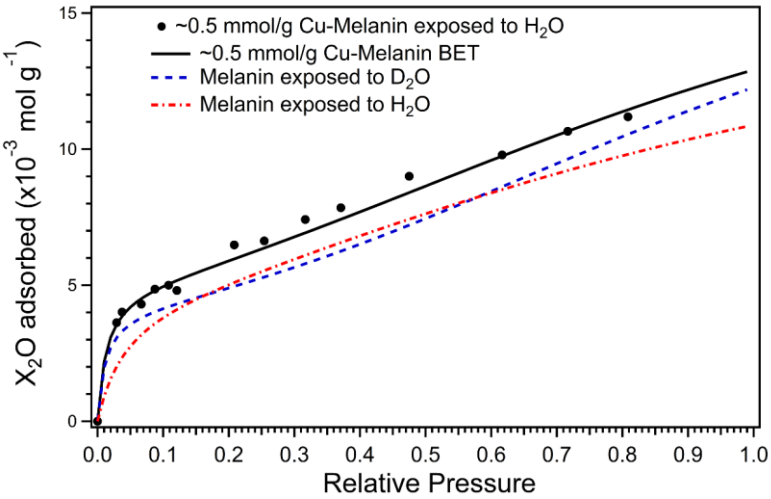

Figure S5.2: Adsorption isotherm of Cu-eumelanin (black) pressed pellets compared with standard synthetic eumelanin exposed to H_2O (red) and D_2O vapour (blue). It can be seen that Cu-eumelanin is more hydrophilic than standard synthetic eumelanin, especially at low vapour pressure. Figure reproduced from [1].

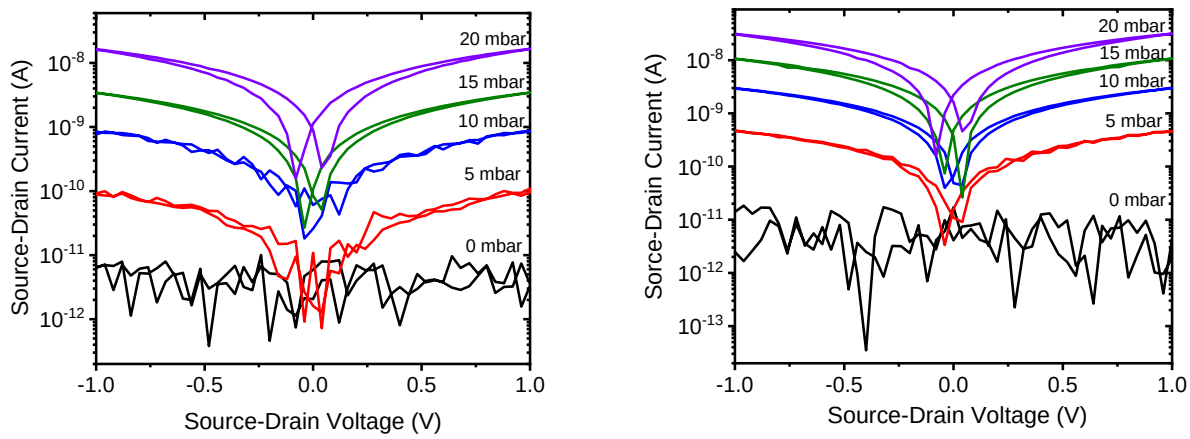

Figure S5.3. Source-drain current as a function of voltage for a Cu-eumelanin thin film: 1 min stirring time (left) and 5 min stirring time (right). Each IV measurement was taken at different water vapour pressures, which are indicated. Each curve is an average of three measurements.

Tables

Chapter 2

p (H_2O) (mbar)	Exposed / Evacuated	Thickness 2 (Å)	ρ 1 (10^{-6} Å^{-2})	ρ 2 (10^{-6} Å^{-2})	ρ 3 (10^{-6} Å^{-2})
0.0	Evacuated	342 ± 1	3.22 ± 0.07	3.35 ± 0.06	3.20 ± 0.10
2.3	Exposed	348 ± 1	3.17 ± 0.07	3.29 ± 0.06	3.21 ± 0.09
	Evacuated	341 ± 1	3.20 ± 0.07	3.37 ± 0.06	3.28 ± 0.10
6.2	Exposed	362 ± 1	3.07 ± 0.07	3.19 ± 0.06	3.08 ± 0.09
	Evacuated	343 ± 1	3.19 ± 0.07	3.36 ± 0.06	3.35 ± 0.09
15.5	Exposed	395 ± 2	2.89 ± 0.07	2.94 ± 0.06	2.80 ± 0.10
	Evacuated	350 ± 1	3.14 ± 0.07	3.30 ± 0.06	3.24 ± 0.09
24.8	Exposed	437 ± 2	2.66 ± 0.07	2.69 ± 0.06	2.49 ± 0.10
	Evacuated	352 ± 1	3.05 ± 0.07	3.27 ± 0.06	3.25 ± 0.09

Table S2.1. NR fitting parameters for the film exposed to H_2O. Layer 1 = air interface layer, Layer 2 = bulk layer and Layer 3 = substrate interface layer. Tx = thickness of layer x, ρx = scattering length density of layer x, R1 = interfacial roughness between layer 1 and air, R2 = interfacial roughness between layer 2 and layer 1, R3 = interfacial roughness between layer 2 and layer 3. RS = interfacial roughness between layer 3 and the silicon substrate. Fixed parameters: T1 = 65 Å, T3 = 28 Å, R1 = 10 Å, R2 = 15 Å, R3 = 15 Å, RS = 8.3.

p (D_2O/H_2O) (mbar)	Exposed / Evacuated	T 2 (Å)	ρ 1 (10^{-6} Å^{-2})	ρ 2 (10^{-6} Å^{-2})	ρ 3 (10^{-6} Å^{-2})
0.0	Evacuated	327 ± 1	3.24 ± 0.07	3.37 ± 0.06	3.23 ± 0.08
2.0 (D_2O)	Exposed	333 ± 1	3.75 ± 0.08	4.03 ± 0.06	3.75 ± 0.08
	Evacuated	327 ± 1	3.63 ± 0.08	3.81 ± 0.06	3.68 ± 0.09
5.4 (D_2O)	Exposed	344 ± 1	4.46 ± 0.09	4.78 ± 0.06	4.48 ± 0.10
	Evacuated	328 ± 1	4.22 ± 0.08	4.38 ± 0.06	4.25 ± 0.09
13.5 (D_2O)	Exposed	373 ± 1	5.18 ± 0.09	5.31 ± 0.06	4.95 ± 0.11
	Evacuated	335 ± 1	4.42 ± 0.09	4.74 ± 0.06	4.54 ± 0.10
21.6 (D_2O)	Exposed	411 ± 1	5.65 ± 0.11	5.66 ± 0.06	5.23 ± 0.14
	Evacuated	339 ± 1	4.41 ± 0.10	4.88 ± 0.06	4.73 ± 0.11
24.8 (H_2O)	Exposed	423 ± 1	3.03 ± 0.07	2.99 ± 0.06	2.85 ± 0.08
	Evacuated	344 ± 1	3.21 ± 0.08	3.52 ± 0.06	3.46 ± 0.09

Table S2.2. NR fitting parameters for the film exposed initially to D_2O and then to H_2O to regenerate/back exchange the H/D moieties. Layer 1 = air interface layer, Layer 2 = bulk layer and Layer 3 = substrate interface layer. Tx = thickness of layer x, ρx = scattering length density of layer x, R1 = interfacial roughness between layer 1 and air, R2 = interfacial roughness between layer 2 and layer 1, R3 = interfacial roughness between layer 2 and layer 3, RS = interfacial roughness between layer 3 and the silicon substrate. Fixed parameters: T1 = 52 Å, T3 = 40 Å, R1 = 12 Å, R2 = 15 Å, R3 = 15 Å, RS = 8.5 Å.

H_2O	Relative pressure	**0.042**	**0.21**	**0.42**	**0.63**	**0.83**
	R_1 (Ohm)	34	36	36	36	36
	Q_2 ($F \cdot s^{(\alpha-1)}$)	$2.94e^{-9}$	$28.59e^{-9}$	$36e^{-9}$	$41.89e^{-9}$	$42e^{-9}$
	a_2	0.985 7	0.884 2	0.891 6	0.928 5	0.994 1
	R_2 (Ohm)	859 300	2 835	240.1	40	8.35
	R_0 (Ohm)	3.8e6	9 242	513	80	$78.18e^{-12}$
	t_0 (s)	$2.22e^{-3}$	$4.388e^{-3}$	$0.138\ 3e^{-3}$	$23.79e^{-6}$	$0.209\ 9e^{-18}$
	a_0	0.584	0.764	0.828	0.860	0.858
D_2O	Relative pressure	**0.05**	**0.25**	**0.5**	**0.75**	**1**
	R_1 (Ohm)	34	36	36	36	36
	Q_2 ($F \cdot s^{(\alpha-1)}$)	$3.818e^{-9}$	$18.12e^{-9}$	$24.74e^{-9}$	$27.53e^{-9}$	$1.2e^{-6}$
	a_2	0.963 7	0.897 3	0.920 1	0.928 5	0.889 8
	R_2 (Ohm)	859 300	6 515	400.1	60.09	12.6
	R_0 (Ohm)	$9.647e^{6}$	25 316	943.5	108	67 583
	t_0 (s)	2.104	$9.359e^{-3}$	$0.285\ 3e^{-3}$	$25.59e^{-6}$	0.015 74
	a_0	0.904	0.713	0.799	0.847	0.540

Table S3.1. Fitting parameters used to fit the data accordingly to the equivalent circuit (Fig. 3.2) for both H_2O and D_2O data at all hydration levels. Software used: Z Fit (Bio-Logic Science Instruments), Demo Version.

Neutron Reflectometry Modelling

The parameters presented in Table S2.1 and Table S2.2. were obtained by the modelling of the NR profiles. The modelling was done using the Motofit reflectometry analysis program [2, 3]. All of the models described used an SLD of 2.07×10^{-6} Å^{-2} for the silicon substrate. A three-layer model was used to fit all of the NR data. The reason for the 3 layer model was that initially, modelling of the eumelanin films as a single layer on top of a thin SiO_2 layer (SLD = 3.47×10^{-6} Å^{-2}) led to unsatisfactory fits of poor visual quality with high χ^2 values. Additional layers were therefore added to the model to improve the fitting quality. Upon the addition of a second eumelanin layer, the modelling software reduced the SiO_2 thickness to zero, increased the interfacial roughness between Si and SiO_2 and placed a thin interfacial layer at either the air interface or the substrate interface with a slightly lower SLD than the bulk layer. It was often observed that the two-layer models would not converge to a unique solution as the χ^2 values for the two fits with the interfacial layer either at the air or substrate interface were very similar. To address this, the eumelanin layers were modelled as three-layer films consisting of a bulk layer (which comprises the majority of the film) with two thin interfacial layers at the substrate and air interfaces. Such a model permits a transition layer at each interface. Once again, the fitting software minimised the thickness of the SiO_2 layer and increased the roughness between the silicon substrate and the lowest eumelanin layer. Given that the modelled SLDs of the interfacial layers in contact with the substrate are similar to or greater than the SiO_2 SLD, it was concluded that the SiO_2 layer could not be adequately distinguished as a separate layer. Thus the SiO_2 layer was removed from the model with its effects being incorporated into the increased roughness of the silicon/eumelanin interface. When the eumelanin films were fitted using the three-layer model without a dedicated SiO_2 layer, it was found that several of the fitting parameters (the thickness and roughness of the interfacial layers and the substrate/eumelanin roughness) were practically invariant in each fit for a given film. As such, these parameters were fixed for the modelling. This was based on the parameters from the best fit to the initial eumelanin films under vacuum (the 0.0 mbar plots in Figure 2.7 (A–D)). With the above, only four free structural modelling parameters were left – the thickness of the bulk eumelanin layer, and the SLDs of the three eumelanin layers in the model. For modelling consistency, all NR profiles were modelled using the three-layer model with only four unconstrained parameters as described. This approach consistently gave the lowest χ^2 values (significantly lower than for the two layer model). Also, the fits were excellent for all changes occurring for a given film during exposure to H_2O or D_2O and subsequent evacuation (representing a minimum of five SLD contrasts between the eumelanin film, air and the silicon substrate). In each case, the SLD of the interfacial layers rose and fell with the same trend as the bulk layer suggesting that water penetrating or leaving the bulk was also doing so in the interfacial layers.

The XRR reflectometry profile modelling was also performed using the Motofit reflectometry analysis program [2] (see Figure 2.6). The model used an SLD of 20.1 × 10^{-6} Å^{-2} (SLD = 4.7 × 10^{-7} Å^{-2}) for the silicon substrate with an interfacial roughness of 6.3 Å between the silicon substrate and the overlying organic layer, which had a thickness of 443 Å, an SLD of 13.4 × 10^{-6} Å^{-2} and a roughness of 11.1 Å at the organic/air interface, which is confirmation of the AFM results described in the main text.

The neutron reflectivity profiles were modelled with three layers as described in the. Both of the thin interfacial layers had SLDs that were slightly lower than or equal to the bulk layer depending on the exposure state. To simplify the analyses that follow, the thickness-weighted average of the individual layer SLDs (Tables S2.1 and S2.2) were determined. The average neutron SLDs for the three eumelanin films under vacuum prior to exposure were similar being 3.29, 3.34 and 3.32 × 10^{-6} Å^{-2} (Figure 2.5). The range of the observed SLD values (0.05 × 10^{-6} Å^{-2}) was used as the uncertainty to account for random sample-to-sample variations. This uncertainty was added to the fitting software. For the XRR contribution to the determination of the prefactor in equation (2.1), an X-ray reflectivity profile recorded for a fourth evacuated eumelanin film (Figure 2.6) was modelled as a single layer with a thickness of 443 Å and an X-ray SLD of 13.4 × 10^{-6} Å^{-2}. Finally, high-resolution XPS measurements under vacuum revealed atomic percentages for C, N and O of 72.3%, 9.2% and 18.5%, respectively. When combined with the neutron and X-ray SLDs these atomic ratios were consistent with the empirical formula of M_i = $C_{7.83}H_{5.39}NO_{2.01}$, which is commensurate with that of crosslinked DHI ($C_8H_7NO_2$) and the quinone form of DHI ($C_8H_5NO_2$). The associated mass density for the film was determined to be 1.52 g cm^{-3} under vacuum.

Appendix References

1. Rienecker, S., Opto-Electronic Properties of Melanin: Solid-State Characterisation via EPR, Conductivity, and Copper Chelation, in School of Chemistry and Molecular Biosciences. 2017, The University of Queensland.

2. Nelson, A., Co-refinement of multiple-contrast neutron/X-ray reflectivity data using MOTOFIT. Journal of Applied Crystallography, 2006. 39: p. 273–279.

3. Nelson, A., Motofit – integrating neutron reflectometry acquisition, reduction and analysis into one, easy to use, package. Journal of Physics: Conference Series, 2010. 251.